

We are IntechOpen, the world's leading publisher of Open Access books Built by scientists, for scientists

6,300

Open access books available

171,000

International authors and editors

190M

Downloads

Our authors are among the

154

Countries delivered to

TOP 1%

most cited scientists

12.2%

Contributors from top 500 universities



WEB OF SCIENCE™

Selection of our books indexed in the Book Citation Index
in Web of Science™ Core Collection (BKCI)

Interested in publishing with us?
Contact book.department@intechopen.com

Numbers displayed above are based on latest data collected.
For more information visit www.intechopen.com



Multi-Core Optical Fibers: Theory, Applications and Opportunities

Andrés Macho Ortiz and Roberto Llorente Sáez

Additional information is available at the end of the chapter

<http://dx.doi.org/10.5772/intechopen.72458>

Abstract

Multi-core fibers (MCFs) have sparked a new paradigm in optical communications, as they can significantly increase the Shannon capacity of optical networks based on single-core fibers. In addition, MCFs constitute a useful platform for testing different physical phenomena, such as quantum or relativistic effects, as well as to develop interesting applications in various fields, such as biological and medical imaging. Motivated by the potential applications of these new fibers, we will perform a detailed review of the MCF technology including a theoretical analysis of the main physical impairments and new dispersive effects of these fibers, and we will discuss their emerging applications and opportunities in different branches of science.

Keywords: multi-core fiber, inter-core crosstalk, birefringent effects, intermodal dispersion, microwave photonics, optical sensors, medical imaging

1. Introduction

Data traffic demand in access and backbone networks has been increased exponentially in the last three decades [1, 2]. Remarkably, in the last decade, the development of streaming transmissions and cloud computing has accelerated this growth [3]. Nowadays, in spite of the fact that this data traffic demand is easily covered by wavelength-division multiplexed (WDM) systems based on single-mode single-core fibers (SM-SCFs),¹ recent works show that the WDM systems are rapidly approaching their Shannon capacity limit [4].

Aimed to overcome the Shannon capacity limit of WDM networks using SM-SCFs, space-division multiplexing (SDM) has been extensively investigated in recent years [5–7].

¹SM-SCFs are also termed in the literature as single-mode fibers (SMFs).

Remarkably, the SDM concept within the context of optical communications was proposed for the first time in the decade of 1980 [8–10]. Unfortunately, the technology underneath SDM was immature and extremely expensive. Nevertheless, the fabrication methods of the SDM fibers and optical devices have been extensively developed in the last decade reducing their manufacturing cost [11]. In this scenario, new types of optical fibers based on the SDM concept have been proposed [5–12]: fiber bundle based on SM-SCFs, multi-mode single-core fibers (MM-SCFs),² single/multi-mode multi-core fibers (SM/MM-MCFs) and photonic crystal fibers.

In contrast with the other aforementioned SDM fibers, MCFs allow us to increase the channel capacity limit of SM-SCFs by exploiting the six signal dimensions (time, wavelength, amplitude, phase, polarization and space) through spatial multi-dimensional modulation formats and digital signal processing at the receiver [13–15]. Interestingly, SCFs have also been used as an experimental platform for testing different phenomena related to diverse branches of physics, such as fluid dynamics, quantum mechanics, general relativity and condensed matter physics, as well as to develop applications in other fields [16–23]. Along this line, MCFs are potential laboratories that could extend the possibilities offered by SCFs. As an example, disordered MCFs exhibiting transverse Anderson localization have been proposed with potential applications in biological and medical imaging [22].

Inspired by the potential applications of these new fibers, we perform a detailed review of the MCF technology including a theoretical analysis of the main physical impairments and new dispersive effects of these fibers, and we discuss their applications and opportunities in different branches of physics, engineering and medicine. The chapter is organized as follows. In Section II, the different MCF types are revisited. In Section III, we include some fundamental aspects of light propagation in the linear and nonlinear fiber regime. Specifically, we focus on the theoretical description of the physical impairments observed in these fibers in the single-mode regime: the linear and nonlinear inter-core crosstalk, the intra- and inter-core birefringent effects, the intermodal dispersion and higher-order coupling and nonlinear effects. In Section IV we discuss the main applications and opportunities of MCFs in photonics, medicine and experimental physics. Finally, in Section V the main conclusions of the chapter and the open research lines in the topic are highlighted.

2. Multi-core fiber types and fabrication

MCF designs can be classified in different categories attending to diverse fiber parameters and characteristics. **Table 1** shows the usual MCF designs employed for SDM transmissions and MCF laser and sensing applications:

1. The refractive index profile of each core allows us to differentiate between step-index (SI-MCF) and gradual-index MCFs (GI-MCF). In the former case, the refractive index profile of all cores has a step between two constant values in the core and cladding interface. However, in the latter case, a MCF is referred to as GI-MCF if at least one core

²MM-SCFs are also referred to as multi-mode fibers (MMFs).

has a continuous refractive index profile. Along this line, we can make a distinction with a third type of MCF: a trench- or hole-assisted MCF (TA-MCF or HA-MCF). In general, a TA- and HA-MCF present a multi-step refractive index profile in the cladding to reduce the mode-coupling (inter-core crosstalk) between the linearly polarized (LP) modes of adjacent cores [7, 11, 12, 24]. Specifically, in a HA-MCF an additional step is included in the cladding by performing holes around the cores [7].

MCF classification	Type 1	Type 2	Figure/comments
Refractive index profile	Step-index SI-MCF	Gradual-index GI-MCF	
Modal regime	Single-mode SM-MCF	Multi-mode MM-MCF	
Spatial homogeneity	Homogeneous cores HO-MCF	Heterogeneous cores HE-MCF	
Core-to-core distance (d_{ab})	Uncoupled cores ($d_{ab} \geq 7 \cdot R_0$) UC-MCF	Coupled cores ($d_{ab} < 7 \cdot R_0$) CC-MCF	
Intrinsic linear birefringence	Lowly birefringent cores LB-MCF	Highly birefringent cores HB-MCF	
Others	(1) Trench-assisted MCF (TA-MCF), (2) Hole-assisted MCF (HA-MCF), (3) MCF with coupled and uncoupled cores, (4) Dispersion-shifted MCF (DS-MCF), (5) MCF Bragg gratings, (6) Hexagonal shaped		

Table 1. Classification of multi-core fiber types.

2. A single-mode MCF (SM-MCF) supports only the LP₀₁ mode in each core. In contrast, if a given core guides several LP modes, the fiber is known as a multi-mode MCF (MM-MCF). Moreover, a MCF supporting only the first three or four LP mode groups (LP₀₁, LP₁₁, LP₂₁, LP₀₂) is usually termed as a few-mode MCF (FM-MCF) [7].
3. Attending to the spatial homogeneity of the MCF structure, we can make a distinction between a homogeneous MCF (HO-MCF) or a heterogeneous MCF (HE-MCF). In the former case, all cores present the same refractive index profile, and in the latter case, the MCF comprises at least one core with a different refractive index profile³.
4. The core-to-core distance (or core pitch) is the main fiber parameter which determinates the inter-core crosstalk level among the LP modes of each core. Usually, if the core pitch between two homogeneous cores *a* and *b* (d_{ab}) is lower than seven times⁴ the core radius R_0 , the LP modes of the cores are found to be degenerated and the MCF supports supermodes [25]. In such a case, the MCF is referred to as a coupled-core MCF (CC-MCF). On the contrary, if the LP modes of the cores *a* and *b* are non-degenerated, the supermodes cannot be generated and each core is considered as an individual light path. This fiber design is termed as uncoupled-core MCF (UC-MCF). Recent works have reported a mixed design using coupled and uncoupled cores [26, 27].
5. If the intrinsic linear birefringence of each core $\Delta n = |n_x - n_y|$ is lower than 10^{-7} , the MCF is referred to as lowly birefringent MCF (LB-MCF). Nonetheless, if a given core has a $\Delta n > 10^{-7}$ the MCF is known as a highly birefringent MCF (HB-MCF). In general, a HB-MCF comprises elliptical or panda cores for polarization-maintaining applications [28, 29].
6. Other designs of MCFs involve: dispersion-shifted cores (DS-MCFs) [30], selective-inscribed Bragg gratings [31] and hexagonal shaped cores [32].

Once the MCF cross-section design is established, the specific MCF fabrication method is of key importance for the final optical transmission characteristics. MCF fabrication processes have been refined and optimized in the last years with an intensive research work [5, 7, 33–37]. In this scenario, the main technological challenge in the design and fabrication of uncoupled MCFs is to minimize the crosstalk providing the maximum core isolation. Usually, the design work is performed numerically using commercial simulation packages. The simulation analysis targets to determine the cross-section modal distribution, the spectral power density of the LP modes, the associated power losses and the resulting inter-core crosstalk.

MCF fabrication can be addressed by microstructured stack-and-draw technology [36], a flexible technology which allows us to fabricate very different fibers on the same machinery. Unfortunately, MCF manufacturing is a complex process with nonlinear results on the process parameters. In particular, some rods or capillaries configurations may be technically difficult to draw into the designed form, which results in a MCF with higher crosstalk levels than in the

³Two cores *a* and *b* have a different refractive index profile if $n_a(r_a) \neq n_b(r_b)$, where $r_{a(b)}$ is the local radial coordinate of each core. Hence, two step-index cores have a different refractive index profile if $n_a(r_a = 0) \neq n_b(r_b = 0)$.

⁴The condition $d_{ab} < 7R_0$ is only an approximation in the third transmission window and in single-mode regime of each core, with $R_0 \sim 4 \mu\text{m}$. In general, the criteria to achieve the supermode regime in the MCF structure depend on additional fiber parameters such as the refractive index profile and the wavelength of the optical carrier.

original design. In this scenario, it is necessary to investigate the linear and nonlinear MCF propagation taking into account not only the MCF manufacturing imperfections, but also additional external fiber perturbations (see below). This would be of great benefit for investigating multi-dimensional modulation formats, spatial encoding techniques and sharing of receiver resources in MCF systems [38–41].

3. Linear and nonlinear propagation in real MCFs

In general, the electromagnetic analysis of a MCF should be performed by solving the macroscopic Maxwell equations (MMEs) in each dielectric region of the fiber (cores + cladding) and applying the boundary conditions between the cores-cladding interfaces. However, the calculation of the exact MCF eigenmodes from the MMEs presents a high degree of complexity, and usually, they should be calculated numerically. Therefore, in order to analyze theoretically the electromagnetic phenomena in MCF media, the perturbation theory is usually employed. **Figure 1** shows a flowchart of this approach.

The goal is to derive a set of coupled equations from the MMEs in terms of the complex envelopes of the electric field strength in each core performing the next steps:

1. First, we should propose the ansatz of the global electric field strength (\mathcal{E}) of the MCF structure following the assumption of the classical perturbation theory [42]: the exact electric field strength is approximated by a linear combination of the mi polarized core modes⁵ considering isolated cores, that is, assuming that the geometry of each core m is not perturbed by the presence of adjacent cores [$\mathcal{E} \approx \sum \mathcal{E}_{mi}$]. At the same time, we should decouple the rapid- and the slowly varying temporal and longitudinal changes of \mathcal{E}_{mi} . The

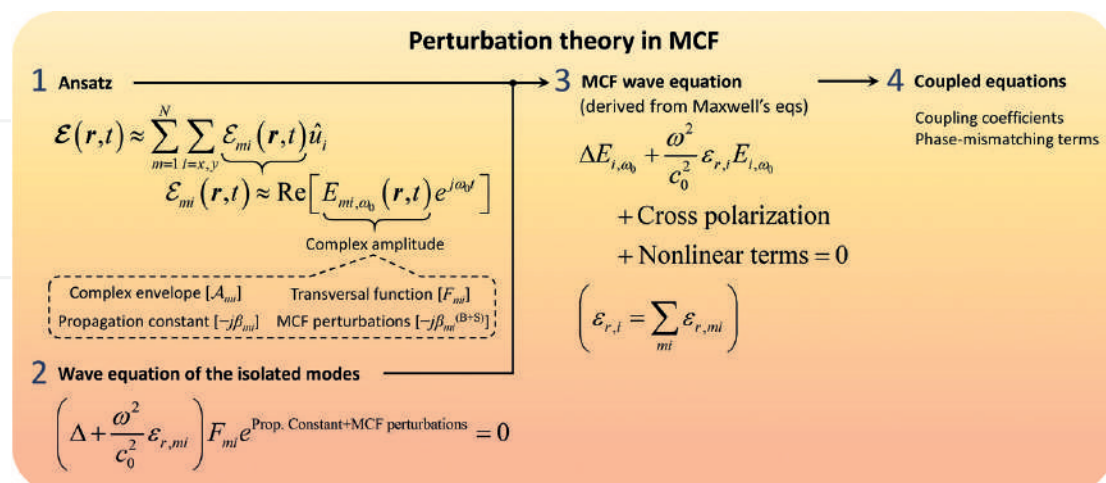


Figure 1. Flowchart of the perturbation theory in MCF media to derive the coupled equations from the macroscopic Maxwell equations.

⁵The polarized core mode mi refers to the $LP_{01,mi}$ mode associated with core m and polarization axis i .

rapidly varying temporal changes are decoupled by using the slowly varying complex amplitude approximation with $\mathcal{E}_{mi}(\mathbf{r}, t) \approx f(E_{mi, \omega_0}(\mathbf{r}, t))$, where E_{mi, ω_0} is the complex amplitude and ω_0 is the angular frequency of the optical carrier⁶. In a similar way, the rapidly varying longitudinal variations are decoupled by writing E_{mi, ω_0} as a function of the complex envelopes $\mathcal{A}_{mi}(z, t)$, that is, $E_{mi, \omega_0}(\mathbf{r}, t) \approx f(\mathcal{A}_{mi}(z, t))$. Although \mathcal{E}_{mi} is written assuming isolated conditions, the complex envelopes should be assumed longitudinal dependent to describe not only the usual longitudinal distortion⁷ of the optical pulses in SM-MCFs, but also the longitudinal fluctuations induced by the mode-coupling. Moreover, E_{mi, ω_0} also involves fundamental information such as the ideal propagation constant ($-j\beta_{mi}$), the transversal eigenfunction (F_{mi}) and the MCF perturbations [bending, twisting and additional fiber birefringent fluctuations modeled by the longitudinal and temporal dependent phase function $\beta_{mi}^{B+S}(z, t)$]⁸.

2. Each polarized core mode \mathcal{E}_{mi} is written by assuming isolated conditions of each core. Therefore, the transversal eigenfunction F_{mi} and the ideal phase constant β_{mi} can be expressed as indicated in [44] for the LP₀₁ mode of a single-core fiber. Moreover, taking into account that the nonlinear effects are not included in the modal solution of [44] and in the MCF perturbations β_{mi}^{B+S} , thus the eigenfunction $F_{mi} \cdot \exp(-j(\beta_{mi} + \beta_{mi}^{B+S})z)$ should satisfy the linear wave equation in each core and polarization in $\delta z \sim \lambda_0$, where λ_0 is the maximum value of the wavelength of the optical carrier in the multi-dielectric medium⁹.
3. In the third step, the wave equation of the MCF should be derived for the complex amplitudes E_{mi, ω_0} from the MMEs by taking into account the cross- and nonlinear polarization.
4. Finally, using the results of the first and second step in the MCF wave equation, we finally derive the coupled equations of the complex envelopes by assuming the slowly varying complex envelope approximation (SVEA), that is, $\delta_z \mathcal{A}_{mi} \ll |\mathcal{A}_{mi}|$ in $\delta z \sim \lambda_0$ and $\delta_t \mathcal{A}_{mi} \ll |\mathcal{A}_{mi}|$ in $\delta t \sim 2\pi/\omega_0$. More specifically¹⁰:

$$\left| \frac{\partial^2 \mathcal{A}_{mi}}{\partial z^2} \right| \ll k_0 \left| \frac{\partial \mathcal{A}_{mi}}{\partial z} \right| \ll k_0^2 |\mathcal{A}_{mi}|; \quad \left| \frac{\partial^2 \mathcal{A}_{mi}}{\partial t^2} \right| \ll \omega_0 \left| \frac{\partial \mathcal{A}_{mi}}{\partial t} \right| \ll \omega_0^2 |\mathcal{A}_{mi}|, \quad (1)$$

where $k_0 = 2\pi/\lambda_0$. Thus, we can approximate $\partial_z^2 \mathcal{A}_{mi} \approx 0$.

In the following subsections, we will review the new physical impairments observed in SM-MCFs using the aforementioned perturbation theory. First, we will describe the inter-core

⁶In general, we cannot consider a single-optical carrier in SDM-WDM systems using SM-MCFs. However, the interchannel nonlinearities should only be taken into account for optical pulses higher than 50 ps [43]. Therefore, the assumption of a single-optical carrier allows us to investigate the major physical impairments in SM-MCFs.

⁷Chromatic dispersion, polarization-mode dispersion and additional distortions induced by the intra-core nonlinear effects.

⁸In Section 3.1, we will be more specific with the description of the MCF perturbations.

⁹The symbol λ_0 is commonly used in the literature to describe the wavelength of the optical carrier at the vacuum. The context should avoid any confusion.

¹⁰Note that $\delta_z \mathcal{A}_{mi}$ and $\delta_t \mathcal{A}_{mi}$ are defined as $\delta_z \mathcal{A}_{mi} := |\mathcal{A}_{mi}(z, t) - \mathcal{A}_{mi}(z + \delta z, t)|$ and $\delta_t \mathcal{A}_{mi} := |\mathcal{A}_{mi}(z, t) - \mathcal{A}_{mi}(z, t + \delta t)|$.

crosstalk among cores when assuming a single polarization. Second, we will discuss the intra- and inter-core birefringent effects by including two polarizations per core. Later, we will analyze the intermodal dispersion and its impact on Gaussian pulses and optical solitons. And finally, higher-order coupling and nonlinear effects will be investigated when propagating optical pulses in the femtosecond regime.

3.1. Inter-core crosstalk

In multi-dielectric media, we can observe mode-coupling among adjacent dielectric regions. The continuity of the electromagnetic field in such media is the physical origin of the mode-coupling, referred to as the inter-core crosstalk (IC-XT) in MCFs.

The IC-XT behavior is induced by the longitudinal and temporal deterministic and random MCF perturbations. The longitudinal perturbations include the macrobending, microbending, fiber twisting and the intrinsic manufacturing imperfections of the fiber. The temporal perturbations are induced by external environmental factors, such as temperature variations and floor vibrations modifying the propagation constant of each polarized core mode, the bending radius and the twist rate of the optical medium. In spite of the fact that the deterministic nature of the intrinsic manufacturing imperfections, the remaining perturbations present a random nature, and therefore, the IC-XT will have a stochastic evolution in the time and space domain [33, 45–50].

Figure 2 shows the temporal evolution of the IC-XT measured during 26 hours in a homogeneous 4-core MCF [Fibercore SM-4C1500(8.0/125)] between two adjacent cores in the linear and nonlinear regimes (power launch levels of 0 and 17 dBm, respectively). Although the bending radius and the twist rate present a constant value in the experimental set-up (see [49] for more details), the slight longitudinal and temporal local variations of both fiber parameters induce a longitudinal and temporal random evolution of the IC-XT in both power regimes. In addition, in the nonlinear regime, the Kerr effect is stimulated in the illuminated core 3 reducing the index-matching between the measured cores 1 and 3. In this scenario, the homogeneous cores 1 and 3 become heterogeneous when high power launch levels are injected in a

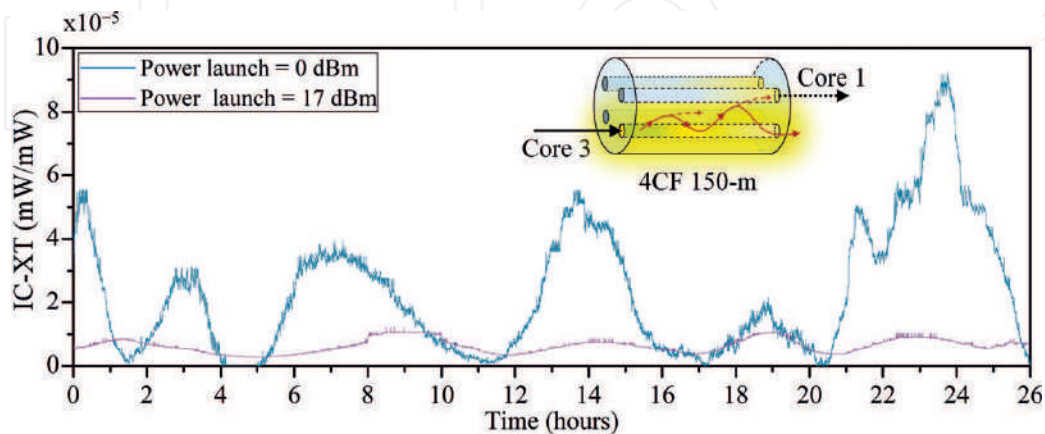


Figure 2. Measured temporal profile of the linear and nonlinear IC-XT between adjacent cores in a homogeneous 4-core MCF (results based on [49]).

given core. As a result, the MCF can be modeled in the nonlinear regime as an asymmetric optical coupler with random behavior, and consequently, the IC-XT mean and variance is reduced.

From these results, we conclude that the IC-XT has a random nature in both linear and nonlinear power regimes. Hence, at this point it is natural to ask how the probability distribution is. In a first investigation of this impairment, the answer can be easily found from the perturbation theory by assuming several initial simplifications: two cores a and b , a single polarization x and monochromatic electric fields. The last two approximations allow us to reduce the mathematical discussion of the IC-XT. In the next sections, these approximations will be revisited. Therefore, following a similar and simple approach as in the first works of the IC-XT [33, 45–50], the global electric field strength of the weakly guiding MCF (only two cores a and b and a single polarization x) is expressed as:

$$\begin{aligned} \mathcal{E}(\mathbf{r}, t) &\approx \sum_{m=a,b} \mathcal{E}_m(\mathbf{r}, t) \hat{x} \approx \sum_{m=a,b} \operatorname{Re}[E_{m,\omega_0}(\mathbf{r}) \exp(j\omega_0 t)] \hat{x} \\ &= \sum_{m=a,b} \operatorname{Re}[A_m(z) F_m(x, y, \omega_0) \exp(-j\beta_m(\omega_0)z) \exp(j\omega_0 t)] \hat{x}, \end{aligned} \quad (2)$$

where A_m is the complex envelope¹¹ of the continuous wave in the core $m = a, b$ satisfying the SVEA; F_m is the transversal eigenfunction of the LP₀₁ mode in the core m ; and β_m is the phase constant at the angular frequency ω_0 of the optical carrier. Note that the eigenmodes are written in Eq. (2) assuming isolated cores. Nonetheless, as mentioned before, A_m should be assumed z -dependent to model the longitudinal variations induced by the IC-XT in the core modes. Moreover, it can be noted that the MCF perturbations have been omitted in our ansatz (first step of **Figure 1**). In these previous works [33, 45–50], the MCF perturbations will be inserted heuristically¹² in the fourth step with fortunate final results. Now, using Eq. (2) in the MMEs and following the steps detailed in **Figure 1** omitting the MCF perturbations, we obtain the coupled equations of the classical coupled-mode theory (CMT) of an asymmetric and nonlinear optical coupler:

$$j \frac{dA_a(z)}{dz} = k_{ab} \exp(-j\Delta\beta_{ba}z) A_b(z) + q_{1a} |A_a(z)|^2 A_a(z), \quad (3)$$

and a similar expression is found for $dA_b(z)/dz$. In Eq. (3), k_{ab} is the linear coupling coefficient, q_{1a} is the self-coupling nonlinear coefficient and $\Delta\beta_{ba} := \beta_b(\omega_0) - \beta_a(\omega_0)$. In general, additional linear and nonlinear coupling coefficients appear in Eq. (3) [50]. However, considering that the core pitch is usually higher than four times de core radius in CC- and UC-MCFs, these

¹¹Note that in Eq. (2) we have employed a different function for the complex envelope as in Eq. (1). We will use $A(z, t)$ to describe the complex envelope in the non-monochromatic regime (optical pulses) and $A(z)$ in the monochromatic regime (continuous waves). Both functions are related as indicated in Section 3.3.

¹²This strategy is mathematically questionable. Note that the propagation constants are assumed invariant in the ansatz [Eq. (2)], but once we derive the coupled equations, we will assume that the MCF perturbations modify the propagation constants. Although the final estimation of the IC-XT is in line with the experimental results in [47-51], in Section 3.2 we will solve this mathematical inconsistency.

coupling coefficients can be neglected [50]. The predominant coupling coefficients describe the linear and nonlinear mode-coupling: k_{ab} models the linear mode overlapping between the transversal eigenfunctions F_a and F_b , and q_{1a} allows us to investigate the self-coupling effect in the nonlinear regime (analog to the self-phase modulation which can be observed when propagating optical pulses in a single-core fiber). At this point, the MCF perturbations can be described by modifying heuristically the exponential term in Eq. (3) as follows:

$$\exp(-j\Delta\beta_{ba}z) \rightarrow \exp(-j\Delta\phi_{ba}(z)) = \exp\left(-j\int_0^z \Delta\beta_{ba}^{(eq)}(\tau)d\tau\right), \quad (4)$$

with $\Delta\beta_{ba}^{(eq)}(z) = \Delta\beta_{ba} + \Delta\beta_{ba}^{(B+S)}(z)$, where $\Delta\beta_{ba}^{(B+S)}$ describes the phase fluctuation induced by the MCF perturbations. As can be seen, the temporal fluctuations of the propagation constants are also omitted in Eq. (4) to simplify the first analysis of the IC-XT. The temporal fluctuations of the crosstalk will be discussed later. Hence, the coupled-mode equation in a real MCF is finally found as:

$$j\frac{dA_a(z)}{dz} = k_{ab}\exp(-j\Delta\phi_{ba}(z))A_b(z) + q_{1a}|A_a(z)|^2A_a(z). \quad (5)$$

Remarkably, the revisited CMT constitutes a fundamental tool to estimate numerically the IC-XT in SM-MCFs using the Monte Carlo method [50]. The numerical calculation can also be performed in HA- and TA-MCFs by using Eq. (5) along with the corresponding closed-form expression of the linear coupling coefficient k_{ab} detailed in [51]. Furthermore, the revisited CMT allows us to derive the closed-form expressions of the IC-XT cumulative distribution function (cdf), probability density function (pdf), mean and variance in the linear and nonlinear regimes. Although the details of the mathematical discussion can be found in [33] for the linear regime and in [50] for the nonlinear regime, let us summarize the main results of these works.

The starting point is to consider a constant or quasi-constant bending and twisting conditions, i.e. their average value much higher than their longitudinal random fluctuations. In such a case, the phase-mismatching function of Eq. (4) can be expressed as [52]:

$$\Delta\phi_{ba}(z) \approx \Delta\beta_{ba}z - \frac{\beta_a d_{ab}}{2\pi f_T(z)R_B(z)} \sin(2\pi f_T(z)z), \quad (6)$$

where $R_B(z)$ and $f_T(z)$ are the bending radius and the twist rate along the MCF length, respectively¹³. The previous expression is the same as Eq. (2) of [52], but assuming to be null the offset of the twist angle of the core a at $z = 0$. It should be noted that the power exchanged between the cores a and b is maximized at the z -points where phase-mismatching function becomes null. These points are referred to as the phase-matching points (denoted as N_L and N_{NL} in the linear

¹³Eq. (6) is valid if and only if we can assume that $R_B \gg \delta R_B$ and $f_T \gg \delta f_T$ along the MCF length. In other case, Eq. (4) must be solved numerically using the refractive index model of [33].

and nonlinear regime, respectively). In general, in homogeneous SM-MCFs $N_{L(NL)} \neq 0$, but in the heterogeneous case, the phase-matching points can only be observed for a bending radius with an average value¹⁴ R_B lower than the threshold R_{pk} (phase-matching region¹⁵) [33]:

$$R_B < R_{pk} = d_{ab}\beta_a / |\Delta\beta_{ba}|. \quad (7)$$

In the phase-matching region, we can use a first-order solution of Eq. (5) to perform the statistical analysis of the IC-XT [33, 50]. **Table 2** shows the analytical expressions of the linear and nonlinear IC-XT distribution and its statistical parameters derived from the CMT. As can be seen, the measured IC-XT pdf fits correctly to a chi-squared distribution with 4 degrees of freedom. In the linear regime, the mean, variance and N_L are constant with the optical power launch level (P_L). However, in the nonlinear regime, the Kerr effect detunes the phase constant of the core modes as P_L increases in the excited core 3 and, therefore, the homogeneous MCF becomes heterogeneous. As a result, the statistical IC-XT parameters are reduced with $P_L > 2$ dBm, the critical optical power in silica MCFs [49].

Furthermore, note that these statistical parameters can be estimated from the mean of the linear crosstalk $\mu_{L,ab}$. Hayashi, Koshiba and co-workers reported in [47, 48] the closed-form expressions to estimate $\mu_{L,ab}$ in different MCF designs with different bending twisting conditions. For small bending radius with $R_B < R_{pk}$, $\mu_{L,ab}$ can be estimated using Eq. (27) of [48], and for large bending radius with $R_B > R_{pk}$, $\mu_{L,ab}$ can be estimated from Eq. (21)¹⁶ of [47]. In **Table 2** we also include the evolution of $\mu_{L,ab}$ with the average value of the bending radius in a heterogeneous SM-MCF [47]. In the phase-matching region, the mean of the linear IC-XT increases with R_B . However, in the phase-mismatching region, the mean of the linear IC-XT is reduced when R_B increases.

Finally, it should be noted that the statistical analysis previously described is only focused on the random longitudinal evolution of the IC-XT along the MCF considering a single polarization and temporal invariant conditions of the optical medium¹⁷. Hence, the following natural step is to consider temporal varying conditions of the dielectric medium and two polarizations per core.

3.2. Birefringent effects

Now, let us assume a 2-core SM-MCF operating in the monochromatic regime as in the previous section, but considering two polarizations per core and both longitudinal and time-varying random perturbations. These initial assumptions will allow us to predict the different

¹⁴In the following equations, we denote the average value of the bending radius and the twist rate without the usual brackets $\langle \rangle$ to simplify the mathematical expressions, that is, $R_B(z) \equiv R_B + \delta R_B(z)$ and $f_T(z) = f_T + \delta f_T(z)$.

¹⁵Note that $R_{pk} = \infty$ when considering homogeneous cores.

¹⁶In [48], Eq. (21) is given as a function of the correlation length of MCF structural fluctuations. The MCF structural fluctuations are all the medium perturbations except the macrobends. Microbends, fiber twisting or floor vibrations are specific examples of the MCF structural fluctuations.

¹⁷That is, the electrical permittivity is assumed to be temporally invariant.

IC-XT	Equations	Figure/Comments
Probability density function (pdf)	$f_X(x) \approx \frac{(16L^2 q_{1a}^2 P_L^2 x^3 + 4x)}{N_{NL}^2 K_{ab} ^4} \times \exp\left(-\frac{L^2 q_{1a}^2 P_L^2 x^3 + x}{N_{NL} K_{ab} ^2 / 2}\right) u(x)$	
Mean	$\mu_{NL,ab} \approx \frac{\mu_{L,ab}}{1+bLP_L}$ $\mu_{L,ab} \approx \frac{2k_{ab}^2 R_B L}{\sqrt{\left(\frac{\beta_a^{d,ab}}{R_B}\right)^2 - \Delta\beta_{ba}^2}}; R_B < R_{pk}$ $\mu_{L,ab} \approx \frac{2k_{ab}^2 l_c L}{1 + (\Delta\beta_{ba} l_c)^2}; R_B > R_{pk}$	
Variance	$\sigma_{NL,ab}^2 \approx \frac{\mu_{NL,ab}^2}{2} \equiv \frac{\sigma_{L,ab}^2}{(1+bLP_L)^2}$	
Phase-matching points	$N_{NL} \approx \frac{\mu_{NL,ab}}{ K_{ab} ^2} \equiv \frac{N_L}{1+bLP_L}$	

Table 2. Statistical distribution and parameters of the linear and nonlinear IC-XT. L is the MCF length, u is the Heaviside step function, P_L is the power launch level in the excited core b , K_{ab} is the discrete coupling coefficient calculated from Eq. (12) of [33], q_{1a} is the nonlinear coupling coefficient, b is a constant which depends on additional MCF parameters [50] [$b = 0.5$ in the Fibercore SM-4C1500(8.0/125)] and l_c is the correlation length of the autocorrelation function of the MCF structural fluctuations [47].

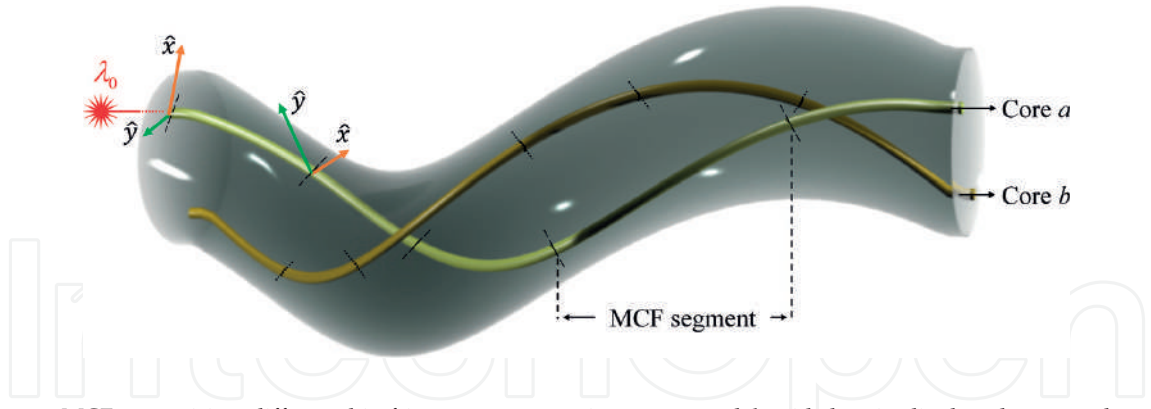


Figure 3. MCF comprising different birefringent segments in cores a and b with longitudinal and temporal varying fluctuations in the first-order electrical permittivity tensor.

crosstalk types between the polarized core modes (PCMs) in a SM-MCF: (i) the intra-core crosstalk (iC-XT) which describes the mode-coupling between orthogonal polarizations in a given core; (ii) the direct inter-core crosstalk (DIC-XT) modeling the mode coupling between the same polarization axis in different cores; and (iii) the cross inter-core crosstalk (XIC-XT) involving mode coupling between orthogonal polarizations in different cores.

As depicted in **Figure 3**, in a real MCF, each core $m = a, b$ can be modeled as a series of birefringent segments with a different time-varying retardation and random orientation of the local principal axes. Therefore, the first-order electrical susceptibility tensor $\chi_{ij}^{(1)}(\mathbf{r}; t)$ will have both spatial and temporal dependence. As a result, in each segment of a given core m , the propagation constant of the polarized core modes (PCMs) LP_{01x} and LP_{01y} presents a different value due to the mentioned slight changes of $\chi_{ij}^{(1)}$, and therefore, the transversal function F_{mi} of each PCM “ mi ” ($i = x, y$) is also found to be spatial and temporal dependent.

In order to model theoretically this scenario, the concept of local mode is included in the perturbation theory. A local mode can be defined as an eigenfunction in a short core segment where the equivalent phase constant $\beta_{mi}^{(eq)}$ and the transversal function F_{mi} are approximately invariant. Hence, each core can be separated in different segments and local modes where the longitudinal and temporal birefringence conditions are approximately constant. In this way, in contrast with the previous section, now the MCF perturbations are considered from the ansatz inserted in the Maxwell equations. Specifically, the ansatz of the global electric field strength of the MCF structure is now written as [53]:

$$\begin{aligned} \mathcal{E}(\mathbf{r}, t) &\approx \sum_{m=a, b} \sum_{i=x, y} \mathcal{E}_{mi}(\mathbf{r}, t) \hat{u}_i \approx \sum_{m=a, b} \sum_{i=x, y} \text{Re}[E_{mi, \omega_0}(\mathbf{r}; t) \exp(j\omega_0 t)] \hat{u}_i \\ &= \sum_{m=a, b} \sum_{i=x, y} \text{Re}[A_{mi}(z; t) F_{mi}(x, y, \omega_0; z, t) \exp(-j\Phi_{mi}(z, \omega_0; t)) \exp(j\omega_0 t)] \hat{u}_i, \end{aligned} \quad (8)$$

where the semicolon symbol is used to separate explicitly longitudinal and temporal changes induced by the slowly varying MCF perturbations. Thus, note that the complex amplitude E_{mi, ω_0} is only a phasor with temporal changes much lower than the temporal oscillation of the optical carrier ($T_0 = 2\pi/\omega_0$). The MCF perturbations and the optical attenuation are described by the complex phase function Φ_{mi} defined as:

$$\begin{aligned} \Phi_{mi}(z, \omega_0; t) &:= \phi_{mi}(z, \omega_0; t) - j\frac{1}{2}\alpha(\omega_0)z = \int_0^z \beta_{mi}^{(eq)}(\delta, \omega_0; t) d\delta - j\frac{1}{2}\alpha(\omega_0)z \\ &= \beta_{mi}(\omega_0)z + \int_0^z \beta_{mi}^{(B+S)}(\delta, \omega_0; t) d\delta - j\frac{1}{2}\alpha(\omega_0)z, \end{aligned} \quad (9)$$

with α modeling the power attenuation coefficient of the MCF (assumed similar in each PCM), and the real phase function ϕ_{mi} involving the ideal phase constant of the PCM and the longitudinal and temporal MCF perturbations. Now, using Eq. (8) and performing the derivation of the perturbation theory as depicted in **Figure 1**, the following coupled local-mode equation is found [53]:

$$\begin{aligned} j\left(\frac{\partial}{\partial z} + \frac{\alpha}{2}\right)A_{ax}(z; t) &= m_{ax, ay}(z; t)\exp(-j\Delta\phi_{ay, ax}(z; t))A_{ay}(z; t) \\ &+ k_{ax, bx}(z; t)\exp(-j\Delta\phi_{bx, ax}(z; t))A_{bx}(z; t) \\ &+ \left(q_{ax}(z; t)|A_{ax}(z; t)|^2 + g_{ax}(z; t)|A_{ay}(z; t)|^2\right)A_{ax}(z; t) \\ &+ \frac{1}{2}g_{ax}(z; t)\exp(-j2\Delta\phi_{ay, ax}(z; t))A_{ax}^*(z; t)A_{ay}^2(z; t), \end{aligned} \quad (10)$$

where $m_{ax, ay}$, $k_{ax, bx}$, q_{ax} and g_{ax} are the coupling coefficients defined in [53]; and the phase-mismatching functions are defined as $\Delta\phi_{ay, ax} := \phi_{ay} - \phi_{ax}$, $\Delta\phi_{bx, ax} := \phi_{bx} - \phi_{ax}$ and $\Delta\phi_{by, ax} := \phi_{by} - \phi_{ax}$. From the above equation, the following considerations are in order:

- In contrast with the previous section, the longitudinal and temporal MCF perturbations are now modeled, not only by the phase-mismatching functions $\Delta\phi(z; t)$, but also by space- and time-varying coupling coefficients¹⁸. This coupled local-mode theory (CLMT) inherently incorporates these stochastic perturbations in both functions, as they were directly included in the Maxwell equations using Eq. (8).
- The CLMT is completed by three additional coupled local-mode equations for the ay , bx and by PCMs, which can be obtained just by exchanging the corresponding subindexes in Eq. (10). The herein presented theory is a general model which can be applied to SM-MCFs comprising: coupled or uncoupled cores, lowly or highly birefringent cores, trench-assisted, hole-assisted, and with gradual-index or step-index profile. In SM-CC-MCFs with a core pitch value (d_{ab}) lower than three times the maximum core radius ($R_0 = \max\{R_{0a}, R_{0b}\}$), additional nonlinear terms modeling cross-coupling effects should be included in Eq. (10). However, if we assume a MCF with $d_{ab} \gg 3R_0$, the self-coupling effect is the predominant nonlinear coupling effect and the additional nonlinear terms can be neglected [53].

¹⁸Note that the explicit dependence with ω_0 has been omitted in the phase-mismatching functions and in the coupling coefficients for the sake of simplicity.

- The monochromatic equivalent refractive index model (ERIM) reported in [53] must be used to calculate numerically the coupling coefficients and the phase-mismatching functions. Thanks to the CLMT and the ERIM, we will observe that the temporal birefringence fluctuation of each core modifies the average value of the iC-, DIC- and XIC-XT.

First, in order to analyze the longitudinal MCF random perturbations induced by MCF bending and twisting, a Monte Carlo simulation was performed using the CLMT along with the ERIM considering a 2-m SI-SM-HO-UC-LB-2CF with cores a and b comprising a single birefringent segment with the same birefringence average value of $\langle \Delta n_{aj} \rangle = \langle \Delta n_{bj} \rangle = 10^{-7}$ (see the specific fiber parameters in [53]). The temporal birefringence fluctuation of the 2CF was omitted in this simulation. The numerical results are shown in **Figure 4**, where we can observe the behavior of the mean of the iC-XT $ay-ax$ DIC-XT $bx-ax$ and XIC-XT $by-ax$ when changing the bending radius R_B and fiber twisting conditions f_T .

As it can be noticed from **Figure 4(a)**, we cannot observe intra-core mode-coupling between $ax-ay$ with $f_T = 0$ in 2 m of the MCF. Macrobending increases the phase-mismatching between the PCMs ax and ay without inducing iC-XT due to the photo-elastic effect [54]. As a result, significant XIC-XT cannot be observed for short MCF lengths when $f_T = 0$, as in the case of **Figure 4(c)**. Nevertheless, an average level of DIC-XT between -100 and -50 dB can be noted from **Figure 4(b)** in non-twisting conditions depending on the R_B value. In addition, the higher the twist rate and the bending radius, the higher the iC-, DIC- and XIC-XT mean due to the reduction of the phase-mismatching between the different PCMs of the 2CF. Note that DIC- and XIC-XT means are balanced when the iC-XT mean achieves the value of 0 dB in **Figure 4(a)**. Therefore, MCF twisting can be proposed as a potential strategy for birefringence management to balance the inter-core crosstalk between the different PCMs for short MCF distances. For MCF distances of several kilometers, the iC-XT mean will be increased and the difference between the mean of the DIC- and XIC-XT will be reduced.

In addition, experimental measurements were performed on a 4CF [Fibercore SM-4C1500 (8.0/125)] analyzing the temporal birefringence of the optical media and its impact on the mean of the crosstalk between the PCMs of the cores 1 and 3. **Figure 5** shows the temporal fluctuation of the linear birefringence and the crosstalk mean behavior between the PCMs of cores 1

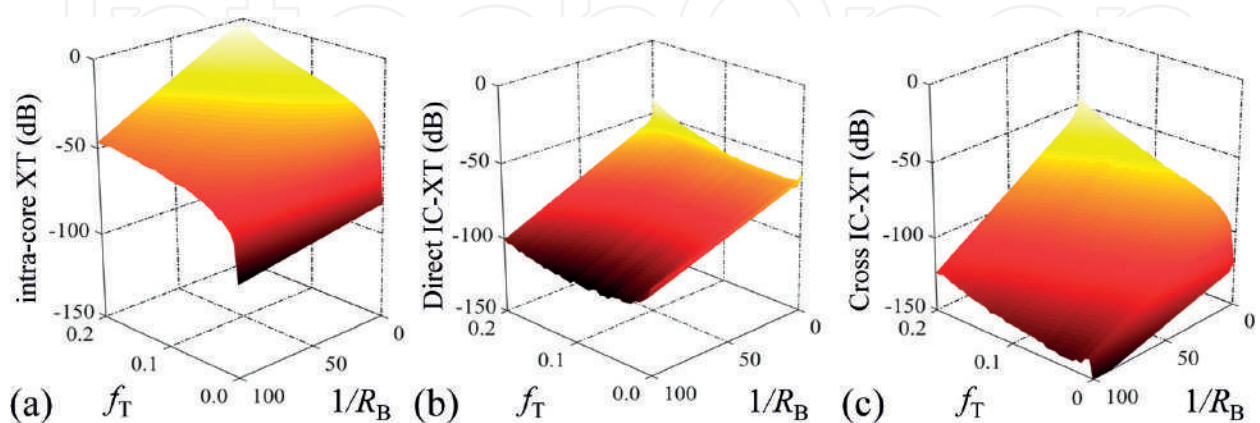


Figure 4. Numerical simulation of the crosstalk between PCMs varying the bending radius and the twist rate in a 2-m SI-SM-HO-UC-LB-2CF: (a) iC-XT mean $ay-ax$, (b) DIC-XT mean $bx-ax$, and (c) XIC-XT mean $by-ax$.

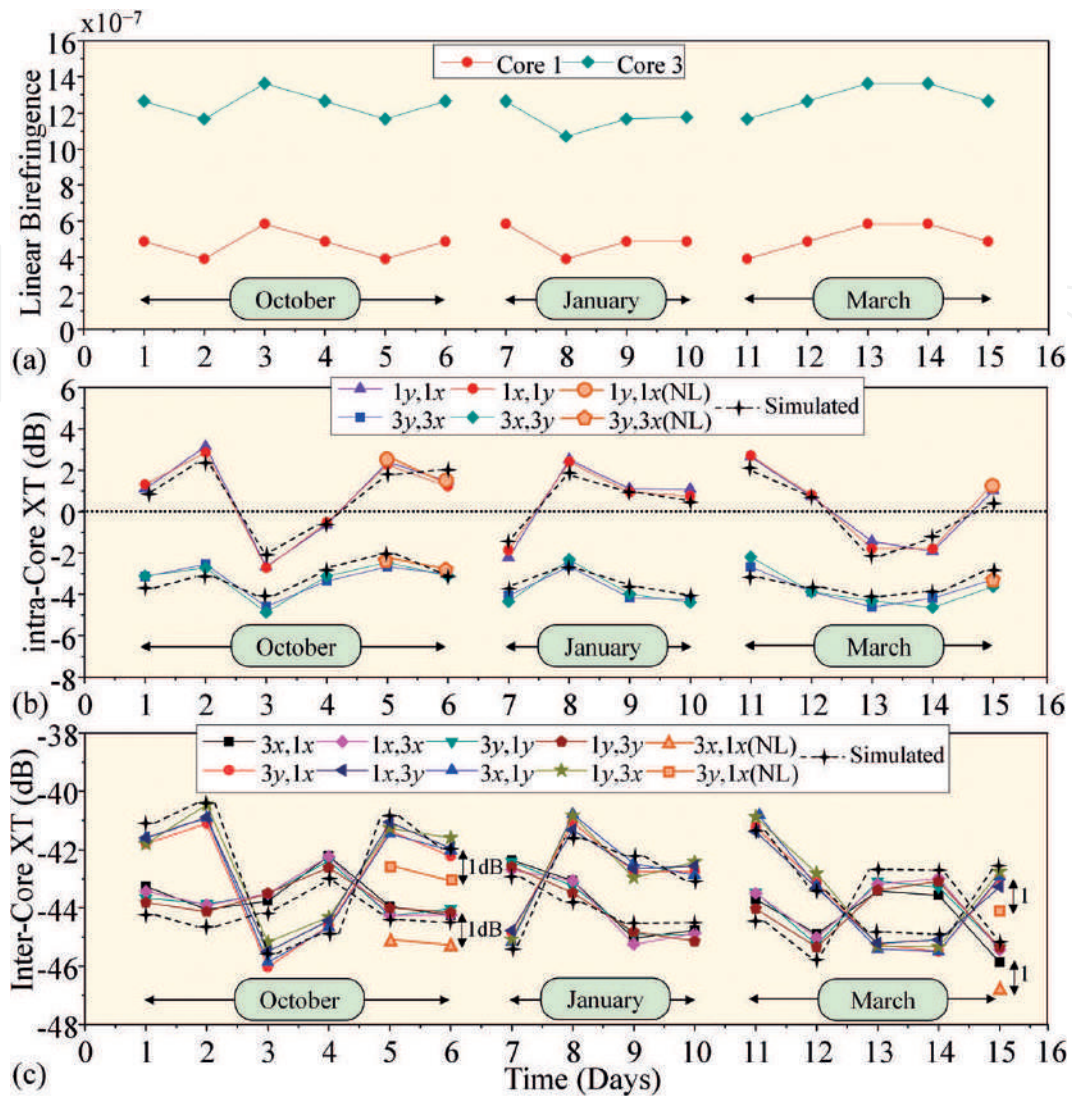


Figure 5. Experimental results of the temporal linear birefringence fluctuation over different days and months of a 150-m 4CF, and corresponding intra- and inter-core crosstalk mean between cores 1 and 3 (NL: nonlinear regime). (a) Linear birefringence of the cores 1 and 3, (b) iC-XT and (c) DIC- and XIC-XT. Results based on [53].

and 3 measured in different days and months¹⁹. As shown in **Figure 5(a)**, cores 1 and 3 present a different average value of the linear birefringence estimated to be $\langle \Delta n_{1,j} \rangle = 4.9 \cdot 10^{-7}$ and $\langle \Delta n_{3,j} \rangle = 1.2 \cdot 10^{-6}$, respectively ($j = 1, \dots, 15$). It can be noted that the average value of the linear birefringence is found to be constant in each core the three different measured months. Moreover, although the average value of the linear birefringence is different in each core, the temporal evolution of the linear birefringence presents a similar shape in both cores. As can be seen from **Figure 5(a)** and **(b)**, the higher the linear birefringence in a given core, the lower the mean of the iC-XT. Furthermore, it should be noted that iC-XT in core 3 is lower than in core 1 due to a higher index-mismatching between the orthogonal polarizations. Remarkably,

¹⁹As the linear birefringence of each core remains unchanged during more than 10 hours in the laboratory room, we analyzed the temporal birefringence fluctuation in different days and months, with similar temperature conditions in the laboratory.

the iC-XT mean presents a lower temporal fluctuation in the more birefringent core (core 3), which occurs when the average value of the birefringence is higher than the temporal random birefringence fluctuation ($\sim 10^{-7}$). In addition, we can observe from **Figure 5(c)** that the temporal evolution of the XIC-XT mean presents the same behavior as the iC-XT mean, indicating that XIC-XT depends directly on the iC-XT of both cores. As a result, DIC-XT is higher than XIC-XT when iC-XT is lower than 0 dB in both cores. The nonlinear crosstalk between de PCMs $1y-1x$, $3y-3x$, $3x-1x$ and $3y-1x$ was also measured the 5th, 6th and 15th days with a power launch level of 6 dBm. The DIC- and XIC-XT mean is reduced around 1 dB keeping constant the difference between both inter-core crosstalk types as a direct consequence of the constant behavior of the iC-XT mean in nonlinear regime. Finally, note that the experimental measurements of **Figure 5** fit correctly with the CLMT when using the simulation parameters detailed in [53].

Additional numerical calculations of the CLMT can be found in [53] involving both LB and HB cores. Interesting, it is worth mentioning that the CLMT and the ERIM can be used to design HB-MCFs with random orientation of the principal axes between adjacent cores to reduce the mode-coupling between their PCMs. The concept is similar to the crosstalk behavior which can be found in disordered MCFs exhibiting transverse Anderson localization [21]. Along this line, a TA- and HA-cladding can also be considered in these fibers to obtain low DIC- and XIC-XT levels. In all these scenarios, the CLMT can be used in the design work, with a lower computational time than numerical simulations based on FDTD (Finite-Difference Time Domain) calculations.

The temporal fluctuation of the crosstalk has also been investigated in [55], but considering a single polarization per core and inserting heuristically the MCF perturbations in the exponential terms of the CMT, in line with the initial crosstalk works [33, 45–50]. Specifically, in ref. [55], the crosstalk transfer function has been discussed at the MCF output considering small modulated signals, i.e. non-monochromatic electric fields. However, the comprehension of the MCF propagation and the IC-XT in the non-monochromatic regime is not as straightforward as initially foreseen. Hence, at this point, let us discuss the non-monochromatic regime with a similar rigorous formalism as in [53] for the monochromatic case.

3.3. Intermodal dispersion and higher-order coupling and nonlinear effects

The theoretical study of the non-monochromatic regime will allow us to describe the propagation of optical pulses through a MCF. Focusing our efforts on SM-MCFs, additional physical impairments should be included in Eq. (10), such as the group-velocity dispersion (GVD), polarization-mode dispersion (PMD), intermodal dispersion and additional nonlinear effects. Moreover, if we also consider the propagation of ultra-short optical pulses in the femtosecond regime, the analysis of higher-order coupling and nonlinear effects should also be incorporated to the coupled equations.

Although in the picosecond regime MCF propagation models have been proposed in [56, 57] including polarization effects and the random longitudinal fiber perturbations (but omitting the temporal fluctuations), in the femtosecond regime, existing MCF propagation models exclude polarization effects and omit both temporal and longitudinal random perturbations

of the fiber [58–60]. In order to include these realistic fiber conditions in the mathematical description of the propagation of femtosecond optical pulses through a MCF, a theoretical model is proposed in [61] based on the concept of local modes. As can be seen later, the intermodal dispersion induced by the MCF random perturbations can become one of the major physical impairment in the single-mode regime of the fiber. Specifically, the intermodal dispersion, also referred to as the mode-coupling dispersion (MCD) in this work, is induced in the femtosecond regime not only by the mismatching between the propagation constants of the PCMs, but also by the frequency dependence of their mode overlapping.

Our initial goal is to revisit the CLMT of the previous section but now assuming non-monochromatic fields. In such a case, the ansatz of the global electric field strength of a SM-MCF should be written as:

$$\mathcal{E}(\mathbf{r}, t) \approx \sum_{m=a, b} \sum_{i=x, y} \mathcal{E}_{mi}(\mathbf{r}, t) \hat{u}_i \approx \sum_{m=a, b} \sum_{i=x, y} \text{Re} [E_{mi, \omega_0}(\mathbf{r}, t) \exp(j\omega_0 t)] \hat{u}_i, \quad (11)$$

where the complex amplitude E_{mi, ω_0} is now a bandpass signal with the slowly varying temporal changes of the electric field strength, given by the expression:

$$E_{mi, \omega_0}(\mathbf{r}, t) = \frac{1}{2\pi} \int \tilde{A}_{mi}(z, \omega - \omega_0; t) F_{mi}(x, y, \omega; z, t) \times \exp[-j\Phi_{mi}(z, \omega; t)] \exp[j(\omega - \omega_0)t] d\omega. \quad (12)$$

The functions involved in the previous equations are the same as in Eq. (8), but now expressed in the frequency domain. Nevertheless, a fundamental remark of the complex envelope should be taken into account at this point. As previously discussed in **Figure 1**, the slowly varying longitudinal changes should also be decoupled from the rapidly varying longitudinal fluctuations via the complex envelope. However, in Eq. (12) the rapidly and slowly varying longitudinal changes are coupled in the first exponential term via the function $\phi_{mi}(z, \omega; t)$. Therefore, in order to decouple them and model the analytic function of the optical pulses, the complex envelope should be rewritten as:

$$\tilde{\mathcal{A}}_{mi}(z, \omega - \omega_0; t) = \tilde{A}_{mi}(z, \omega - \omega_0; t) \exp[-j(\phi_{mi}(z, \omega; t) - \phi_{mi}(z, \omega_0; t))]. \quad (13)$$

Once we have written our ansatz of the global electric field strength, the following step is to propose the wave equation of the PCMs (second step) and the wave equation of the MCF (third step). In particular, in the third step, we will be able to incorporate the higher-order nonlinear effects via the constitutive relation between the global electric field strength and the nonlinear polarization. Note that in the femtosecond regime, the aforementioned constitutive relation should include the delay response of the electronic and nuclei structure of silica atoms [62]. For optical frequencies well below the electronic transitions, the electronic contribution to the nonlinear polarization can be considered instantaneous. However, since nucleons (protons and neutrons) are considerably heavier than electrons, the nuclei motions have resonant frequencies much lower than the electronic resonances and, consequently, they should be retained in the constitutive relation as indicated in Eq. (S36) of [61]. Specifically, Raman

scattering is a well-known effect arising from the nuclear contribution to the nonlinear polarization. All in all, the coupled local-mode equations can be derived to describe the propagation of ultra-short pulses in SM-MCFs. In particular, the coupled local-mode equation modeling the propagation of the PCM ax is found to be [61]:

$$\begin{aligned}
j\left(\frac{\partial}{\partial z} + \widehat{D}_{ax}^{(eq)} + \frac{1}{2}\widehat{\alpha}\right)\mathcal{A}_{ax}(z, t) &= \widehat{M}_{ax, ay}^{(eq)}\mathcal{A}_{ay}(z, t) + \sum_{m=b}^N \widehat{K}_{ax, mx}^{(eq)}\mathcal{A}_{mx}(z, t) \\
&+ \widehat{q}_{ax}^{(I)}\left(|\mathcal{A}_{ax}(z, t)|^2\mathcal{A}_{ax}(z, t)\right) + \frac{2}{3}\widehat{g}_{ax, ay}^{(I)}\left(|\mathcal{A}_{ay}(z, t)|^2\mathcal{A}_{ax}(z, t)\right) \\
&+ \frac{1}{3}\exp\left(-j2\Delta\phi_{ay, ax}^{(0)}(z; t)\right)\widehat{g}_{ax, ay}^{(I)}\left(\mathcal{A}_{ax}^*(z, t)\mathcal{A}_{ay}^2(z, t)\right) \\
&+ \widehat{q}_{ax}^{(R)}\left[\left(f(t)*|\mathcal{A}_{ax}(z, t)|^2\right)\mathcal{A}_{ax}(z, t)\right] + \widehat{g}_{ax, ay}^{(R)}\left[\left(h(t)*|\mathcal{A}_{ay}(z, t)|^2\right)\mathcal{A}_{ax}(z, t)\right] \\
&+ \frac{1}{2}\widehat{g}_{ax, ay}^{(R)}\left\{\left[u(t)*\left(\mathcal{A}_{ax}(z, t)\mathcal{A}_{ay}^*(z, t)\right)\right]\mathcal{A}_{ay}(z, t)\right\} \\
&+ \frac{1}{2}\exp\left(-j2\Delta\phi_{ay, ax}^{(0)}(z; t)\right)\widehat{g}_{ax, ay}^{(R)}\left\{\left[u(t)*\left(\mathcal{A}_{ax}^*(z, t)\mathcal{A}_{ay}(z, t)\right)\right]\mathcal{A}_{ay}(z, t)\right\}.
\end{aligned} \tag{14}$$

where $\widehat{D}_{ax}^{(eq)}$ is the equivalent dispersion operator in the PCM ax including the frequency dependence of the MCF perturbations in the time domain; $\widehat{\alpha}$ is the attenuation operator; the h and u functions describe the isotropic and anisotropic Raman response, respectively; the f function is $f = h + u$; the phase-mismatching term $\Delta\phi_{ay, ax}^{(0)}(z; t) := \phi_{ay}(z, \omega_0; t) - \phi_{ax}(z, \omega_0; t)$ describes the phase-mismatching between the PCMs ax and ay at ω_0 ; $\widehat{M}_{ax, ay}^{(eq)}$ and $\widehat{K}_{ax, mx}^{(eq)}$ are, respectively, the equivalent intra- and inter-core mode-coupling dispersion operators between the PCMs ax - ay and ax - mx ; $\widehat{q}_{ax}^{(I)}$ and $\widehat{g}_{ax, ay}^{(I)}$ are the nonlinear mode-coupling dispersion operators associated with the instantaneous response of the nonlinear polarization and accounting for the nonlinear mode overlapping between the PCMs ax - ax and ax - ay ; and $\widehat{q}_{ax}^{(R)}$ and $\widehat{g}_{ax, ay}^{(R)}$ are analogous to $\widehat{q}_{ax}^{(I)}$ and $\widehat{g}_{ax, ay}^{(I)}$, but associated with the nonlinear polarization induced by the delay response of the nuclei motion of silica atoms (Raman effect). A comprehensive description of the main parameters of the model can be found in [61].

It should be remarked that the linear operators of Eq. (14) are found to be longitudinal and temporal dependent, instead of constant coupling coefficients and unperturbed propagation constants. Thanks to these linear operators, Eq. (14) is able to describe accurately the linear and nonlinear propagation of each PCM and the linear and nonlinear MCD including the longitudinal and temporal MCF perturbations. Furthermore, it is worthy to note that the MCD is induced in each birefringent segment by two different dispersive effects when propagating femtosecond optical pulse through a MCF: (i) the frequency dependence of the local mismatching between the phase functions $\phi_{mi}(z, \omega; t)$ of the PCMs, referred to as the phase-mismatching dispersion (PhMD); and (ii) the frequency dependence of the mode overlapping between the PCMs, modeled by the coupling coefficients and referred to as the coupling coefficient dispersion (CCD). As an example, the PhMD between the PCMs ax and mx is given by the phase-mismatching $\Delta\phi_{mx, ax}(z, \omega; t)$ and the CCD by the coupling coefficients

$\tilde{k}_{ax,mx}(z, \omega; t)$ and $\tilde{k}_{mx,ax}(z, \omega; t)$, both dispersive effects modeled by the operators $\hat{D}_{ax}^{(eq)}$, $\hat{D}_{mx}^{(eq)}$, $\hat{K}_{ax,mx}^{(eq)}$ and $\hat{K}_{mx,ax}^{(eq)}$. Note that the equivalent dispersion operators $\hat{D}_{ax}^{(eq)}$ and $\hat{D}_{mx}^{(eq)}$ describe not only the linear propagation of the PCMs ax and mx , but also the exact phase-mismatching $\Delta\phi_{mx,ax}(z, \omega; t)$ at each angular frequency ω at a given z point. The MCD can be observed in a SM-MCF between the PCMs of different cores (inter-core MCD) and between the PCMs of a single core (intra-core MCD). Note that the intra-core MCD is the well-known linear and nonlinear polarization-mode dispersion (PMD). Hence, we will discuss in this subsection the inter-core MCD (IMCD) involving the mode-coupling between the PCMs of different cores.

Although the proposed model allows us to investigate a wide range of propagation phenomena in MCFs, our efforts are mainly focused on a deeper understanding of the IMCD induced by the fiber perturbations. In order to clarify the impact of the MCF birefringence on this physical impairment when propagating femtosecond optical pulses, Eq. (16) is solved numerically in the linear and nonlinear regime of the fiber. In all the analyzed cases, we considered a MCF comprising a fiber length of $L = 40$ m and two cores a and b distributed in a square lattice as in the Fibercore SM 4C1500(8.0/125) but with a core-to-core distance $d_{ab} = 26 \mu\text{m}$. The wavelength of the optical carrier λ_0 was selected to be in the third transmission window with $\lambda_0 = 1550$ nm. The time variable was normalized using the group delay of the PCM ax as a reference with $t_N = (t - \beta_{ax}^{(1)}z)/T_P$, where T_P is defined in this work as the full width at $1/2e$ (~18%) of the peak power.

As a first simple example, we considered an ideal homogeneous MCF, with $R_B = \infty$ and $f_T = 0$ turns/m. **Figure 6(a)** shows the simulation results of the CLMT when a 350-fs Gaussian optical pulse is launched into the PCM ax at $z = 0$. In this example, the GVD and the PMD (induced by the intrinsic random fiber birefringence) were omitted to isolate the effects of the first-order

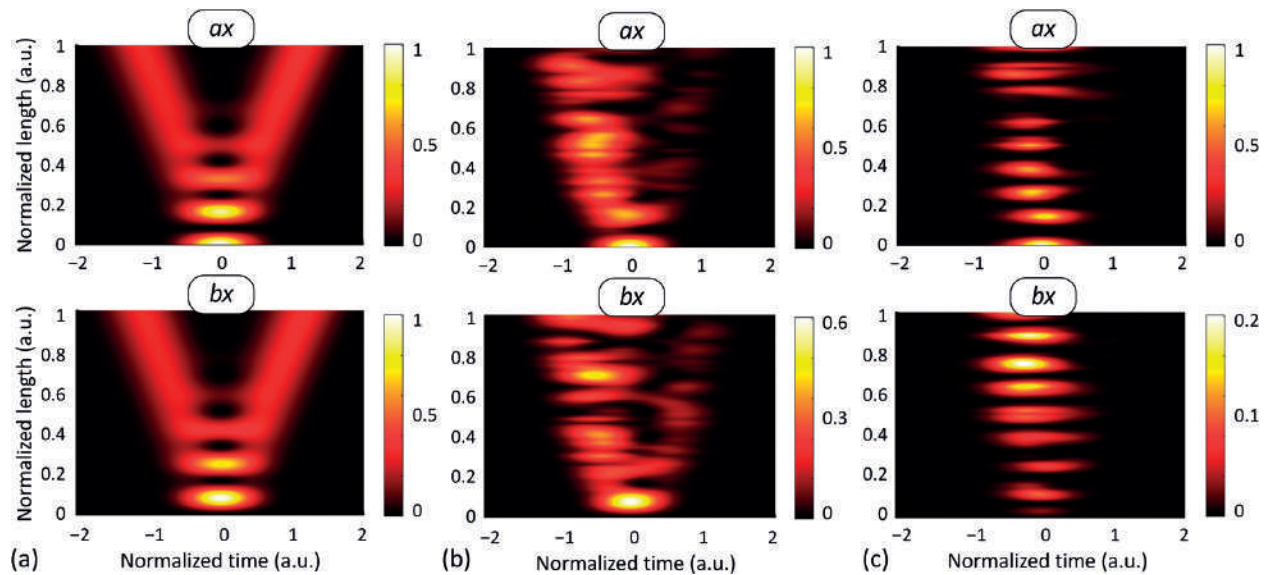


Figure 6. IMCD impact on Gaussian pulses and optical solitons propagating through a SM-MCF. (a) 350-fs Gaussian optical pulse propagation under ideal conditions. (b) 250-fs Gaussian optical pulse propagation with random bending conditions. (c) 600-fs fundamental bright soliton with random bending and twisting conditions. The numerical results for the PCMs ay and by can be found in [61].

IMCD. In this way, the pulse is only propagated by the PCMs ax and bx . Remarkably, the pulse splitting predicted by Chiang et al. in [58] appears induced by the first-order CCD: each spectral component of the pulse presents a different coupling length as a direct consequence of the linear frequency dependence of the power confinement ratio of the LP01 mode in each core. As a result, the pulse propagation can be modeled in this case by two linear and time-invariant systems with the impulse response proportional to the Dirac delta functions $\delta(t \pm Kz)$, where K is the first-order frequency derivative of the coupling coefficient between the PCMs ax and bx .

Another interesting effect of the first-order IMCD is related to the random birefringence that arises from a randomly varying fiber bending radius. In this case, the effect of the first-order PhMD along with the CCD can also be observed when considering a high number of MCF birefringent segments where the bending radius fluctuates with a Normal distribution between adjacent segments. We simulate the MCF of the first example considering a 250-fs Gaussian optical pulse and 50 birefringent segments with a bending radius Normal distribution $R_B = N(\mu = 100, \sigma^2 = 40)$ cm. The numerical results are shown in **Figure 6(b)**. It can be seen that the group delay and the pulse splitting present a random evolution in each core due to the stochastic nature of the MCF perturbations inducing a random differential group delay between the PCMs ax and bx . In particular, this result can be employed for pulse shaping and dispersion engineering applications.

In the third example, the IMCD effects are also investigated in the nonlinear fiber regime along with the PMD (intra-core MCD). Specifically, the impact of such perturbations on a bright soliton is analyzed. A 600-fs fundamental soliton (~ 350 fs full width at half maximum) was launched into the PCM ax of a dispersion-shifted homogeneous 2-core MCF with usual GVD parameters of $\beta^{(2)} = -1$ ps²/km and $\beta^{(3)} = 0.1$ ps³/km. The peak power (P_0) required to support the fundamental soliton is found to be around ~ 40 dBm considering a nonlinear refractive index of $n_{NL} = 2.6 \cdot 10^{-20}$ m²/W at 1550 nm. In order to simulate realistic MCF conditions, we assume $\Delta\beta_{bx,ax}^{(1)} = 0.2$ ps/km and $\Delta\beta_{bx,ax}^{(2)} = 0.1$ ps²/km induced by manufacturing imperfections (similar values for the y -polarization). In this case, we also include the intrinsic linear birefringence of the medium along with the linear and circular birefringence induced by the fiber bending and twisting conditions. We consider 50 birefringent segments along the MCF length, where the linear and circular birefringence fluctuate between adjacent segments. The circular birefringence is induced by a random twist rate f_T given by the Normal distribution $f_T = N(\mu = 0.1, \sigma^2 = 0.01)$ turns/m. The linear birefringence is induced by: (i) the random bending conditions with $R_B = N(\mu = 100, \sigma^2 = 40)$ cm; and (ii) the intrinsic linear birefringence of each core, fixed to $2 \cdot 10^{-7}$ in both cores a and b . According to **Figure 6(c)**, we can observe that the soliton condition is broken along the MCF propagation. The second-order PhMD becomes the main physical impairment when $\Delta\beta_{bx,ax}^{(2)} \neq 0$ in dispersion-shifted coupled-core MCFs, with a reduced second-order GVD coefficient and core-to-core distance. Therefore, in the first propagation meters, the additional chirp induced by the second-order PhMD along with the first-order CCD increases the pulse width and reduces the peak power. As a result of the peak power reduction, the pulse width is increased along the MCF length and the soliton peak is shifted from its original position due to the first-order PhMD and the third-order GVD. In this case, note that the effects of the Raman-induced frequency shift (RIFS) [63] and the self-

steepening are difficult to observe with $T_P = 600$ fs, $L = 40$ m, $\beta^{(2)} = -1$ ps²/km, and $P_0 \approx 40$ dBm. Nevertheless, in optical pulses of few femtoseconds and in MCFs with a higher second-order GVD coefficient, the soliton distortion will be increased not only by the IMCD and the third-order GVD, but also by the RIFS and the self-steepening nonlinear effects.

Although we have only discussed the main effects of the longitudinal birefringence of the MCF, the analysis of the temporal perturbations of the medium can be found in [61]. It should be noted that the IMCD can also fluctuate in time due to the temporal fluctuation of the MCF birefringence modifying the value of the phase functions $\phi_{mi}(z, \omega; t)$ for the PCM mi . Therefore, the random group delay induced by the first-order PhMD in each MCF segment may present a time-varying evolution.

For completeness, we investigate the fiber length scales over which the dispersive effects of the IMCD should be considered in the pulse propagation phenomena when comparing this physical impairment with the GVD. To this end, we compare the GVD, CCD and PhMD lengths considering a MCF without random perturbations, given by the expressions for the PCMs ax and bx [61]:

$$L_{\text{GVD}} := T_P^2 / |\beta_{ax}^{(2)}|; \quad L_{\text{CCD}} := T_P / 2 |\tilde{k}_{ax, bx}^{(1)}|; \quad L_{\text{PhMD}} := T_P^2 / |\Delta\beta_{bx, ax}^{(2)}|. \quad (15)$$

Figure 7 depicts the comparison of the GVD, CCD and PhMD dispersion lengths. As can be seen, the IMCD induced by the CCD becomes the predominant impairment in dispersion-shifted coupled-core MCFs with a reduced core-to-core distance and $\Delta\beta_{bx, ax}^{(2)} = 0$. On the other hand, the GVD is expected to become the major physical impairment in homogeneous uncoupled-core MCFs, with a core-to-core distance d_{ab} higher than 30 μm and $\Delta\beta_{bx, ax}^{(2)} \approx 0$, or in heterogeneous MCFs with inter-core crosstalk levels lower than -30 dB. Nevertheless, the GVD along with the IMCD induced by the second-order PhMD will be the predominant physical impairments in homogeneous coupled-core MCFs with $\Delta\beta_{bx, ax}^{(2)} \neq 0$.

Finally, it should be noted that the extension of Eq. (14) to the multi-mode regime is straightforward when including additional LP mode groups in the complex amplitude of the global electric field strength $E_{i, \omega 0}$. Inserting $E_{i, \omega 0}$ in the Maxwell equations, the CLMT can be extended

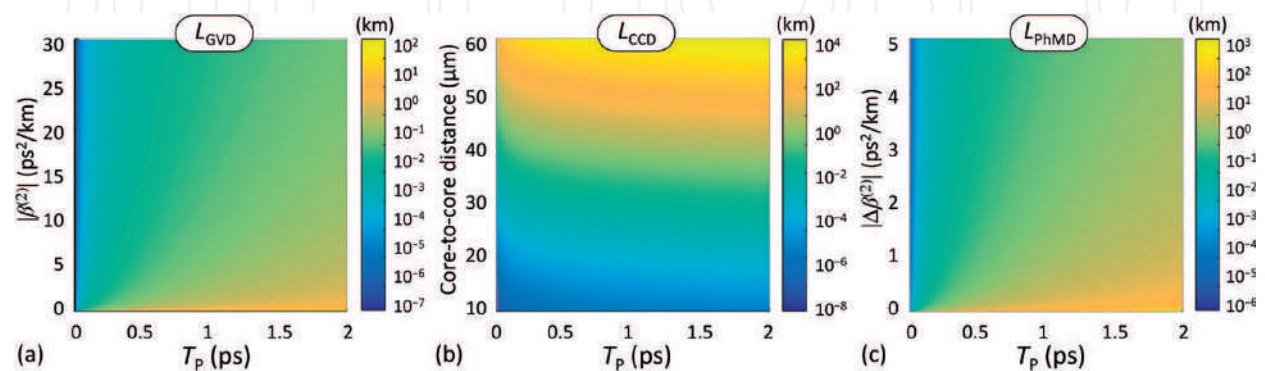


Figure 7. Comparison of the dispersion lengths. (a) Group-velocity dispersion (GVD) length, (b) coupling coefficient dispersion (CCD) length, and (c) phase-mismatching dispersion (PhMD) length.

to the multi-mode regime performing a similar mathematical discussion as in [61] in the single-mode regime.

4. Current and emerging applications

Once we have reviewed the fundamental aspects of the linear and nonlinear propagation in MCF media, we will discuss in this section the main applications and opportunities of the MCF technology in photonics and diverse branches of sciences.

4.1. Backbone and access optical networks using multi-core fibers

SDM systems using MCFs have been extensively investigated in recent years targeting to overcome the exponential growth of data traffic in the backbone and in the access network [4–7].

The first laboratory MCF transmission was demonstrated in May 2010 [64]. Zhu and co-workers used a SI-SM-HO-UC-LB-7CF with a hexagonal lattice. A novel network configuration was proposed for passive optical network (PON) based on a bidirectional parallel transmission at 1310 nm and 1490 nm and using a tapered MCF connector (TMC) for injecting and extracting the optical signals in the MCF.

A set of MCF experiments were reported since 2011. Scaling in capacity demonstrations, [65–67] should be mentioned. In [65] the authors demonstrated a 210 Tb/s self-homodyne transmission system using distributed feedback (DFB) lasers and a 19-core TA-SM-HO-UC-LB-MCF. Sakaguchi et al. reported in [66] a record capacity of 305 Tb/s over 10.1 km using the same MCF as in [65], with an IC-XT mean of -32 dB between adjacent cores at 1550 nm. The authors also fabricated a 19-channel SDM multiplexer/demultiplexer using free-space optics with low insertion losses and low additional crosstalk. As another interesting example, Takara et al. reported in [67] 1.01 Pb/s transmission over 52 km with the highest aggregate spectral efficiency of 91.4 b/s/Hz by using a one-ring-structured 12-core TA-SM-HO-UC-LB-MCF. They generated 222-channel WDM signals of 456-Gb/s PDM-32QAM-SC-FDM signals²⁰ with 50-GHz spacing in the C and L bands. Following significant efforts on the design and fabrication of MCFs, demonstrations of SDM transmissions using MCF media for long-haul applications have shown impressive progress in terms of capacity, reach, and spectral efficiency, as detailed in **Table 3**.

On the other hand, cloud radio-access network (C-RAN) systems should also deal with this huge future capacity demand in the next-generation wireless systems, e.g. 5G cellular technology and Beyond-5G [75–77]. According to some telecom equipment manufacturers, it is expected that 5G cellular networks will be required to provide 1000 times higher mobile data traffic in 2025 as compared with 2013, including flexibility and adaptability solutions to maximize the energy efficiency of the network [78, 79]. A new radio-access model supporting

²⁰PDM: Polarization-Division Multiplexing, QAM: Quadrature Amplitude Modulation, SC: Single Carrier, FDM: Frequency-Division Multiplexing.

Year	Ref.	Fiber type	Cores \times modes	Distance (km)	Channel rate (Gb/s)	WDM channels per core	S/E (b/s/Hz)	Total capacity (Tb/s)
2011	[68]	SM-MCF	7×1	2688	128	10	15	7
2012	[67]	SM-MCF	12×1	52	456	222	91.40	1012
2012	[66]	SM-MCF	19×1	10.1	172	100	30.50	305
2013	[65]	SM-MCF	19×1	10.1	100	125	33.60	210
2014	[7]	FM-MCF	7×2	1	4000	50	102	200
2015	[69]	SM-MCF	7×1	2520	100	73	16	51
2015	[70]	FM-MCF	36×2	5.5	107	40	108	432
2015	[71]	FM-MCF	12×2	527	80	20	90.28	45
2015	[72]	FM-MCF	19×4	9.8	40	8	345	29
2016	[73]	FM-MCF	19×4	9.8	60	360	456	2050
2017	[74]	SM-MCF	32×1	205.6	768	46	217.6	1001

Table 3. Summary of progress in MCF transmissions in recent years. The MCF type indicates only the modal regime (additional characteristics of the MCF involving the index profile, the spatial homogeneity, the core pitch and the birefringence can be found in the corresponding reference). The number of modes indicate the number of LP mode groups supported by the MCF transmission. The channel rate includes PDM and the overhead for forward-error-correction (FEC). The spectral efficiency and total capacity exclude the FEC overhead.

massive data uploading will be required considering additional transport facilities provided by the physical layer [78–80].

Fronthaul connectivity performed by radio-over-fiber (RoF) transmission using single-input single-output (SISO), multiple-input multiple-output (MIMO) configuration [81], sub-Nyquist sampling [82], and ultra-wideband signals exceeding 400 MHz bandwidth has been proposed for the 5G cellular generation [76, 77, 83]. The required channel capacity is further extended in the case of Beyond-5G systems, where a massive number of antennas operating in MIMO configuration, should be connected using RoF. To overcome the massive increment in the data capacity demand, MCF has been recently proposed as a suitable medium for LTE-Advanced (LTE-A) MIMO fronthaul systems [52, 83, 84].

MCFs open up attractive possibilities in RoF systems as different wireless signals can be transmitted simultaneously over the same optical wavelengths and electrical frequencies in different cores of the optical waveguide to provide multi-wireless service using a single laser at the transmitter. Thus, MCF can also be proposed as an alternative to the classical SM-SCF [also termed in the literature as the standard single-mode fiber (SSMF)] providing fronthaul connectivity using multiple wavelength channels with multiple lasers. Additionally, MCFs with high core density are suitable for connecting large phase array antennas performing multi-user MIMO (MU-MIMO) processing [85]. Furthermore, network operators can offer a dynamic and scalable capacity in the next cellular generation due to the aggregated channel capacity provided by the MCF technology [86]. Moreover, the possibility of combining MCF-RoF transmissions with additional multiplexing techniques such as time-division multiplexing (TDM), WDM, PDM and mode-division multiplexing (MDM) [12] should be considered.

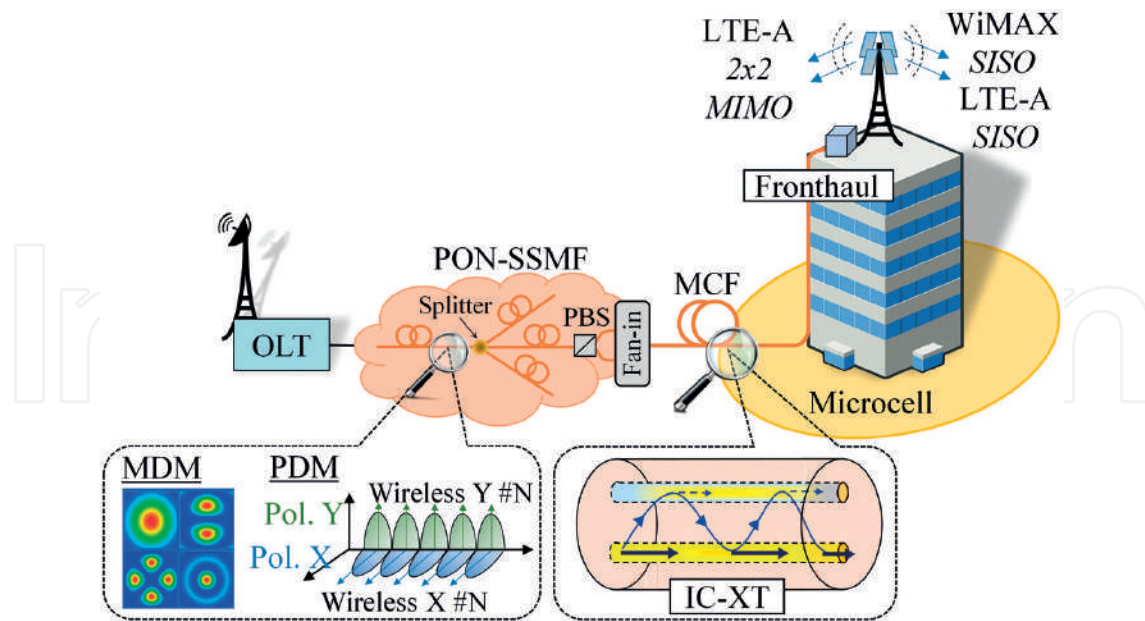


Figure 8. Next-generation optical fronthaul system using MCF medium operating with a converged fiber-wireless PON including optical polarization-division multiplexing (PDM) and mode-division multiplexing (MDM) transmissions.

Figure 8 depicts the proposed fronthaul provision applied to converged fiber-wireless PON including PDM to provide connectivity between the SSMF and MCF media.

Remarkably, the use of MCFs in the next-generation RoF fronthaul systems is proposed for the first time in [52, 87]. In these works, it is investigated the performance of fully standard LTE-A signals in MIMO and SISO configurations with the random IC-XT fluctuations and the demonstration of fronthaul provision of both LTE-A and WiMAX signals using a 150-m SI-SM-HO-UC-LB-4CF. In order to reduce the random fluctuations of the error vector magnitude (EVM) induced by the IC-XT, the core interleaving nonlinear stimulation (CINLS) was proposed to mismatch the phase constant of adjacent core modes reducing the temporal and spectral EVM fluctuations of the MCF-RoF transmissions.

4.2. Signal processing

The potential application of MCFs is not only restricted to SDM transmissions. The inherent capability of a MCF to modify the propagated signals allows us to investigate a vast scenario of new applications for ultra-high capacity SDM transmissions and microwave photonics (MWP) based on signal processing techniques. As we will see, the basic concept of the signal processing using MCFs is a far richer scope than initially foreseen.

In particular, the use of MCFs for MWP applications based on signal processing was firstly proposed by Gasulla and Capmany in [88]. In this work the authors investigate the suitability of these new fibers to perform true-time delay lines (TTDLs), optical beamforming, optical filtering and arbitrary waveform generation using heterogeneous cores. These applications have been extensively researched in [30, 31, 89–93] with different MCF designs and experimental setups. As an attractive example, it should be remarked the proposal reported in [31, 90], where the inscription of selective Bragg gratings in a homogeneous MCF it was introduced in [90] and

experimentally verified in [31] to achieve compact fiber-based TTDL without using heterogeneous cores. Along this line, other MWP applications such as optical beamforming can also be performed by using homogeneous cores as described in [94]. In this work, Llorente and co-workers propose a compact all-fiber beamformer based on a N -core homogeneous MCF.

On the other hand, the MCF signal processing also involves additional applications and functionalities such as pulse shaping, dispersion engineering, modal conversion and modal filtering applications. Remarkably, the engineering of the refractive index profile allows us to implement these fashion features in MCF media. In this scenario, a fascinating proposal recovered from the string and quantum field theory was firstly introduced in [95] within the framework of photonics and further developed in [19, 96] to design SCFs and MCFs: the supersymmetry (SUSY). Specifically, one-dimensional SUSY allows us to perform the aforementioned MWP applications. The specific details can be found in [96] for cylindrical potentials with axial symmetry. As an interesting example (among other applications detailed in this work), we include here the description of a true modal (de)multiplexer (M-MUX/DEMUX) using a 3-core MCF. **Figure 9** shows the optical device and its functionality.

The device is designed using a 60-cm MCF comprising three cores a , b and c with a core-to-core distance $d_{ab} = d_{ac} = 55 \mu\text{m}$, $R_0 = 25 \mu\text{m}$, and $\lambda_0 = 1550 \text{ nm}$ [**Figure 9(a)**]. The index profiles of the cores a and c are calculated by using the Darboux procedure. The index profile of the core b is taken to be the step-index profile, with $n_b = 1.45$ when $r < R_0$. A 10-ps Gaussian optical pulse is launched to the central core b , first in the LP_{01} mode, and later in the LP_{11} and LP_{21} modes with a peak power of 0 dBm. The numerical simulation was performed using a beam propagation method at $\lambda_0 = 1550 \text{ nm}$. **Figure 9(b)** shows the numerical results of the optical pulse propagating through each LP mode in the M-DEMUX. It is worth noting that, in contrast with other mode (de)multiplexing strategies [97–100], a true mode demultiplexing is achieved for each LP mode. At the device output, the pulse launched into the LP_{11} mode of the core b is found in the LP_{11} mode of the core a , the pulse launched into the LP_{01} mode of the core b is found in the same mode and core, and the pulse launched into the LP_{21} mode of the core b can be observed

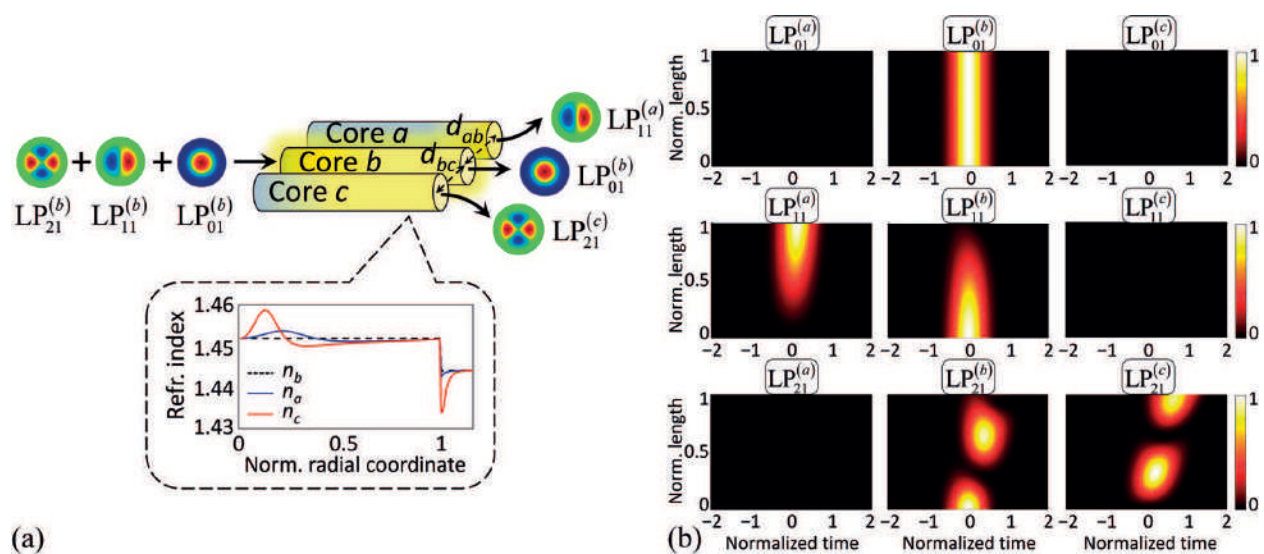


Figure 9. Modal (de)multiplexer based on a 60-cm 3-core MCF [96]. (a) Schematic structure of the optical device. (b) A 10-ps Gaussian pulse propagating through the: LP_{01} , LP_{11} and LP_{21} modes of the cores a , b , and c .

in the LP_{21} mode of the core c . Moreover, pulse shaping and dispersion engineering functionalities can be incorporated in the proposed device as indicated in [96]. On the other hand, it should be noted that the SUSY transformations presented in [96] can also be applied to axially symmetric quantum and acoustic potentials as discussed in this work.

4.3. Multi-core fiber lasers, amplifiers and optical sensors

All-fiber designs of optical lasers, amplifiers and sensors using MCFs have been extensively investigated in recent years [32, 101–111]. In particular, the multi-mode interference (MMI) which can be observed through a chain SMF-MCF-SMF is widely employed in lasers, amplifiers and optical sensors to improve the performance of classical designs based on SCFs [32, 104].

As one can expect, the basic concept of an active MCF is the natural evolution for the cladding pumped rare-earth-doped fibers. The classical design using a single core offers an excellent combination of high efficiency and beam quality. However, high output powers are limited by the stimulation of nonlinear effects. In that case, the increment of the mode field area is the obvious solution to decrease the nonlinear effects. In this scenario, active MCFs offer the possibility of reducing the nonlinear effects using a coupled-core design to generate supermodes with large mode field area [101, 105]. Moreover, note that the gain medium is split at discrete regions (cores) inside the cladding, and therefore, the thermal dissipation is higher than in the classical single-core design. As a result, higher output powers can be achieved in MCF media [105]. On the other hand, in contrast with a SCF bundle, a N -core MCF laser/amplifier only requires a single pumped laser for N optical paths, with the corresponding energy cost reduction for the network operators [5, 106, 107].

In this topic, an intense research work has been developed in the last decade [5, 11, 12]. To date, most CC-MCF lasers/amplifiers operate in the in-phase supermode combining high brightness and near-diffraction limited far field profile. The selection of the in-phase supermode can be performed by using diverse methods such as phase-locking and Talbot cavities [102]. As an example, a monolithic fiber laser using a CC-MCF with highly and lowly reflective fiber Bragg gratings (HR/LR-FBG) is shown in **Figure 10(a)** [104]. The MCF segment is located between the HR-FBG and the LR-FBG creating an active cavity, where the MMI allows us to obtain a high-contrast spectral modulation. In addition, the uniform illumination of the cores is achieved by performing a cladding pumping scheme. Remarkably, this MCF laser design demonstrates the direct correlation between the MMI in few-mode SCF systems and in the laser operation when multiple supermodes oscillate simultaneously. Following a similar approach, additional MCF laser and amplifier designs have been proposed in [103, 105]. Nevertheless, in long-haul SDM transmissions the usual design is the multi-core erbium-doped-fiber-amplifier based on a cladding pumped scheme [106, 107].

On the other hand, MCF sensors are also based on a similar concept as in the laser of the previous example [see **Figure 10(b)**]. The sensor comprises two SSMFs spliced to a short MCF segment with hexagonal shaped cores. The operating principle within the MCF segment is the MMI, which induces a deep peak in the transmission spectrum. An external environmental change shifts the spectral position of the minimum. As an specific example, let us consider a temperature change. When increasing the temperature, the thermal expansion of the MCF medium will increase the refractive index of the silica cores, and consequently, the peak will be shifted to a longer wavelength [32].

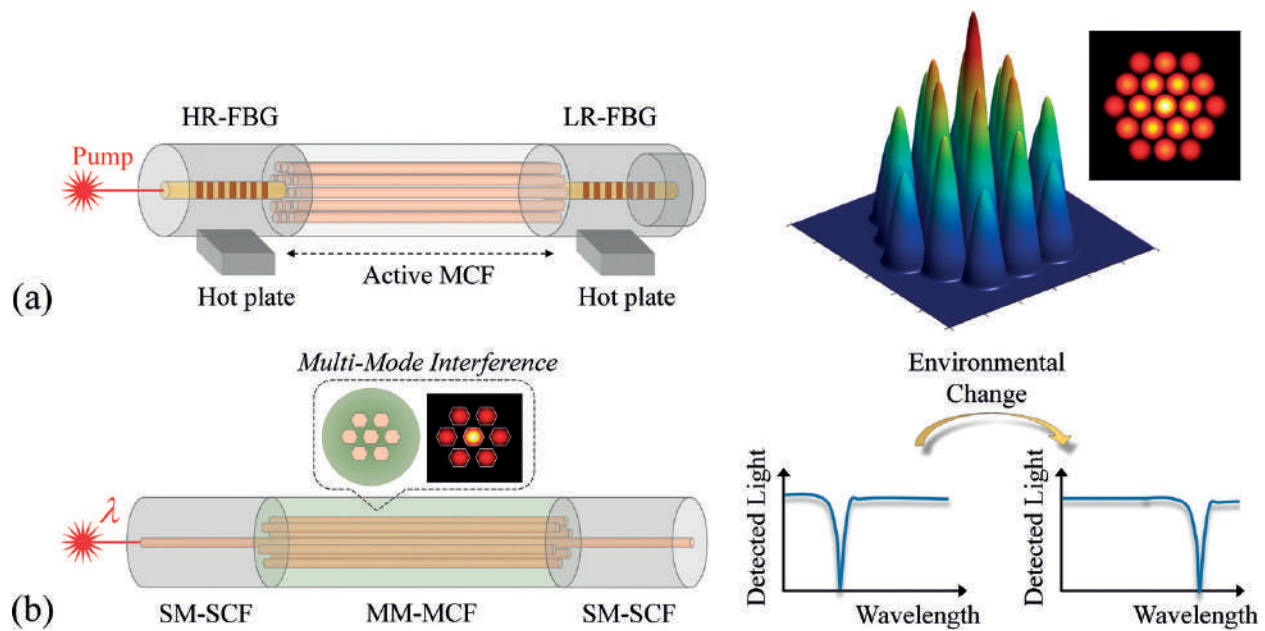


Figure 10. MCF laser and optical sensor operating on the principle of multi-mode interference (MMI). (a) MCF laser comprising a highly and lowly reflective fiber Bragg grating (HR/LR-FBG). (b) MCF optical sensor with hexagonal shaped cores. Results based on [32, 104].

In the past, fiber optic sensors using SCFs have been widely discussed for sensing in a broad range of industrial and scientific applications including temperature, force, liquid level, pressure and acoustic waves, among other. Nowadays, the MCF technology allows us to design and fabricate new optical sensors providing accuracy, high resolution, compactness, stability, reproducibility and reliability [32, 108–111].

4.4. Multi-core fibers for medical applications

Multi-core optical fibers have also been studied in recent years within the context of medicine for biomedical sensing and imaging applications [112–121]. Basically, biomedical sensors using MCFs are based on the MMI technique previously described. Thus, let us now focus our attention on biomedical imaging applications in the next paragraphs.

Nowadays, the main challenge in biomedical imaging is the study of cells in biological tissues. In this scenario, the multiphoton microscopy and adaptive optics become fundamental technologies because of their benefits in cellular resolution, high sensitivity, and high imaging rate [121]. In particular, the two-photon excited fluorescence (TPEF) microscopy requires the use of adaptive optics to increase the imaging depth, in practice limited to 1 mm [122]. Remarkably, the so-called *lensless endoscope* is based on the TPEF microscopy and adaptive optics adding at the same time the use of an optical waveguide [121]. The waveguide should be capable of acquiring a multiphoton image of an object located at its tip. To this end, MCFs have been proposed as a necessary technology for the realization of ultrathin lensless endoscopes [112–121]. **Figure 11** depicts different MCF types proposed for biomedical imaging along with a basic scheme of adaptive optics using a spatial light modulator (SLM).

In general, MCFs used for image transport require a high number of cores (>100) with low IC-XT levels and low intermodal dispersion among cores. Therefore, the preferred design is a SI-SM-HO-CC-LB-MCF, in line with the MCF shown in **Figure 11(a)**. Examples of this MCF type fabricated for medical imaging purposes can be found in [113–115], with $d_{ab} < 20 \mu\text{m}$ and IC-XT levels lower than -20 dB/m . In spite of the fact that the intermodal dispersion can be reduced with a homogeneous design, disordered MCFs based on the transverse Anderson localization have been reported in [22] to improve the image transport quality [see **Figure 11(b)**]. Specifically, the transverse Anderson localization of light allows localized optical-beam-transport through a transversely disordered medium. Interesting, in disordered multi-dielectric media, the resultant image quality can also be understood with the perturbation theory. In general, disordered arranged non-homogeneous cores exhibit a high phase-mismatching between their LP modes. As a result, the IC-XT level between adjacent core modes is found to be of the same order or lower than in a homogeneous and periodically arranged design [**Figure 11(a)**]. In a similar way and from our viewpoint, additional highly density MCF designs could be investigated from the CLMT using HB cores with a random orientation of the principal axes to minimize the IC-XT.

On the other hand, adaptive optics is required in the TPEF microscopy to recover the initial imaging of the biological tissue [**Figure 11(c)**]. The advance on wave front shapers composed by 2-D SLMs and deformable mirrors have spurred the main evolution in ultrathin endoscopes [121]. Thompson et al. were the first to report imaging with a lensless endoscope based on a waveguide with multiple cores [112]. Later, in 2013, Andresen and co-workers realized a lensless endoscope employing a MCF similar to **Figure 11(a)** with extremely low IC-XT between adjacent cores [113]. In the same line, additional works have been reported combining MCF and MM-SCFs with adaptive optics in [114–120]. At present, the major aim in lensless endoscopy using MCF media is to increase the core density with a reduced IC-XT and intermodal dispersion between neighboring cores [121].

4.5. Multi-core fiber opportunities in experimental physics

In the past, fiber-optical analogies have been investigated to use optical fibers as an experimental platform for testing different physical phenomena in various fields, such as in quantum

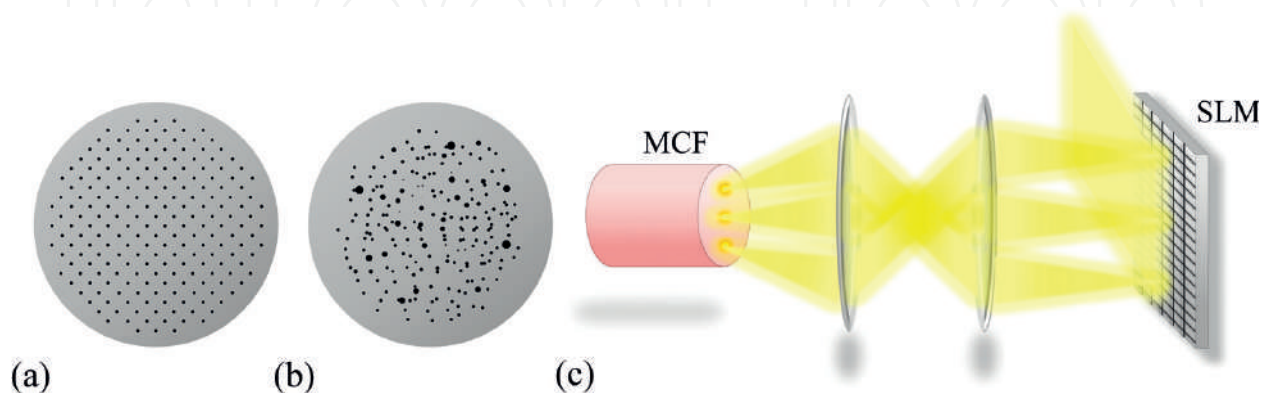


Figure 11. MCFs and adaptive optics for medical imaging. (a) MCF with low IC-XT and periodically arranged cores [113], (b) disorder MCF based on transverse Anderson localization, and (c) wavefront shaping with a single spatial light modulator (SLM) for a MCF based lensless endoscope. Results based on [22, 114].

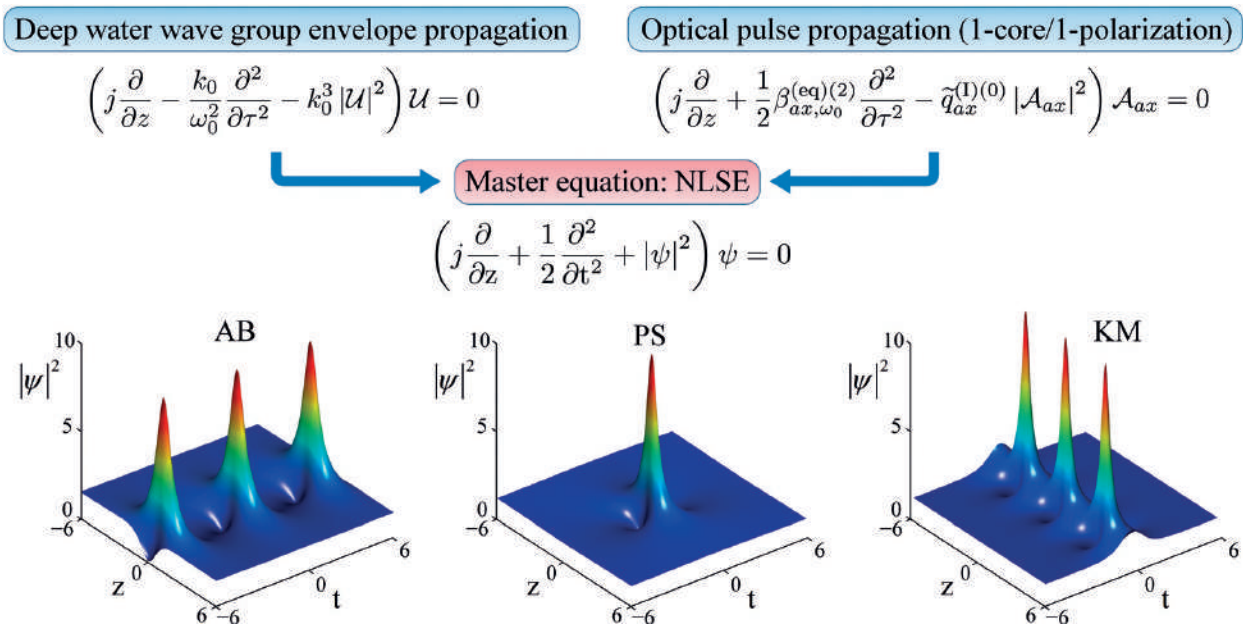


Figure 12. Analogy between fluid mechanics and optics. The NLSE describes the linear and nonlinear wave propagation in different physical systems. Analytical SFB solutions of the NLSE: Akhmediev breathers (ABs), the Peregrine soliton (PS) and the Kuznetsov-Ma (KM) solitons.

mechanics, general relativity or condensed matter physics, among others [16–23]. In fact, a specific example of solid-state physics has already been discussed in the previous subsection, the Anderson effect, relying on the immobility of an electron in a disordered lattice [21, 22]. As Anderson localization involves an interfering phenomenon, this effect has been extended to optics. In [21], Anderson localization has been discussed in two-dimensional photonic lattices, and in [22] it has been discussed its potential applications for medical imaging using disordered MCFs, as pointed out before. More broadly, additional strong disorder phenomena in optics such as the self-organized instability in MM-SCFs [123] can be generalized to MM-MCFs.

Another interesting example can be found in fluid dynamics in the studio of rogue waves on deep water. The giant oceanic rogue waves emerge from the sea induced by many different linear and nonlinear wave propagating effects [124]. Indeed, these nonlinear phenomena can be investigated from a fiber-optical analogy [125]. The nonlinear wave propagation on deep water and in a SM-SCF is described in both cases by a master equation: the nonlinear Schrödinger equation (NLSE), as shown in **Figure 12**.

It can be seen that both propagating equations present a similar form, and therefore, the theoretical results can be directly extrapolated from one field to another. Significantly, the emergence of rogue waves can be analytically studied from the solutions of the NLSE referred to as *solitons on finite background* (SFB) [126]. As a specific example, we include in **Figure 12** the Akhmediev breathers (ABs), the Peregrine soliton (PS) and the Kuznetsov-Ma (KM) solitons²¹. In a similar way, the coupled NLSEs (CNLSEs) have also been discussed in the literature to gain physical

²¹Many of these SFB solutions are termed in the literature as rogue waves. Nevertheless, the fundamental concept of rogue waves emerging unexpectedly from the sea requires additional statistical criteria only fulfilled by higher-order SFB solutions. In either case, the term rogue waves is commonly used for any analytical SFB solution of the NLSE.

insight between interacting rogue waves [127–130]. In this scenario, MCFs offer the possibility of investigating the collision of these nonlinear solutions by using the CLMT [Eq. (14)]. In fact, MCFs can be employed to elucidate the underlying wave propagation phenomena of any physical system with propagating equations of the form of the CNLSEs, for example, superposed nonlinear waves in coherently coupled Bose-Einstein condensates [130] or turbocharge applications in acoustics [131]. Remarkably, in acoustics, the CLMT reported in [60] can play an essential role. Time-varying multi-core cylindrical acoustic ducts can be engineered with the same modal properties as optical MCFs. Therefore, the presented theory can be employed to analyze the intermodal dispersion and the random medium perturbations in acoustic duct conductions.

On the other hand, additional exotic physical phenomena can also be explored in MCF media expanding the possibilities of the classical SCFs. For example, an optical pulse propagating through a SCF establishes a moving medium which corresponds to a space-time geometry. Specifically, this gravitational approach was employed in [20] to demonstrate a fiber-optical analogy of the event horizon in a black hole. Along this line, additional gravitational anomalies could be investigated in a MCF when adjacent cores perturb the space-time geometry created by an optical pulse propagating in a given core of the fiber.

Finally, it is worth mentioning that MCFs are being explored in other branches of experimental physics as in astronomy [132]. The main advantage of these new fibers is the reduced core-to-core distance which can be achieved in a single cladding. In particular, this property has revealed special interest because of the superior fill factor²² to other approaches for creating spectroscopic maps of galaxies or detecting exoplanets. The Sydney-AAO Multi-object Integral field spectrograph (SAMi) project [133], responsible of performing a large spatial spectroscopy of galaxies, pioneered the introduction of MCFs in astronomical observatories.

5. Conclusions and outlook

Multi-core optical fibers have been developed during the last decade, remarkably within the context of SDM transmissions. In this chapter we have reviewed the main MCF types, the fundamental concepts of the linear and nonlinear propagation, and finally, their potential applications in diverse fields of science. In spite of the fact that the fundamentals of the MCF technology have been well elucidated in recent years, the main challenges in this topic involve the following points:

- The analysis of the longitudinal and temporal fluctuations of the crosstalk should be further investigated in the multi-mode regime. To this end, the CLMT of [61] could be extended to MM-MCFs. In addition, other theoretical models based on the Manakov equations [56, 57] can also be employed and extended to the femtosecond regime.
- Existing and additional MCF fabrication methods should be explored and optimized not only in the S + C + L optical bands, but also in the first and second transmission window. In general, the manufacturing cost of a MCF and the peripheral devices (fan-in/fan-out

²²Fill factor: ratio between the cores and the total transversal area of the waveguide. Typically, in MM-SCFs (105/125) the fill factor is of the order of 0.7. Using a MM-SCF or a fiber bundle of SM-SCFs a lot of dead space cannot be observed.

connectors, lasers, amplifiers, photonic lanterns, power combiners, couplers, multiplexers, etc) should be reduced.

- The efforts in future MCF designs must be focused on the increment of the core density minimizing the IC-XT, the intermodal dispersion and the random linear birefringence induced by the microbends. The impact of external perturbations such as the macrobends and the fiber twisting should also be reduced in real-deployed MCF systems. Furthermore, new MCF designs should also be investigated for lensless endoscope integrating a high number of cores with a reduced evanescent field in the cladding. In this scenario, it has been proposed HB-MCFs with a random orientation of the principal axes in each core.
- Fronthaul connectivity performed by MCF-ROF transmissions should be spurred for the next-generation wireless systems, e.g. 5G cellular technology and Beyond-5G. In this line, selective-inscribed FBGs [31] and SUSY MCFs [96] will allow us to process the propagated optical signals between the OLT and the microcell.
- On-line MIMO processing of MDM transmissions using MM-MCFs should be developed to support real-time applications in backbone and access networks [134].
- Quantum communications are emerging as a fundamental key in network security [135]. Nowadays, quantum key distribution (QKD) is making the transition from the laboratory to field trials [136]. In this scenario, the QKD through MCF media should be further investigated for the next-generation optical SDM networks [137].

Acknowledgements

This work was supported by Spanish National Plan projects MINECO/FEDER UE XCORE TEC2015-70858-C2-1-R and HIDRASENSE RTC-2014-2232-3. A. Macho work was supported by BES-2013-062952 F.P.I. Grant.

Author details

Andrés Macho Ortiz* and Roberto Llorente Sáez

*Address all correspondence to: amachor@ntc.upv.es

Nanophotonics Technology Center, Universitat Politècnica de València, Valencia, Spain

References

- [1] Ayhan Y, Cavdar IH. Optimum link distance determination for a constant signal to noise ratio in M-ary PSK modulated coherent optical OFDM systems. *Telecommunication Systems*. 2013;4:461-470

- [2] Yu J, Dong Z, Chien H-C, Jia Z, Li X, Huo D, Gunkel M, Wagner P, Mayer H, Schippel A. Transmission of 200 G PDM-CSRZ-QPSK and PDM-16QAM with a SE of 4 b/s/Hz. *Journal of Lightwave Technology*. 2013;**31**(4):515-522
- [3] Li L, Jijun Z, Degong D, Aihan Y. Analysis modulation formats of DQPSK in WDM-PON system. *Optik*. 2012;**123**:2050-2055
- [4] Essiambre R-J, Kramer G, Winzer PJ, Foschini GJ, Goebel B. Capacity limits of optical fiber networks. *Journal of Lightwave Technology*. 2010;**28**(4):662-701
- [5] Richardson D, Fini J, Nelson LE. Space-division multiplexing in optical fibres. *Nature Photonics*. 2013;**7**:354-362
- [6] Bozinovic N et al. Terabit-scale orbital angular momentum mode division multiplexing in Fibers. *Science*. 2013;**340**(6140):1545-1548
- [7] Van Uden RGH et al. Ultra-high-density spatial division multiplexing with a few-mode multi-core fibre. *Nature Photonics*. 2014;**8**:865-870
- [8] Inao S et al. High density multi-core-fibre cable. In: *The International Cable Connectivity Symposium (IWCS)*. 1979. pp. 370-384
- [9] Inao S, Sato T, Sentsui S, Kuroha T, Nishimura Y. Multi-core optical fiber. In: *The Optical Fiber Communication Conference and Exhibition (OFC)*. Washington: Optical Society of America; 1979. WB1
- [10] Berdagué S, Facq P. Mode-division multiplexing in optical fibers. *Applied Optics*. 1982;**21**(11):1950-1055
- [11] Saitoh K, Matsuo M. Multicore Fiber technology. *Journal of Lightwave Technology*. 2016;**34**(1):55-66
- [12] Mizuno T, Takara H, Sano A, Miyamoto Y. Dense space-division multiplexed transmission systems using multi-core and multi-mode fiber. *Journal of Lightwave Technology*. 2016;**34**(2):582-591
- [13] Temprana E et al. Overcoming Kerr-induced capacity limit in optical fiber transmission. *Science*. 2015;**348**(6242):1445-1447
- [14] Li G, Bai N, Zhao N, Xia C. Space-division multiplexing: The next frontier in optical communication. *Advanced in Optics and Photonics*. 2014;**6**:413-487
- [15] Puttnam BJ et al. Modulation formats for multi-core fiber transmission. *Optics Express*. 2014;**22**(26):32457-32469
- [16] Wan W, Jia S, Fleischer JW. Dispersive superfluid-like shock waves in nonlinear optics. *Nature Physics*. 2007;**3**:46-51
- [17] Fatome J, Finot C, Millot G, Armaroli A, Trillo S. Observation of optical undular bores in multiple four-wave mixing. *Physical Review X*. 2014;**4**:021022

- [18] Dreisow F et al. Classical simulation of relativistic Zitterbewegung in photonic lattices. *Physical Review Letters*. 2010;**105**:143902
- [19] Miri M-A, Heinrich M, Ganainy RE, Christodoulides DN. Supersymmetric optical structures. *Physical Review Letters*. 2013;**110**:233902
- [20] Philbin TG et al. Fiber-optical analog of the event horizon. *Science*. 2008;**319**(5868):1367-1370
- [21] Schwartz T, Bartal G, Fishman S, Segev M. Transport and Anderson localization in disordered two-dimensional photonic lattices. *Nature*. 2007;**446**:52-55
- [22] Karbasi S et al. Image transport through a disordered optical fibre mediated by transverse Anderson localization. *Nature Communications*. 2014;**5**(3362)
- [23] Saleh MF et al. Raman induced temporal condensed matter physics in a gas-filled photonic crystal fibers. *Optics Express*. 2015;**23**(9):11879-11886
- [24] Sumimoto Electric. Sumitomo electric has developed new-type multi-Core optical Fiber for optical interconnects and realized highest-density multi-Core Fiber optic cable [internet]. March 26, 2015. Available from: http://global-sei.com/company/press/2015/03/prs022_s.html
- [25] Xia C, Bai N, Ozdur I, Zhou X, Li G. Supermodes for optical transmissions. *Optics Express*. 2011;**19**(17):16653-16664
- [26] Ryf R et al. Space-division multiplexed transmission over 3×3 coupled-core multicore fiber. In: *Optical Fiber Communication Conference (OFC)*. San Francisco: Optical Society of America; 2014. Tu2J.4
- [27] Hayashi T et al. Coupled-core multi-core fibers: High-spatial-density optical transmission fibers with low differential modal properties. In: *European Conference On Optical Communications (ECOC)*; Valencia. IEEE. 2015
- [28] Stone JM, Yu F, Knight JC. Highly birefringent 98-core fiber. *Optics Letters* 2014; **39**(15): 4568-4570
- [29] Kim Y et al. Adaptive multiphoton Endomicroscope incorporating a polarization-maintaining multicore optical fibre. *IEEE Journal of Selected Topics in Quantum Electronics*. 2016;**22**(3):171-178
- [30] García S, Gasulla I. Dispersion-engineered multicore fibers for distributed radio-frequency signal processing. *Optics Express*. 2016;**24**(18):20641-20654
- [31] Gasulla I, Barrera D, Hervás J, Sales S. Spatial division multiplexed microwave signal processing by selective grating inscription in homogeneous multicore fibers. *Scientific Reports*. 2017;**7**(41727). <https://www.nature.com/articles/srep41727>
- [32] López JEA, Eznaveh ZS, LiKamWa PL, Schülzgen A, Correa RA. Multicore fiber sensor for high-temperature applications up to 1000°C. *Optics Letters*. 2014;**39**(15):4309-4312

- [33] Hayashi T, Taru T, Shimakawa O, Sasaki T, Sasaoka E. Design and fabrication of ultra-low crosstalk and low-loss multi-core fiber. *Optics Express*. 2011;**19**(17):16576-16592
- [34] Zioliowicz A et al. Hole-assisted multicore optical fiber for next generation telecom transmission systems. *Applied Physics Letters*. 2014; **105**(081106)
- [35] Mahdiraji GA, Amir Khan F, Chow DM, Kakaie Z, Yong PS, Dambul KD, Adikan FRM. Multicore flat Fiber: A new fabrication technique. *IEEE Photonics Technology Letters*. 2014;**26**(19):1972-1974
- [36] Ishida I et al. Possibility of stack and draw process as fabrication technology for multi-core fiber. In: *Optical Fiber Communication Conference (OFC)*. Anaheim: Optical Society of America; 2013. OTu2G.1
- [37] Yamamoto J et al. Fabrication of multi-core fiber by using slurry casting method. In: *Optical Fiber Communication Conference (OFC)*. Los Angeles: Optical Society of America; 2017. Th1H.5
- [38] Feuer M et al. Joint digital signal processing receivers for spatial superchannels. *IEEE Photonics Technology Letters*. 2012;**24**(21):1957-1960
- [39] Eriksson TA et al. Single parity check-coded 16QAM over spatial superchannels in multicore fiber transmission. *Optics Express*. 2015;**23**(11):14569-14582
- [40] Rademacher G, Puttnam BJ, Luis RS, Awaji Y, Wada N. Experimental investigation of a 16-dimensional modulation format for long-haul multi-core fiber transmission. In: *European Conference on Optical Communications (ECOC)*. Valencia: IEEE; 2015. P.5.10
- [41] Puttnam BJ, Luis RS, Mendinueta JMD, Awaji Y, Wada N. Linear block-coding across >5 Tb/s PDM-64QAM spatial super-channels in a 19-core fiber. In: *European Conference on Optical Communications (ECOC)*. Valencia: IEEE; 2015. P.5.6
- [42] Marcuse D. *Theory of Dielectric Optical Waveguides*. Elsevier; 1974
- [43] Winzer PJ, Essiambre R-J. Advanced modulation formats for high-capacity optical transport networks. *Journal of Lightwave Technology*. 2006;**24**(12):4711-4728
- [44] Gloge D. Weakly guiding fibers. *Applied Optics*. 1971;**10**(10):2252-2258
- [45] Fini JM, Zhu B, Taunay TF, Yan MF. Statistics of crosstalk in bent multicore fibers. *Optics Express*. 2010;**18**(14):15122-15129
- [46] Koshiha M, Saitoh K, Takenaga K, Matsuo S. Multi-core fiber design and analysis: Coupled-mode theory and coupled-power theory. *Optic Express*. 2011;**19**(26):B102-B111
- [47] Koshiha M, Saitoh K, Takenaga K, Matsuo S. Analytical expression of average power-coupling coefficients for estimating intercore crosstalk in multicore fibers. *IEEE Photonics Journal*. 2012;**4**(5):1987-1995
- [48] Hayashi T, Sasaki T, Sasaoka E, Saitoh K, Koshiha M. Physical interpretation of intercore crosstalk in multicore fiber: Effects of macrobend, structure fluctuation, and microbend. *Optics Express*. 2013;**21**(5):5401-5412

- [49] Macho A, Morant M, Llorente R. Experimental evaluation of nonlinear crosstalk in multi-core fiber. *Optics Express*. 2015;**23**(14):18712-18720
- [50] Macho A, Morant M, Llorente R. Unified model of linear and nonlinear crosstalk in multi-core fiber. *Journal of Lightwave Technology*. 2016;**34**(13):3035-3046
- [51] Ye F, Tu J, Saitoh K, Morioka T. Simple analytical expression for crosstalk estimation in homogeneous trench-assisted multi-core fibers. *Optics Express*. 2014;**22**(19):23007-23018
- [52] Morant M, Macho A, Llorente R. On the suitability of multicore fiber for LTE-advanced MIMO optical fronthaul systems. *Journal of Lightwave Technology*. 2016;**34**(2):676-682
- [53] Macho A, Meca CG, Peláez FJF, Morant M, Llorente R. Birefringence effects in multi-core fiber: Coupled local-mode theory. *Optics Express*. 2016;**24**(19):21415-21434
- [54] Iizuka K. *Elements of photonics volume I*. Wiley; 2002
- [55] Luis RS et al. Time and modulation frequency dependence of crosstalk in homogeneous multi-core fibers. *Journal of Lightwave Technology*. 2016;**34**(2):441-447
- [56] Mecozzi A, Antonelli C, Shtaif M. Nonlinear propagation in multi-mode fiber in the strong coupling regime. *Optics Express*. 2012;**20**(11):11673-11678
- [57] Mumtaz S, Essiambre RJ, Agrawal GP. Nonlinear propagation in multimode and multicore fibers: Generalization of the Manakov equations. *Journal of Lightwave Technology*. 2013;**31**(3):398-406
- [58] Chiang KS. Coupled-mode equations for pulse switching in parallel waveguides. *IEEE Xplore: IEEE Journal of Quantum Electronics*. 1997;**33**(6):950-954
- [59] Liu M, Chiang KS. Effects of intrapulse stimulated Raman scattering on short pulse propagation in a nonlinear two-core fiber. *Applied Physics B*. 2007;**87**:45-52
- [60] Liu M, Chiang KS. Pulse propagation in a decoupled two-core fiber. *Optics Express*. 2010;**18**(20):21261-21268
- [61] Macho A, Meca CG, Peláez FJF, Cortés-Juan F, Llorente R. Ultra-short pulse propagation model for multi-core fibers based on local modes. *Scientific Reports*. 2017;**7**(16457)
- [62] Weiner AM. *Ultrafast optics*. Wiley; 2009
- [63] Agrawal GP. *Nonlinear fiber optics*. Elsevier; 2013
- [64] Zhu B, Taunay T, Yan M, Fini J, Fishteyn M, Monberg EM. Seven-core multi-core fibre transmissions for passive optical network. *Optics Express*. 2010;**18**(11):11117-11122
- [65] Puttnam BJ, Delgado J-M, Sakaguchi J, Luis RS, Klaus W, Awaji Y, Wada N, Kanno A, Kawanishi T. 210Tb/s Self-Homodyne PDM-WDM-SDM Transmission with DFB Lasers in a 19-Core Fibre. In: *European Conference on Optical Communications (ECOC)*. London: IEEE; 2013. TuC1.2
- [66] Sakaguchi J et al. 305 Tb/s space division multiplexed transmission using homogeneous 19-Core fibre. *Journal of Lightwave Technology*. 2013;**31**(4):554-562

- [67] Takara H et al. 1.01-Pb/s (12 SDM/222 WDM/456 Gb/s) crosstalk-managed transmission with 91.4-b/s/Hz aggregate spectral efficiency. In: European Conference on Optical Communications (ECOC). Amsterdam, Netherlands: IEEE; 2012. Th3.C.1
- [68] Chandrasekhar S et al. WDM/SDM transmission of 10 × 128-Gb/s PDM-QPSK over 2688-km 7-core fiber with a per-fiber net aggregate spectral-efficiency distance product of 40,320 km·b/s/Hz. In: European Conference on Optical Communications (ECOC). Geneva, Switzerland: IEEE; 2011. Th13.C.4
- [69] Takeshima K et al. 51.1-Tbit/s MCF transmission over 2520 km using cladding pumped 7-core EDFAs. In: Optical Fiber Communication Conference (OFC). Los Angeles, USA: Optical Society of America; 2015. W3G.1
- [70] Sakaguchi J et al. Realizing a 36-core, 3-mode Fibre with 108 Spatial Channels. In: Optical Fiber Communication Conference (OFC). Los Angeles, USA: Optical Society of America; 2015. Th5C.2
- [71] Shibahara K, et al. Dense SDM (12-core × 3-mode) Transmission over 527 km with 33.2 ns Mode-Dispersion Employing Low-Complexity Parallel MIMO Frequency-Domain Equalization. In: Optical Fiber Communication Conference (OFC). Los Angeles, USA: Optical Society of America; 2015. Th5C.3
- [72] Igarashi K, et al. 114 Space-Division-Multiplexed Transmission over 9.8-km Weakly-Coupled-6-Mode Uncoupled-19-Core Fibers. In: Optical Fiber Communication Conference (OFC). Los Angeles, USA: Optical Society of America; 2015. Th5C.4
- [73] Igarashi K et al. Ultra-dense spatial-division-multiplexed optical fiber transmission over 6-mode 19-core fibers. *Optics Express*. 2016;**24**(10):10213-10231
- [74] Kobayashi T et al. 1-Pb/s (32 SDM/46 WDM/768 Gb/s) C-band dense SDM transmission over 205.6-km of single-mode heterogeneous multi-core fiber using 96-Gbaud PDM-16QAM channels. In: Optical Fiber Communication Conference (OFC). Los Angeles, USA: Optical Society of America; 2017. Th5B.1
- [75] Tanaka K, Agata A. Next-generation Optical Access Networks for C-RAN. In: Optical Fiber Communication Conference (OFC). Los Angeles, USA: Optical Society of America; 2015. Tu2E.1
- [76] Cvijetic N. Optical network evolution for 5G mobile applications and SDN-based control. In: Proceedings of 16th International Telecomm. Network Strategy and Planning Symposium. IEEE; 2014
- [77] Öhlen P et al. Flexibility in 5G Transport Network: The Key to Meeting the Demand for Connectivity [Internet]. 2015. Available from: <https://www.ericsson.com/>
- [78] Rappaport TS. Millimeter wave wireless communications for 5G cellular: It will work! In: Personal, indoor, and mobile radio communications conference. Washington, USA: IEEE. 2014
- [79] Ericsson. 5G Energy Performance [Internet]. 2015. Available from: <http://www.5gamericas.org/files>

- [80] Kohn U. Fronthaul Networks—a Key Enabler for LTE-Advanced [Internet]. 2014. Available from: <https://oristel.com.sg/wp-content/uploads/2015/03/Fronthaul-Networks-A-Key-Enabler-for-LTE-Advanced.pdf>
- [81] Zhu M, Liu X, Chand N, Effenberger F, Chang G-K. High-capacity mobile fronthaul supporting LTE-Advanced carrier aggregation and 8×8 MIMO. In: Optical Fiber Communication Conference (OFC). Optical Society of America; 2015. M2J.3
- [82] Cheng L, Liu X, Chand N, Effenberger F, Chang G-K. Experimental demonstration of sub-Nyquist sampling for bandwidth- and hardware-efficient mobile fronthaul supporting 128×128 MIMO with 100-MHz OFDM signals. In: Optical Fiber Communication Conference (OFC). Anaheim, USA: Optical Society of America; 2016. W3C.3
- [83] Wang N, Hossain E, Bhargava VK. Backhauling 5G small cells: A radio resource management perspective. *IEEE Wireless Communications*. 2015;**22**(5):41-49
- [84] Morant, M., Macho, A., and Llorente, R. Optical fronthaul of LTE-Advanced MIMO by spatial multiplexing in multicore fiber. In: Optical Fiber Communication Conference (OFC). Optical Society of America; 2015. W1F.6
- [85] Karadimitrakakis A, Moustakas AL, Vivo P. Outage capacity for the optical MIMO channel, *IEEE transactions on information theory*. *IEEE Transactions on Information Theory*. 2014;**60**(7):4370-4382
- [86] Sano A, Takara H, Moyamoto Y. Large capacity transmission systems using multi-core fibers. In: OptoElectronics and communication Conf. Melbourne, Australia: IEEE. 2014
- [87] Macho A, Morant M, Llorente R. Next-generation optical fronthaul systems using multicore fiber media. *Journal of Lightwave Technology*. 2016;**34**(20):4819-4827
- [88] Gasulla I, Capmany J. Microwave photonics applications of multicore Fibers. *IEEE Photonics Journal*. 2012;**4**(3):877-888
- [89] Yu S, Jiang T, Li J, Zhang R, Wu G, Gu W. Linearized frequency doubling for microwave photonics links using integrated parallel Mach-Zehnder modulator. *IEEE Photonics Journal*. 2013;**5**(4):5501108
- [90] Gasulla I, Barrera D, Sales S. Microwave photonic devices based on multicore fibers. In: Transparent Optical Networks (ICTON). Graz, Austria: IEEE; 2014. Th.B6.4
- [91] Garcia S, Gasulla I. Design of heterogeneous multicore fibers as sampled true-time delay lines. *Optics Letters*. 2015;**40**(4):621-624
- [92] Lawrence RC. Silicon Photonics for Microwave Photonics Applications. In: Optical Fiber Communication Conference (OFC). Anaheim, USA: Optical Society of America; 2016. M2B.4
- [93] Wang J et al. Subwavelength grating enabled on-chip ultra-compact optical true time delay line. *Scientific Reports*. 2016;**6**:30235
- [94] Zainullin A, Vidal B, Macho A, Llorente R. Multicore Fiber Beamforming Network for Broadband Satellite Communications. In: Proceedings of SPIE Terahertz, RF, Millimeter,

- and Submillimeter-Wave Technology and Applications X. San Francisco, USA: SPIE; 2017. 1010310
- [95] Chumakov SM, Wolf KB. Supersymmetry in Helmholtz optics. *Physics Letters A*. 1994;**193**:51-53
- [96] Macho A, Llorente R, Meca CG. Supersymmetric transformations in optical fibers. *Forthcoming*
- [97] Song KY, Hwang IK, Yun SH, Kim BY. High performance fused-type mode-selective coupler using elliptical core two-mode fiber at 1550 nm. *IEEE Xplore: IEEE Photonics Technology*. 2002;**14**(4):501-503
- [98] Hanzawa N. Mode multi/demultiplexing with parallel waveguide for mode division multiplexed transmission. *Optics Express*. 2014;**22**(24):29321-29330
- [99] Chang SH et al. Mode- and wavelength-division multiplexed transmission using all-fiber mode multiplexer based on mode selective couplers. *Optics Express*. 2015;**23**(6):7164-7172
- [100] Corral JL, Rodríguez DG, Llorente R. Mode-selective couplers for two-mode transmission at 850 nm in standard SMF. *IEEE Photonics Technology Letters*. 2016;**28**(4):425-428
- [101] Michaille L, Bennet CR, Taylor DM, Shepherd TJ. Multicore photonic crystal Fiber lasers for high power/energy applications. *IEEE journal of selected topics in Quantum Electronics*. 2009;**15**(2):328-336
- [102] Anderson J, Jollivet C, Van Newkirk A, Schuster K, Grimm S, Schülzgen A. Multi-Core Fiber Lasers. In: *Frontiers in Optics/Laser Science*. Los Angeles, USA: Optical Society of America; 2015. LTu2H.2
- [103] Chuncan W, Fan Z, Chu L, Shuiseng J. Microstructured optical fiber for in-phase mode selection in multicore fiber lasers. *Optics Express*. 2008;**16**(8):5505-5515
- [104] Jollivet C et al. Mode-resolved gain analysis and lasing in multisupermode multi-core fiber laser. *Optics Express*. 2014;**22**(24):30377-30386
- [105] Li L, Schülzgen A, Chen S, Témyanko VI. Phase locking and in-phase supermode selection in monolithic multicore fiber lasers. *Optics Letters*. 2006;**31**(17):2577-2579
- [106] Krummrich PM, Akhtari S. Selection of energy optimized pump concepts for multi-core and multi-mode erbium doped fiber amplifiers. *Optics Express*. 2014;**22**(24):30267-30280
- [107] Abedin KS et al. Multicore erbium doped Fiber amplifiers for space division multiplexing systems. *Journal of Lightwave Technology*. 2014;**32**(16):2800-2808
- [108] Mizuno Y, Hayashi N, Tanaka H, Wada Y, Nahamura K. Brillouin scattering in multicore optical fibers for sensing applications. *Scientific Reports*. 2015;**5**:11388
- [109] Newkirk AV, López JEA, Delgado GS, Piracha MU, Correa RA, Schülzgen A. Multicore Fiber sensors for simultaneous measurement of force and temperature. *IEEE Photonics Technology Letters*. 2015;**27**(14):1523-1526

- [110] Newkirk AV, Eznaveh ZS, López J.EA, Delgado GS, Schülzgen A, Correa RA High Temperature Sensor based on Supermode Interference in Multicore Fiber. In: Conference on Lasers and Electro-Optics (CLEO). San Jose, USA: IEEE/OSA; 2014. SM2N.7
- [111] Villatoro J, Arrizabalaga O, López JEA, Zubia J, de Ocáriz IS, Multicore Fiber Sensors. In: Optical Fiber Communication Conference (OFC). Los Angeles, USA: Optical Society of America; 2017. Th3H.1
- [112] Thompson AJ et al. Adaptive phase compensation for ultracompact laser scanning endomicroscopy. *Optics Letters*. 2011;**36**(9):1707-1709
- [113] Andresen ER et al. Toward endoscopes with no distal optics: Videorate scanning microscopy through a fiber bundle. *Optics Letters*. 2013;**38**(5):609-611
- [114] Andresen ER et al. Two-photon lensless endoscope. *Optics Express*. 2013;**21**(18):20713-20721
- [115] Andresen ER et al. Measurement and compensation of residual group delay in a multicore fiber for lensless endoscopy. *Journal of the Optical Society of America B: Optical Physics*. 2015;**32**(6):1221-1228
- [116] Roper JC et al. Minimizing group index variations in a multicore endoscope fiber. *IEEE Photonics Technology Letters*. 2015;**27**(22):2359-2362
- [117] Kim Y et al. Adaptive multiphoton endomicroscope incorporating a polarization-maintaining multicore optical fibre. *IEEE Journal of Selected Topics in Quantum Electronics*. 2015;**22**(3):6800708
- [118] Sivankutty S et al. Extended field-of-view in a lensless endoscope using an aperiodic multicore fiber. *Optics Letters*. 2016;**41**(15):3531-3534
- [119] Conkey DB et al. Lensless two-photon imaging through a multicore fiber with coherence-gated digital phase conjugation. *Journal of Biomedical Optics*. 2016;**21**(4):045002
- [120] Stasio N, Moser C, Psaltis D. Calibration-free imaging through a multicore fiber using speckle scanning microscopy. *Optics Letters*. 2016;**41**(13):3078-3081
- [121] Andresen ER et al. Ultrathin endoscopes based on multicore fibers and adaptive optics: A status review and perspectives. *Journal of Biomedical Optics*. 2016;**21**(12):121506
- [122] Helmchen F, Denk F. Deep tissue two-photon microscopy. *Nature Methods*. 2005;**2**(12):932-940
- [123] Wright LG, Liu Z, Nolan DA, Li M-J, Christodoulides DN, Wise FW. Self-organized instability in graded-index multimode fibres. *Nature Photonics*. 2016;**10**:771-776
- [124] Kharif C, Pelinovsky E. Physical mechanisms of the rogue wave phenomenon. *European Journal of Mechanics*. 2003;**22**:603-634
- [125] Dudley JM, Dias F, Erkintalo M, Genty G. Instabilities, breathers and rogue waves in optics. *Nature Photonics*. 2014;**8**:755-764

- [126] Akhmediev N, Korneeve VI. Modulation instability and periodic solutions of the nonlinear Schrödinger equation. *Theoretical and Mathematical Physics*. 1986;**69**:1089-1093
- [127] Wu CF, Grimshaw RH, Chow KW, Chan HNA. Coupled "AB" system: Rogue waves and modulation instabilities. *Chaos*. 2015;**25**:103113
- [128] Zhong W-P, Belić M, Malomed BA. Rogue waves in a two-component Manakov system with variable coefficients and an external potential. *Physical Review E*. 2015;**92**:053201
- [129] Manikandan K, Senthilvelan M, Kraenkel RA. On the characterization of vector rogue waves in two-dimensional two coupled nonlinear Schrödinger equations with distributed coefficients. *The European Physical Journal B*. 2016;**89**:218
- [130] Mareeswaran RB, Kanna T. Superposed nonlinear waves in coherently coupled Bose–Einstein condensates. *Physics Letters A*. 2016;**380**:3244-3252
- [131] Rämmal H, Lavrentjev J. Sound reflection at an open end of a circular duct exhausting hot gas. *Noise control Engineering Journal*. 2008;**56**(2):107-114
- [132] Jovanovic N, Guyon O, Kawahara H, Kotani T. Application of Multicore Optical Fibers in Astronomy. In: *Optical Fiber Communication Conference (OFC)*. Los Angeles, USA: Optical Society of America; 2017. W3H.3
- [133] Croom S et al. The Sydney-AAO multi-object integral field spectrograph. *MNRAS*. 2012;**421**:872C
- [134] Randel, S. et al. First Real-Time Coherent MIMO-DSP for Six Coupled Mode Transmission. In: *IEEE Photonics Conference (IPC)*. Virginia, USA: IEEE; 2015. 15600579
- [135] Scarani V, Bechmann-Pasquinucci H, Cerf NJ, Dušek M, Lütkenhaus N, Peev M. The security of practical quantum key distribution. *Reviews of Modern Physics*. 2009;**81**(3): 1301-1350
- [136] Peev M et al. The SECOQC quantum key distribution network in Vienna. *New Journal of Physics*. 2009;**11**(7):075001
- [137] Dynes JF et al. Quantum key distribution over multicore fiber. *Optics Express*. 2016;**24**(8): 8081-8087

Fabrication of Polymer Optical Fiber Splitter Using Lapping Technique

Latifah S. Supian, Mohd Syuhaimi Ab-Rahman,
Norhana Arsad, Chew Sue Ping, Nani Fadzlina Naim,
Nurdiani Zamhari and
Syed Mohd Fairuz Syed Mohd Dardin

Additional information is available at the end of the chapter

<http://dx.doi.org/10.5772/intechopen.71868>

Abstract

This work involves in designing and developing a POF-based directional coupler/splitter using lapping technique and geometrical blocks. Two fiber strands were first tapered at the middle and they were attached to the geometrical blocks and lapped together. Design parameters that are used to develop this coupler/splitter are core diameter, D_c , etching length, L_e , bending radius, R_e , coupling length, L_c and pressure, F_c . All the parameters were taken into account during characterization and analysis of the designed coupler in order to find the most optimum prototype coupler/splitter. Characterizations are done by experimental set-up to test the efficiency, splitting ratio, coupling ratio, excess loss and insertion loss for all the couplers/splitters. Through the characterization process and analysis, the optimized coupler with high splitting ratio and low excess loss were identified. Throughout the experimental process, some of the fibers were improved and renewed in order to realize the design and development of the coupler using this technique. The device can also be utilized as an optical tap and the applications of the device are not only limited in in-house network but also in automotive applications. By using a platform, several splitting ratio can be obtained by integrating different core-cladding thickness and bending radius in order to get the desired splitting ratio and excess loss.

Keywords: polymer optical fiber, splitter, low-cost, lapping technique, green technology, short-haul communication system, geometrical blocks

1. Introduction

1.1. POFs for main medium in short-distance transmission

Polymer optical fibers (POFs) have many advantages compared to other communication medium such as glass fibers, copper cables and wireless communication system. Although glass fibers show high performance in terms of speed, higher bandwidth and minimal loss, POFs in the other hand, offer easy and cost-efficient processing and flexibility, whilst glass optical fibers are very brittle, expensive and the cost of installing overall system is very expensive [1]. Therefore due to the complication of installation using glass optical fibers, where the fibers is easily broken and very sensitive, POFs are more handy and easy to install.

For short-haul distance application, POFs show lower attenuation and data transmission works perfectly within distance less than 1 km. Thus, POFs are more suitable as for medium transmission for home-networking, optical data buses for automotive applications or industrial automation sector. Transmission method of using POFs have emerged as a highly-potential candidate for cost-effective and future-proof solution [2]. Glass optical fibers have replaced copper for telephone networks and backbone wiring for buildings, however, still unable to be used in short distance applications due to its cost.

Polymer optical fibers are widely known around 1960s after glass optical fiber was introduced as an effective transmission medium for optical communication. Over the decades, the performance of POFs have shown improvement in terms of transmission capability from having large attenuation as large as 300–20 dB/km and 3 dB/km for passive device such as optical splitter at visible wavelength [3]. Characteristics that give advantages for POFs include low insertion loss, low production cost, having thermal and mechanical stability and highly potential for mass production reliability. Although the loss of POFs is generally higher than silica or glass fiber, POFs are mostly used in intra office communication system where the distance requirement is only up to a few hundred meters where the losses are low and cost-effective. It provides cost-effective solutions to short distance applications such as local area networks (LAN) and high speed internet access and in vehicles [4].

Multimode POFs particularly is chosen as the fiber technology that is largely employed in short-distance communication applications such as in LANs and interconnects. It is also driven by the needs of higher bit rates and lower cost as cost is one of the important drives in short distance communications.

1.2. DIY kit

Although for short-haul communication system, POFs show lower attenuation and cost-effective compared to glass optical fibers, however, there are lack of industry attention received due to less of industry marketing and education of the end user on how to utilize POFs in the system. The lack of information for the end-users on how to install POF-based devices and components lead to the limitation of POF utilization among the customers or end-users. Although huge companies of automobile and medical equipment companies have already

utilizes POFs, however, the lack of education of the end-users on the technique to install and implement the POFs in home-networking causes the industry to pay less attention on building POFs “do-it-yourself” components and devices [5, 6].

1.3. Green technology

About 3% of the world-wide energy is consumed by the information and communications technology (ICT) which contributes to the carbon dioxide (CO₂) emissions [7]. Telecommunication applications can have a direct impact on lowering greenhouse gas emissions and power consumption. Technical approaches of achieving green communication includes energy-efficient network architecture and protocol and energy-efficient wireless transmission techniques [7]. A green technology coupler/splitter is presented based on polymer optical fiber. The splitter has been fabricated by using harmless chemical solvent to etch the fiber and by using various radii of geometrical blocks as the platforms that are made of acrylic and aluminum.

Wavelength from eco-friendly light emitting diode (LED) is utilized to transmit signal. The red LED (650 nm) is capable to download and upload data through Ethernet cable or video signal. LED source used in the system is a solar powered product of semiconductor diode. Compared to incandescent light, light produced by LED is a cool light. The lifetime of LED surpass incandescent which has at most 50,000 hours. Compared to laser, LED is much safer source and little effort is needed to maintain and conduct the source.

The technique used to fabricate this device includes etching using harmless chemical solvent, acetone and also side-polishing. Both the techniques used are environmentally safe and easy to conduct. Acetone is a safe chemical solvent where studies suggest that acetone has low acute and low toxicity if being ingested or inhaled. It is not regarded as carcinogen, a mutagenic chemical or cause chronic neurotoxicity effects. It is mostly used in cosmetic products, processed food and other household products. Acetone has been rated as “generally recognized as safe” (GRAS) substance [8].

1.4. POF couplers

Polymer optical fiber coupler or splitter is a passive device that is built to perform functions required by optical communications such as isolator, circulator and attenuator [9]. Coupler or splitter is important device in the development of optical networks such as in transportations, local area network and for short-distance or in-house applications, in industrial automation or for sensor applications.

Optical couplers are used to combine two or more optical signal inputs from different paths into one output while splitters act oppositely. A particular message encoded as optical signal that needs to be delivered to several outputs at the same time can utilize $1 \times N$ splitter so that the optical signal can be sent to different routes of optical fibers connected to intended end-users or destinations [10]. The requirements for POF couplers are having small excess loss and insertion loss, various power splitting ratios, easy to develop, can be mass produced and having low cost.

Common types of optical splitter are directional, distributive and wavelength-dependent. The mechanism involves can be characterized as diffusion type, area-splitting type and beam-splitting type. Evanescent wave coupling or radiative coupling is part of diffusion couplers. In evanescent wave coupling, two or more fibers are placed sufficiently closed to one another [11]. It is crucial to place the fibers in parallel over a finite distance known as coupling length so that the evanescent field from the primary fiber builds up a propagation field in the secondary fiber to provide two outputs.

A traditional silica optical coupler in one work is formed by placing the two polished-cladding fibers closely together making the light couple from the direct branch to the coupling branch by evanescent field as shown in **Figure 1**. By changing the polishing depth or tapering depth, the contact area and angle, certain modes can be selected and bandwidth can be enhanced in network systems [12]. When the light is transmitted to the coupler, some light will leak out to the branch and be transmitted as stable transmission mode due to the changed of waveguide structure by polishing. Some of the modes were selected by changing the angle of the contact areas of both fiber [12].

1.5. Existing technique of POF splitters/couplers

One of the advantages of polymer optical fibers as compared to other cable types is the simple connector fittings. Copper cables for high data transfer rates mostly require the connection of twisted pairs that must be individually shielded. At frequencies of several 100 MHz, however, cutting open the shielding over a distance of 1 cm results in a noticeable drop in quality of the connection. Glass fibers in the other hand, have a core diameter between 10 and 200 μm . Precise guides are required and glass fibers cannot simply be cut. The face must either be precisely cut by craving with diamond blade or the face must be polished after the cutting. Other advantages for POF is due to its material where the surface of plastics can be smoothed by both cutting and simple polishing and thermal smoothing of the surface is also possible for PMMA.

One of the existing couplers that have been fabricated is done by [7] where the team had demonstrated for the first time that the POF devices can be fabricated by hand using fused

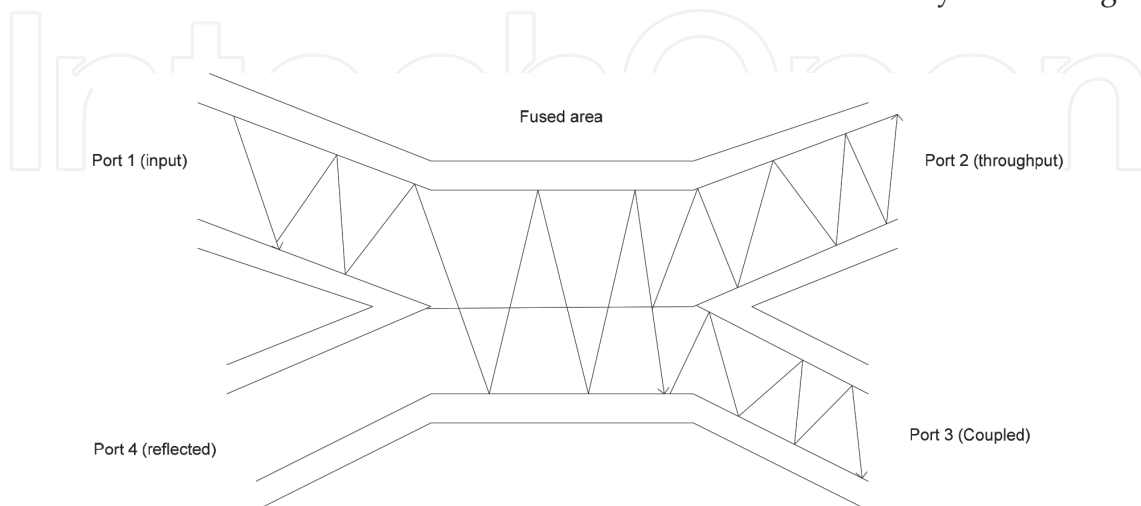


Figure 1. Lapping fibers.

technique. The temperature, stress and splitting technique are the most important parameters to fabricate low loss device. With some modification the device can be used for the extended function such as demultiplexer which is fabricated from uniformity optical splitter [7].

Other techniques include cutting and gluing where in this technique, POF is cut at certain angle using hot knife and glue is applied to attach the two segments of POF. Thermal deformation is a technique where two POF ends are shaped into semicircular form by thermoplastic deformation using hot plate flattening technique. Molding in the other hand is a technique where POF is assembled by a polymer waveguide. Lithography method is used to fabricate the mold [3].

1.6. Etching technique

There are several ways of technique to develop a coupler/splitter. In some cases, tapering is done unto the fibers in the process of developing the coupler. One of the tapering techniques is using chemical etching [4, 5]. Tapering offers unique optical properties that have application to couplers and sensors. The change of diameter can redistribute the modes within the core or remove selected modes. The penetration depth of the evanescent field and proportion of power within this field increases in the tapered section. The change in diameter is used for coupling fibers or interface fibers to devices [13]. This technique has been used by [13] where the cladding of the fiber is thinned using hydrofluoric acid where cladding layer of four micron thick is removed. A technique for removing the cladding of polymethylmethacrylate (PMMA) polymer optical fiber using chemical solvent is used to create etched tapers of a certain length in the middle part of the fiber [14]. PMMA POF is a thermoplastic with softening temperature of 75–80°C. Heat drawing sometimes done unto POF for tapering, however, polymer is not so compatible with drawing due to the latent stress within the structure from production and different physical properties of core and cladding [13]. Thus, etching is by far one of the best methods. The process is simple, low cost and requires no sophisticated equipment and is a safe process since it involves a harmless chemical solvent which is acetone.

PMMA is dissolved using organic solvents such as acetone and methyl isobutyl ketone (MIBK) in order to remove the polymer in concentric layers as required. The method requires no tension to be applied on fiber under etching process so as to prevent brittle stress fracture from occurring and break the fiber. Isopropyl alcohol is used to neutralize the solvent and leave the exposed core clean and grease-free. Once the region has been washed, it will return to PMMA physical and chemical properties.

By tapering the multimode optical fiber cladding, higher modes of the fiber are removed while some other modes are redistributed. As the tapered section is developed, the evanescent field and proportion of total power within this field increases in the affected region. This technique is conventionally applied to glass fibers, however, POF has becoming widely used in optical communication systems and this method can be as a potential towards fabricating a practical coupler using this technique.

The etching process of POF gives an optically smooth surface of similar quality to the original POF due to the polymer quality of POF. If the tapered region is cleanse and washed appropriately the core material section will remain its original properties of PMMA.

1.7. Polishing technique

Side-polishing is one of tapering technique that can be done unto fibers other than etching and fusing. It has been used by other researchers [12, 15, 16] in order to develop couplers/splitter. In this process, single strand multimode fiber is polished at the outer cladding layer for several micrometers. Then the polished fiber is lapped to the other fiber in a bent surface and aided by a thin film of UV curing adhesive is used between them as mode stripping. When the launched port is injected with light source, the mode coupling will occur between the lapped region and split the light accordingly. The strength of the evanescent light coupling is tuned in the range of 0–50% by translating the fibers in or out of alignment of each other [17]. The insertion loss of using this technique is below 5 dB. Polishing technique is considered as one of the simple method to fabricate a directional coupler over the years.

1.8. Macro-bending loss by radiation

Attenuation is a loss of optical power as light travels along the fiber as a result of loss mechanisms such as absorption, scattering and bending. One of the important concepts applied in this research is loss due to macro-bending. Macro-bends are bending that has relatively large radius of curvature compared to the fiber diameter. The loss is high when the bending is smaller. Any dielectric waveguide will radiate if it is bent [18]. Radiation loss occurs in the cladding even when the propagating ray is greater than critical angle. If radius of bending is smaller and wavelength of transmitted light is longer, the macrobending loss or power loss is due to the radiation [19]. Below a critical radius optical fiber bending, macrobending loss is significant. When light facing total internal reflection an electromagnetic disturbance which is known as evanescent wave penetrate the reflecting interface. The amplitudes of evanescent wave decay exponentially when it gets further than the reflecting interface because it cannot propagate in medium of lower refractive index. Non-uniformity in the reflecting interface may cause the evanescent wave to convert into propagating wave. In bending loss, evanescent fields extend to the cladding but decay exponentially with radial distance.

All rays in bent fiber are leaky where at some reflections they lose power by either refraction or tunneling. By stripping the cladding layers, bent fiber will escape from the fiber and the cladding will behave as if it were infinite. The power losses in bent step-index multimode fibers can depend on the cladding thickness. Decreasing the bend radius and increasing fiber core will increase the bending losses. As bend radius begins to decrease, more refracting rays are produced and more power is transferred to the cladding.

Low losses can be obtained in bends that have small radii of the where width of the channel is decreased and the refractive index contrast is increased. Bend losses of multimode channels are independent of wavelength. At some point from the center of the bend, the portion of the field in the cladding would have to exceed the speed of light and be radiated, thus reduce the power in the guided mode [20].

In this research, light that escapes from the bending is utilize to develop an optical coupler or splitter by varying the bending radius in order to obtain certain splitting ratio using mechanical platform of circular blocks and elliptical blocks [21].

1.9. New approach of using lapping technique

Directional coupler is a passive device where power exchanges between two waveguides that is placed in proximity to each other. When a certain power is launched into a waveguide, some of the power is transferred to an adjacent guide due to coupling. The power exchange depends on the interaction length and coupling strength along with other parameters. When two guides are parallel to each other, coupling coefficient is constant and the power launched into one guide will alternate back and forth between the two guides as long as they are close [22].

Complete power transfer occurs when phase velocities are perfectly synchronized and the interaction length is half the coupling length [16]. In [16], they developed a coupler with variable spacing where by gradually increasing the separation between the two guides where all or some of desired power may be transferred from one guide to the other in strong interaction region. By controlling the separation between the channels, the coupler can be realized as switch, splitter and power divider [23].

This research focuses on developing user-friendly and inexpensive splitters with various splitting ratio and low excess loss using POF splitter kit consists of circular blocks and elliptical blocks of varied radii and several pairs of splitters. This technique of splitter development has the advantage of low-cost installation, environmental-friendly with considerable low losses. The proposed fabrication of the coupler/splitter consists of two parallel fibers in contact with each other along a certain coupling length or know as lapping technique [24].

The technique used in this experiment is lapping technique where two similar length fibers are tapered in the middle region using harmless chemical solvent for particular time and the tapered regions of certain diameter, D_c and etched length, L_e are lapped to each other. The taper introduces variations in the effective refractive index of a waveguide and a change in coupling coefficient [16]. Chemical solvent, acetone is used to taper the fiber and stripped off the cladding layer. The thickness of cladding layer that is being stripped off depends on the duration of the etching process. The time duration for etching process in this research range from 30 to 120 minutes. The longer the duration process, the smaller the fiber cores obtained. At this diameter, the cladding layers have been fully etched and leave only the bare core. The aim of this process is to strip off the cladding layers so that when the bare cores are lapped to each other and bent, the rays that propagate in the first fiber can transfer to the second fiber. However, for some fibers the etching process strips off the whole cladding layer including the region that will not be lapped to the other fiber core, this situation will lead the unnecessary losses during splitting/coupling. Thus, the geometrical blocks that the fibers are attached to are customized using acrylic material that has similar refractive index so that it replaces the cladding layers that has been etched.

To stimulate the energy transfers between the primary fiber that has been injected with light source to the secondary fiber, macro-bending effect is a parameter used where the fibers are bent accordingly to the customized geometrical blocks of several bending radii, R_c . It is known that when an optical fiber is bent it radiates power to the surrounding medium. The radiation power in the fiber depends on radius of curvature and the difference between refractive indices of core and cladding. The size of bending radius of the blocks either circular or elliptical

gives the coupling length, L_c , of the contact region of the lapping cores. Coupling length is important in order to obtain high splitting ratio and coupling efficiency.

Two forces, F_c are exerted upon blocks that hold the lapped splitter together, i.e., normal force and given force. The aim is to characterize the splitter when the fiber cores touches each other without external force and recorded as normal force and with external force or namely given force. Force is exerted upon the blocks and fibers in order to minimize the gap that exists between the two lapped fibers in order to observe and characterize the energy transfer of the splitter when different bending radii are formed along with particular core-cladding thickness at certain coupling length. The force exerted upon the fiber also has small impact on the coupling length between the two fibers.

The pair of fibers will be attached to different circular and ellipse-shaped blocks that consist of different bending radii, R_c . The tapering and bending contributes to the effective index of higher-order modes that approach cladding and when the tapering section is constant, the modes become cut-off and radiate which contributes to the loss.

The aim of varying the bending radii, R_c is to characterize and analyze the macro-bending effect on the splitter having varied diameter, D_c , varied etching length, L_e , coupling length, L_c with different load force, F_c . The aim of the design is to obtain optimum bending radius that gives the optimum splitting ratio and low excess loss.

Analytical work is considered where the parameters of core thickness, D_c , coupling length, L_c and distance between the two fibers, d , are taken into account in order to obtain the coupling efficiency between the two fibers. The bent fiber using circular and elliptical blocks encourages the modes to radiate out of the tapered section. The amount of power transfer is calculated using Coupled Mode Theory. The coupling length between the two fibers also affects the coupling efficiency [24].

1.9.1. Taper

Taper changes the fiber diameter or thickness which allows redistribution of the modes in the core or eliminates the modes. The penetration depth of the evanescent field and proportion of power within this field increases in the tapered section. The modified core-cladding thickness is used for coupling fibers or interface fibers to devices [13]. In [17] in their research stated that they polished the fiber for several micrometers and lapped the fibers together and when source is inserted, mode will couple between the lapping regions and split the light accordingly. By adjusting the alignment between the two lapping fibers, the strength of the evanescent light coupling can be tuned. However, [17] do not apply mechanical technique of circular and elliptical blocks to vary the splitting ratios, rather the alignment is varied. In [13] in the other hand manipulate the thickness of cladding in order to obtain desired results. In [25] states that at the end of the tapering section of the first fiber, the rays propagate in the cladding will be recaptured by the core. If the tapering section of parallel fibers is small, the coupling ratio is high. However, if the radius of the tapered section is too small, the coupling efficiency will decrease dramatically due to the lost rays while passing through the down taper.

For some tapered fibers in this research, whole surfaces were etched around the fiber creating extra taper regions that allows unnecessary losses of the splitter. Thus, circular and elliptical blocks were made of acrylic and when the fibers are placed in the groove, the non-lapping surfaces are surrounded by acrylic material. This material is aimed to reduce the losses of the splitter due to tapering of the fiber cladding.

1.9.2. Bending and radiation

Generally, loss is high when the bending is smaller. Radiation loss occurs in the cladding even when the propagating ray is greater than critical angle. If light facing total internal reflection, an electromagnetic disturbance occurs which is known as evanescent wave where it penetrate the reflecting interface. Non-uniformity in the reflecting interface may cause the evanescent wave to convert into propagating wave where in bending loss, evanescent fields extend to the cladding but decay exponentially with radial distance [26].

The loss in bent step-index multimode fibers not only depends on bending but also on the cladding thickness [11]. When a refracting ray hits a core-cladding interface, two rays are created where one ray is refracting at the cladding interface while the other ray is tunneling at inner core interface. At cladding interface, some rays will be reflected back and some will be refracted with considerable power content [27]. By decreasing the bend radius and increasing fiber core, losses will increase. As bend radius begins to decrease, more refracting rays are produced and more power is transferred to the cladding [28].

Some rays in the incident radiation are not bounded by core of the fiber rather the rays that propagate through the core-cladding interface and get into the cladding region. Due to the finite radius of curvature at the cladding surface, some of the rays will be reflected back into the cladding and propagates while some will radiate. The rays that propagate in the cladding are known as the cladding modes and coupling can occur with the higher-order modes of the core resulting in loss of the core power. According to [27], the refracting rays lost most part of their energy at the beginning of the bent section and then the rate of loss will be slower whilst the remaining losses afterwards are due to weakly leaky rays which are known as whispery gallery rays of tunneling rays.

Therefore, this research integrate the concept of taper, lapping and bending the splitter in order to increase or limiting the splitting or coupling of rays between the two lapping fibers in order to gain certain splitting ratios.

1.9.3. Coupling length

The coupling efficiency describes the total power of coupling between the two fibers depending on the distance, fiber core thickness and length of the contact region. In [14] stated that cross type coupler is not able to achieve high coupling efficiency due to its short coupling length. Coupling length must be long in order to achieve high coupling efficiency such as parallel type coupler. For short coupling length, coupling is dominant only for higher order modes. In cross type coupler, the radiation loss is increased by increasing the pressure since the coupling length is quite short in order to gain optimum result. In [14] shows that as the

coupling length is longer, the coupling efficiency will be stabilized. However, high coupling efficiency is achieved at coupling length between 6 to 10 mm and from 18 to 22 mm.

1.9.4. Distance of cores

In [29] agrees that the distance between the two fibers affects the coupling efficiency among other considered parameters. Although coupling length is important, however, the optimum efficiency of coupling not only depends on the optimum length but also on the distance between the two cores. In [29] shows that when the gap is zero between the lapping cores, high coupling efficiency is achieved, however, when gap exists or distance over the two cores is 1.01, the coupling efficiency drops to less than 30%. When the gap or distance over the two cores is further increased to 1.05, the efficiency drops to less than 5%. The distance between the two fibers affects the coupling efficiency strongly.

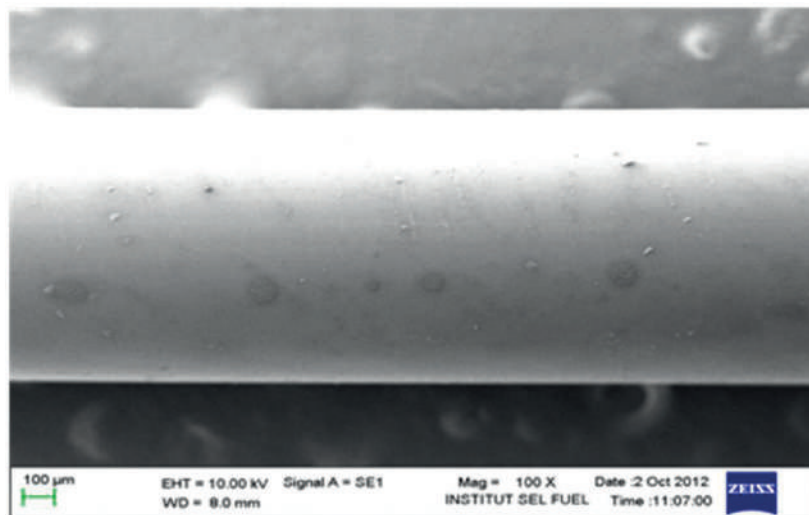
According to [25] states that when the ray of light propagates along the tapered section of the lapping fiber, the angle of incidence on the core surface decreases with each reflection and the high-order modes may have cutoff points in the down-taper section and therefore will leak out the core. If the cladding modes encounter the air-cladding interface at incident angles smaller than the critical angle, the modes will radiate away from the fiber at the air-cladding interface. However, if the claddings of the two lapping fibers are closed enough over appropriate length, the light in the cladding of the fiber will be transferred to the second fiber.

Therefore, load is accounted in this research in order to minimize if not eliminate the gap between the two lapping cores. The difference of characterization is compared when normal force is exerted and external force is exerted.

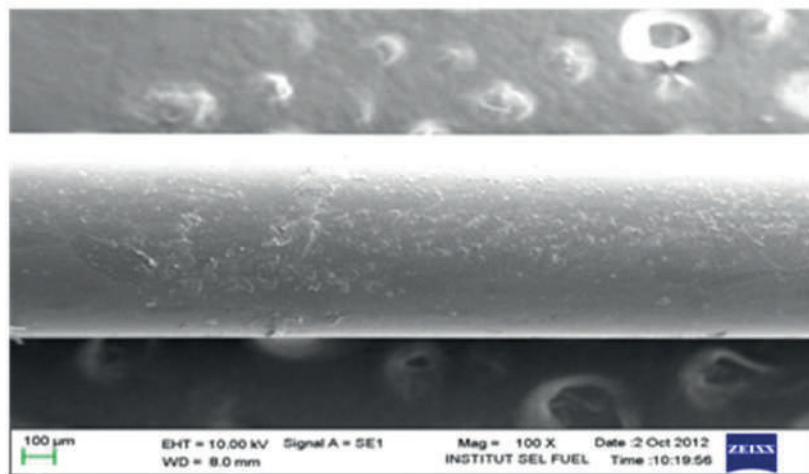
1.10. Fiber preparation development

Apart from the platform design, the development of the coupler/splitter also comprises of three sets of fibers tapered by etching method and side polishing. The first set of fibers were prepared by fully etching using harmless chemical solvent, acetone. During the etching process, the tapered length of each fiber was set to be 25 mm long and the duration of each pair of the fiber strands was varied from 30 to 120 minutes. For second set of fibers using fully etching method, the etching length of tapered length of the fibers were varied for each pair between 4 and 25 mm long and the duration of etching also was set to 60 minutes. The third set of fiber pairs were tapered using side polishing method and side etching where only one side of the fiber strand was polished and etched to clean the rugged surfaces. The tapered length of the fiber pair of each coupler/splitter is also varied from 4 to 25 mm long and the duration of etching is about 60 minutes. The effect of etching duration leads to the different diameter of core-cladding of the fiber pairs. The longer the etching process, the smaller the core thickness diameter. **Figure 2(a)–(c)** show the surface of the fibers before etching process, **Figure 2(a)** and post etching fiber, **Figure 2(b)**.

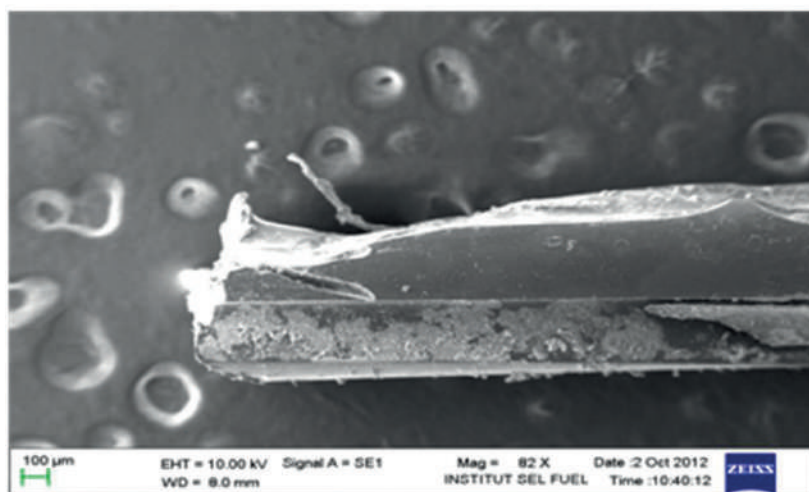
This shows that the physical property of the fiber strand is sustained when the fiber is tapered using chemical solvent. However, when the fiber is etched while it is in bending state, brittleness occurs and leads the fiber to break apart. **Figure 2(c)** shows the physical state of the fiber



(a)



(b)



(c)

Figure 2. Physical surface of the (a) pre-etch (b) post-etch fiber and (c) fiber breaks due to brittleness.

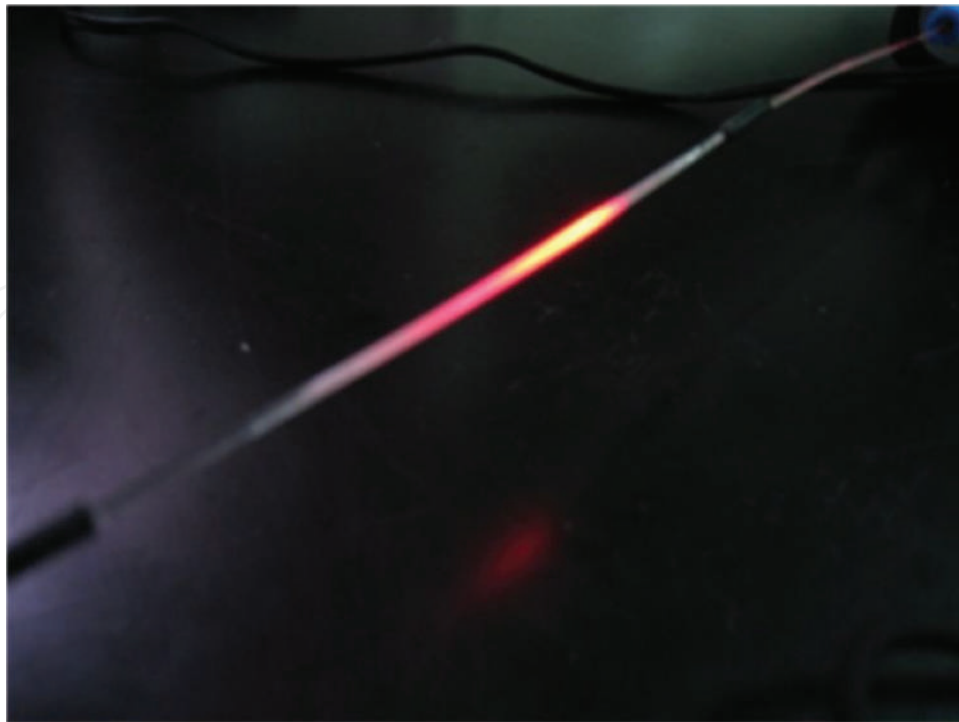


Figure 3. The light transmitted over the etched fiber.

when brittleness causes the fiber to break. **Figure 3** shows the light signal transmitted over the etched fiber and it shows that the light spread out at the etched region only and due to this behavior, insertion loss increases and output power decreases.

1.11. Platform development

The coupler/splitter platform is one of the important parts of developing this directional coupler using lapping technique and geometrical blocks. The platform of the coupler is customized using acrylic material. The platform of the fiber coupler/splitter is consisted of mainly circular/elliptical blocks of various radii, made of acrylic material that has similar refractive index as the cladding of the fiber.

1.11.1. Circular

The first phase of platform development involves the development of circular blocks made of acrylic material as shown in **Figure 4**. The circular block functions to hold the etched fibers while the fibers will be bent accordingly to the bending radius of the circular blocks. A groove of 1 mm is carved along the edge of the blocks in order to place and hold the fibers as shown in **Figure 5**. The tapered area of the fiber is facing outward of the groove and will be lapped to the other tapered surface so that coupling or splitting between the two fibers can occur. The etched area or surface that is not facing or lapping to the other fiber is covered by the groove of the blocks that are made from acrylic. Acrylic material has similar refractive index as the cladding layer, $n = 1.402$. Therefore, the unlapping surface of the etched area is covered

by similar cladding layer refractive index. Thus, when the propagating modes are traveling along the etched fiber, some of the modes will be transferred to the other lapped fiber while some the modes that radiated out of the unlapping area is bounded by similarly refractive index of cladding, that is the groove of the block. Therefore, this will decrease the loss. The pivot is designed to hold the etched fibers that are placed at the groove so that they do not move and the tapered surfaces are lapped to each other. The screws of the pivots are used to loosen and tighten the pivot accordingly so when other block of bending radius is placed, the fiber can be bent according to the bending radius of the circular blocks.

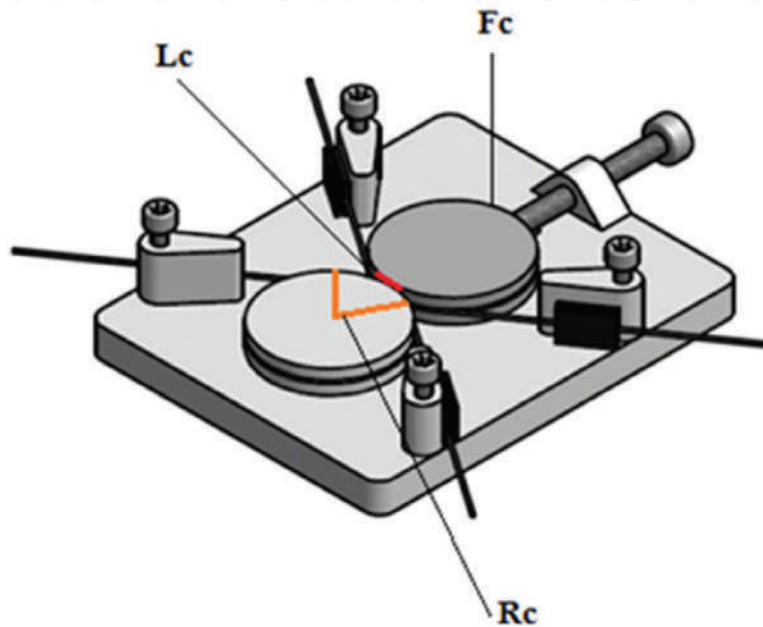


Figure 4. Circular blocks platform and fibers lapped.

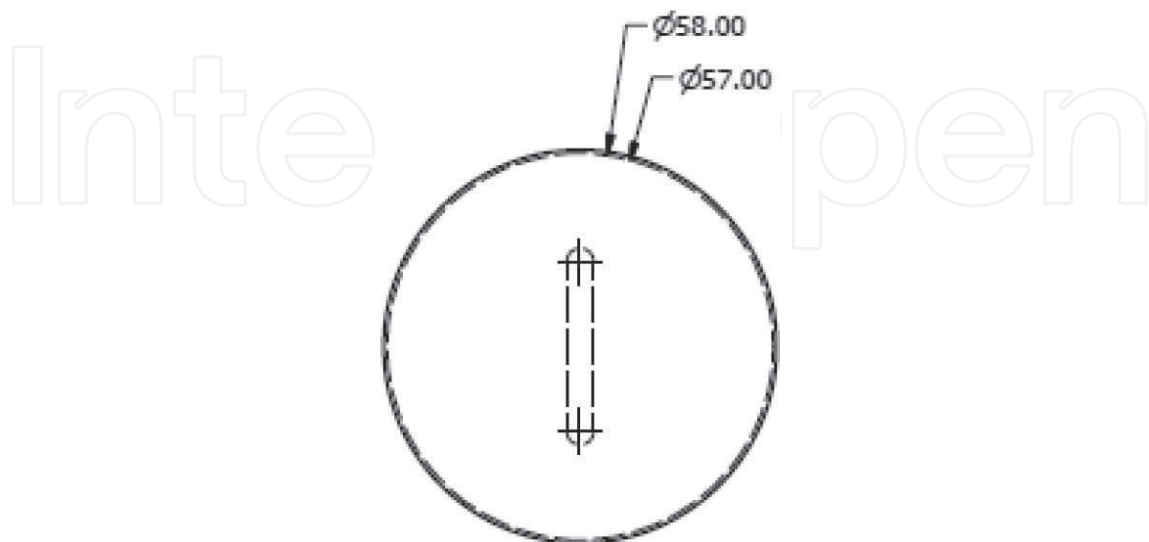


Figure 5. The bottom view of a circular block with groove showing at the round edge of the block.

1.11.2. Elliptical

Elliptical blocks shape are designed apart from circular blocks as another geometrical shape in order to study the effect of different bending radius, R_c , and coupling length, L_c , between the two lapped fibers. Apart from circular blocks having bending radius or curve that is more critical than elliptical shape, circular blocks are used to mainly study the effect of bending radius when the fibers of the coupler are bent at certain bending radii. Elliptical shapes in the other hand, when fibers are attached to the elliptical blocks and bent, the bending radii are less curvier than that of circular blocks, however, the curves of ellipse shape blocks are more flatter thus the coupling length between the two lapped fibers are longer than that of circular blocks. Bending does play part in order to stimulate the transfer of modes from the first fiber to the second one, however, another parameter that also play an important part is coupling length, L_c . The bending radius of elliptical shapes range from 10 to 29 mm. The bigger the bending radius of the elliptical shapes, the longer the lapping region between the two lapping cores. **Figure 6** shows the dimensions of the elliptical platform together with the force gauge embedded in the design. The experiment platform is big as to characterize and analyze which bending radius range is the most optimum to be used and developed as an efficient optical coupler/splitter using lapping technique.

1.11.3. Semi-elliptical

The third phase of the development is using semi-elliptical shaped blocks and platform with spring embedded as shown in **Figure 7**. The semi-elliptical shaped blocks have bending radius of 30, 40 and 50 mm. No force gauge is used on this platform because the force is exerted unto the blocks and fibers by the spring embedded in the platform.

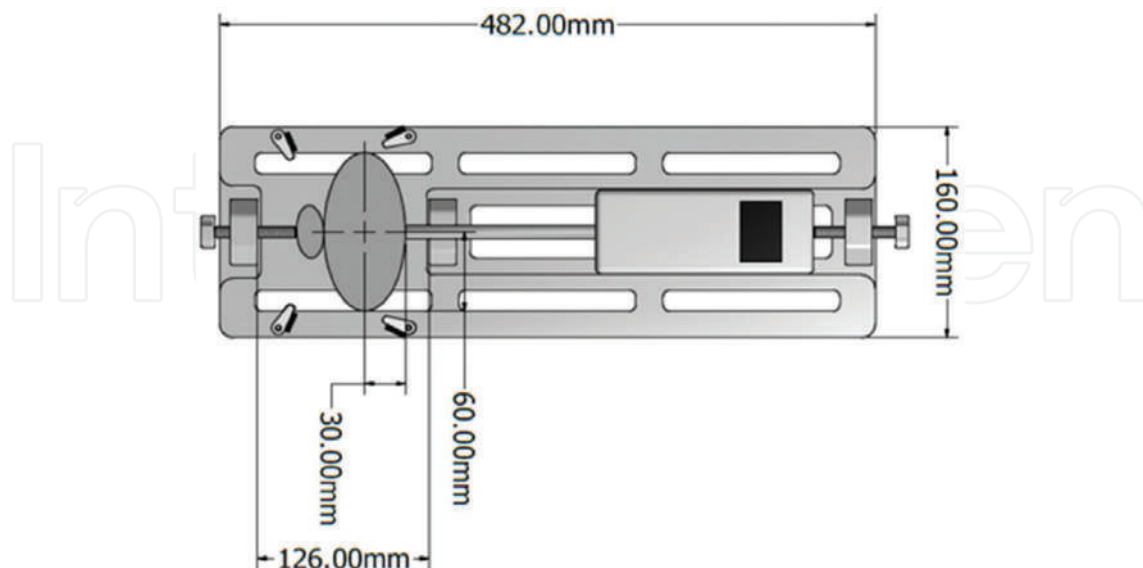


Figure 6. Elliptical blocks platform design measurement with ellipse-shaped blocks.

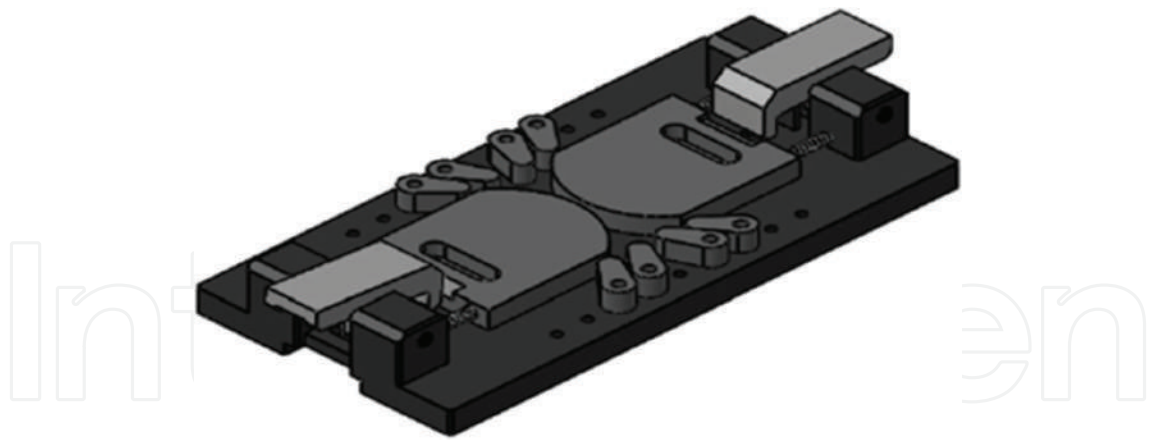


Figure 7. Coupler/splitter experimental platform using semi-elliptical blocks and embedded spring.

1.12. Coupling efficiency by integration of CMT and Hertz's law

The amount of power transfer is relatively in accordance to the coupling length. Thus, in this study, two very important theories are applied where the force exerted on the fiber through geometrical blocks relates to elliptical point contacts of Hertz's Law [30] and the amount of force put upon the fibers determines the radius of contact area or coupling length which brings to Couple Mode Theory. The propagation of modes between the two fibers is studied analytically and coupling efficiencies are obtained by varying the load force, coupling lengths and the distances between the two fibers.

To obtain an efficient coupling ratio or splitting ratio, the coupling length between the two lapped fibers must be long in order to obtain an adequate level of coupling efficiency. In this research, two similarly fibers were tapered at the middle region with particular diameter of core-cladding. They are attached to the circular blocks/elliptical blocks of certain bending radius that determines the bending angle of the lapped fibers that helps the transfer of energy from primary fiber to the secondary fiber. The performance of the splitter/coupler is analyzed through the relationship of the distance between the two fiber waveguides and the load put upon the blocks and fibers which gives effect in the coupling length. For the multimode step index fiber, a group of modes exist as according to parameters assigned by the optical waveguides. Between reflections of each of the propagation rays, each ray travels in straight line and Snell's Law determines the reflection on the interface [31].

Coupling efficiency is calculated by first specifying the coupling length, L_c , which in this design is assumed to be directly relative to radius of contact area, c , of Hertz's ellipsoid. Coupling efficiency is done by integrating the coupling coefficient and coupling length.

$$\eta = \frac{P_{A \rightarrow B}}{P_{in}} \cong \frac{1}{N} \int_0^1 \sin \left(\frac{(2^{1/4} \Delta^{1/4}) L_c}{\sqrt{\pi k n_0} D_c^{3/2}} t (1-t)^{1/4} \right)^2 dt \quad (1)$$

$$\eta = \left(\int_0^1 \sin (C_{coef} \cdot L_c)^2 dt \right) \quad (2)$$

Here the relationship between CMT and Hertz's can be focused on coupling length or twice the radius of contact area of the elliptical point contacts of two spheres.

$$\eta = \int_0^1 \sin \left[\left(\frac{1}{\sqrt{\pi}} \frac{\sqrt{\text{NA}(n_0, n_1)}}{\sqrt{k(\lambda) \cdot (D_c) \cdot (n_0)}} \right) \left(\frac{t \cdot (1-t)^{1/4}}{D_c} \right) (2) \left(\sqrt[3]{\frac{3 \cdot F \cdot (\text{Re})}{4 \cdot E}} \right) \left[(F1) \left(\frac{R1}{R2} \right) \right] \right]^2 dt \quad (3)$$

This expression will be used to vary the distance between the two fibers having different load F_c and the coupling efficiency of the splitter can be determined accordingly.

1.13. Performance

During characterization of the couplers/splitters, the experimental set-up is first prepared as shown in **Figure 8**. Geometrical blocks of different radii are placed on the platform with pair of tapered cladding secured in the groove of the circular/elliptical blocks. At each of the ports of splitter/coupler except at the input port, power meter is set to take readings of the output power. Red LED of $\lambda = 650 \text{ nm}$ is injected through input port and normal force of $F_n = 0.3 \text{ lbF}$ is exerted upon the middle region of the coupler/splitter through the geometrical blocks as shown in **Figure 8**. Normal force is the reading at which the two cores of the fibers touch each other without any external force. Output power is taken accordingly at each port. Then, given force or external pressure is exerted upon the blocks and fibers, namely $F_c = 3.0 \text{ lbF}$. This external pressure is presumed to minimize the air gap that existed between the two lapped cores.

The experiment was repeated twice as in the first test, normal force is exerted upon the blocks and the fiber cores and in the second test, external force is exerted upon the blocks and the fiber cores. Based on the data collected, efficiency of each coupler/splitter can be measured. The efficiency of a coupler/splitter, σ can be defined as power ratio of overall output, ΣP_o against the power input, P_1 . The mathematical equation that refers to the coupler/splitter efficiency is:

$$\Sigma P_o = P_2 + P_3 + P_4 \quad (4)$$

$$\sigma (\%) = \frac{\Sigma P_o}{P_1} \times 100\% \quad (5)$$

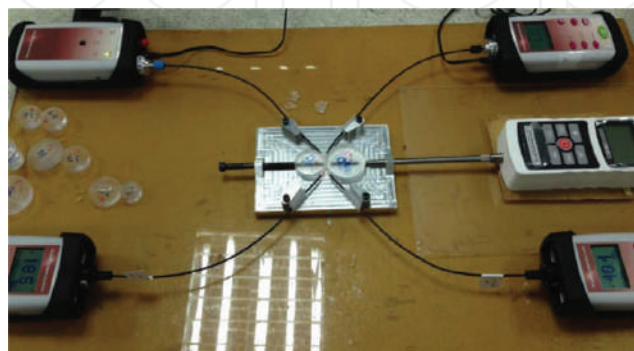


Figure 8. Experimental set-up platform with force gauge.

P_2 , P_3 and P_4 are the output power of the light signal that propagates out of the throughput port, P_2 , coupled port, P_3 and reflected port, P_4 , while P_1 is the input port of the injected light signal.

The objective of this work which is to apply theories of CMT and Hertz's Law in studying the effect on coupling efficiency by manipulating the cores and coupling lengths between the fibers are analyzed and the optimum efficiency obtained shows that when the two fiber cores are closed to each other, the efficiency lies between 40% and 70% depending on the coupling length and distance is zero. When force exertion is small, the coupling length decreases thus coupling efficiency decreases to less than 50%. It decreases when the force, F_c is less and the coupling length, L_c is shorter. The efficiency decreases as the distance, d , between the two fiber cores is bigger. The optimum range of efficiency achieved based on coupling length, L_c , depends on the fiber core size, D_c . The diameter of the cores affects the efficiency where optimum efficiency is achieved at shorter coupling length range when the core diameter is smaller. This study gives an insight of the optimum distance and fiber core size of the lapping fibers used in the experiment.

Experimental results show the splitters having different splitting ratios as high as 80% to as low as 1%. Each of the splitter has different bending radius, R_c and different tapered length, L_c . Macro-bending effect shows that different bending radius of circular and elliptical blocks allow different bending angle for each splitter. Small angle of bending leads to radiation of rays that propagate along the bent section. The radiation is enhanced by the tapered regions at the bent section where some of the cladding layers are etched to allow coupling between the lapping sections. Different core-cladding thickness may influence the amount of rays coupling into second fiber. Large bending radius in the other hand slows the radiation rate, however, helps the splitting and coupling by lengthen the lapping region or coupling length. Diameters of 0.88 mm of splitters show optimum splitting ratios such as 80%, 70% and 60%. However the losses are high due to the surfaces of the tapered fibers that were etched wholly around the surfaces. The non-lapping section may contribute to the losses. Diameters of 0.77 mm in the other hand give splitting ratios between 20% and 50% with considerable losses. All bending platform of circular, elliptical and semi-elliptical blocks contribute to these range of splitting ratios. Side-polished and side-etched splitters and fully etched splitters with varied etched length are mostly used with the platforms to obtain optimum results. Long tapered region as given by fully etched fibers with constant etched length shows very low splitting ratios with considerable high losses. However, shortest tapered region does not give the most optimum results. Therefore, depending on each parameter, particular tapered length, diameter and bending have to be considered into the design to obtain desired optimum results.

1.14. Maintenance and reproducibility

Another important attributes that represents a coupler include its flexibility, maintenance and reproducibility. The device is flexible since the fiber pair and blocks can be exchanged in order to get desired splitting ratio. Even though the blocks needs to be exchanged for obtaining desired splitting ratio, the blocks and fibers are ready to be fitted into platform and they are highly durable. Since the splitter is custom-made, the splitter can be reproduced by handling

each process of fabrication meticulously to the etching rate, polishing rate and bending size in order to achieve uniform and persistent results.

1.15. Installations and performance

Installations and performances are very important attribute to any coupler or splitter developed. Although a coupler is a small component in a system, it does play an important role throughout the whole performance. Although the coupler/splitter developed has considerable higher loss than the ones in the market line, the ability of the coupler to achieve several splitting ratio has high potential where improvements and expandability of the device can be done in order for the device to compete in the market line.

The device developed is easy to install using prepared platform and mix matched fiber pair and blocks where varied splitting ratio can be obtained using one platform. Although targeted loss is considerably higher than marketed splitter, however, the device is applicable for signal transmittance and applications. The device developed is green technology-based since the production process is using eco-friendly material, harmless solvent, moreover, LED source is used which is very safe for consumers.

1.16. Research future Prospect

The limitation of "DIY" kit can be overcome by this design. Since the design of this splitter gives several solution of splitting ratios, users that demand different value of splitting ratios can utilize the splitters. Although the prototype design for users are yet to be finalized, however, based on the results shown, the platform shows good performance and can be realized as DIY kit. Apart from that, since the cost of POF is low and materials and tools needed to build the platform are inexpensive and does not involve high-end expensive machine, this device has low-cost production and very economic. The material used to develop this device such as POF, harmless chemical solvent, acrylic and aluminum are safe and green technology based.

1.17. Summary

New technique of developing an optical coupler using POF and mechanical platform using lapping technique is discussed and analyzed in this chapter. Three different categories of splitters are prepared where the first category of splitters has constant etching length of 25 mm and the diameter of the tapered section is varied. The second category is splitters that have been etched with different length between 4 and 25 mm but having constant diameters of 0.88 mm. The third category is splitters that have been polished and etched at one side of the fibers only having different etching length between 4 and 25 mm and constant diameter of 0.77 mm. Three different platforms are also built. The first platform having small angle of circular blocks, the second platform having larger angle of elliptical blocks and the third platform having intermediate angle between small and large angle of semi-elliptical blocks with spring embedded. Varied angles represented by the bending radii of the blocks are chosen and designed in order to study the bending effect of the splitter. Different bending radius with combination of fiber diameter and coupling length leads different coupling behavior between the two lapping regions and therefore provides different splitting ratios.

Author details

Latifah S. Supian^{1*}, Mohd Syuhaimi Ab-Rahman², Norhana Arsad², Chew Sue Ping¹, Nani Fadzlina Naim³, Nurdiani Zamhari⁴ and Syed Mohd Fairuz Syed Mohd Dardin¹

*Address all correspondence to: sarah@upnm.edu.my or cawa711@gmail.com

1 Department of Electrical and Electronics Engineering, Faculty of Engineering, Universiti Pertahanan Nasional Malaysia, Kuala Lumpur, Malaysia

2 Department of Electric, Electronics and Systems Engineering, Faculty of Engineering and Built Environment, Universiti Kebangsaan Malaysia, Bangi, Selangor, Malaysia

3 Faculty of Electrical Engineering, Engineering Complex, Universiti Teknologi MARA, Shah Alam, Selangor, Malaysia

4 Department of Electrical and Electronics Engineering, Faculty of Engineering, Universiti Malaysia Sarawak, Kota Samarahan, Sarawak, Malaysia

References

- [1] IGI Consulting. Plastic Optical Fiber Market & Technology Assessment Study. Boston, MA: IGI Group, Information Gatekeepers Inc.; 2011
- [2] Khoe GD, Boom H, Monroy IT. High Capacity Transmission Systems. Polymer Optical Fiber. Stevenson Ranch: American Scientific Publisher; 2004
- [3] Nalwa HS. Polymer Optical Fiber. Stevenson Ranch: American Scientific Publisher; 2004
- [4] Supian LS, Ab-Rahman MS, Arsad N. Etching technique study for POF coupler fabrication using circular blocks. *Optik Journal*. 2014;**125**:893-896. Elsevier
- [5] Supian LS, Ab-Rahman MS. Polymer optical fiber coupler fabrication using chemical etching and lapping technique. In: 4th International Conference on Photonics (ICP 2013); Malacca, Malaysia; IEEE; 2013. pp. 184-186. DOI: 10.1109/ICP.2013.6687108. ISBN: 978-1-4673-6073-9
- [6] Ghatak A. Optics. New Delhi: McGraw Hill Education; 2013
- [7] Ab-Rahman MS, Guna H, Harun MH, Supian L, Jumari K. Integration of ecofriendly splitter and optical filter for low-cost WDM network solution. In: *Optical Fiber Communication and Devices*. InTech; 2012. ISBN: 978-953-307-954-7
- [8] Strategic Services Division. Acetone. [online]. Available from: <http://hazard.com/msds/mf/baker/baker/files/a0446.html> [Accessed: Jan 15, 2015]
- [9] Lin CF. Optical Components for Communications: Principles and Applications. Boston: Kluwer; 2010

- [10] Chen CL. *Optical Directional Couplers and their Applications*. Hoboken, USA: John Wiley & Sons, Inc.; 2007
- [11] Love JD, Durniak C. Bend loss, tapering and cladding-mode coupling in single-mode fibers. *IEEE Photonics Technology Letters*. 2007;**19**(16):1257-1259
- [12] Ji F, Xu L, Li F, Gu C, Gao K, Ming H. Simulation and experimental research on polymer fiber mode selection polished coupler. *Chinese Optics Letter*. 2008;**6**(1):16
- [13] Merchant DF, Scully PJ, Schmitt NF. Chemical tapering of polymer optical fiber. *Sensors and Actuators A: Physical Elsevier*. 2000;**76**(1-3):365-371
- [14] Ogawa K, McCormick AR. Multimode fiber coupler. *Applied Optics*. 1978;**17**(13):2077-2079
- [15] Tanaka T, Serizawa H, Tsujimoto Y. Characteristics of directional couplers with lapped multimode fibers. *Applied Optics*. 1980;**19**(20):2019-2024
- [16] Findakly T, Chen CL. Optical directional couplers with variable spacing. *Applied Optics*. 1978;**17**(5):769-773
- [17] Kawase LR, Santos JC, Silva LPC, Ribeiro RM, Canedo J, Werneck MM. Comparison of different fabrication techniques for POF couplers. In: *The International POF Technical Conference, Cambridge, Massachusetts*. Boston, MA: Information Gatekeepers, Inc.; 2000. pp. 68-71
- [18] Gloge D. Bending loss in multimode fibers with graded and ungraded core index. *Applied Optics*. 1972;**11**(11):2506-2513
- [19] Barnoski MK, Friedrich HR. Fabrication of an access coupler with single-strand multimode fiber waveguides. *Applied Optics*. 1976;**15**(11):2629-2630
- [20] Musa S, Borreman A, Kok AM, Diemeer MJB, Driessen A. Experimental study of bent multimode optical waveguides. *Applied Optics*. 2004;**43**:5705-5707
- [21] Supian LS, Ab-Rahman MS, Arsad N, Ramza H. Study of macro-bending of polymer fiber in multimode POF couplers development by lapping technique. *International Journal of New Computer Architectures and their Applications (IJNCAA)*. 2014;**4**(1):39-47. The Society of Digital Information and Wireless Communications. (ISSN: 2220-9085)
- [22] Badar AH, Maclean TSM, Gazey BK, Miller JF, Shiraz HG. Radiation from circular bends in multimode and single-mode optical fibres. *IEEE Proceedings*. 1989;**136**(3):147-151
- [23] Supian LS, Ab-Rahman MS, Arsad N. The study on pressure effect on characterization of directional coupler for different thickness of fiber cores in POF splitter development. In: *The 2nd International Symposium on Telecommunication Technologies (ISTT 2014)*. Langkawi, Malaysia: IEEE; 2014. pp. 298-302. ISBN: 978-1-4799-5981-5/14
- [24] Supian LS, Ab-Rahman MS, Ramza H, Arsad N. Characteristics study of multimode directional coupler by elliptical point contacts and CMT. In: *2nd International Conference on Applications of Optics and Photonics Proceedings of SPIE*. San Francisco, USA. Vol. 9286 92863K-1. 2014. DOI: 10.1117/12.2063541

- [25] Li YF, Lit WY. Coupling efficiency of a multimode biconical taper coupler. *Journal of Optical Society of America A*. 1985;**2**(8):1301-1306
- [26] Marcuse D. Curvature loss formula for optical fibers. *Journal of Optical Society of America*. 1975;**66**(3):216-220
- [27] Durana G, Zubia J, Arrue J, Aldabaldetrekua G, Mateo J. Dependence of bending losses on cladding thickness in plastic optical fibers. *Applied Optics*. 2003;**42**:997-1002
- [28] Winkler C, Love JD, Ghatak AK. Loss calculations in bent multimode optical waveguides. *Optical and Quantum Electronics*. 1979;**11**:173-183
- [29] Ogawa K. Simplified theory of the multimode fiber coupler. *The Bell System Technical Journal*. 1977;**56**(5):729-745
- [30] Johnson KL. *Contact Mechanics*. Cambridge: Cambridge University Press; 1985
- [31] Snyder AW, Love JD. *Optical Waveguide Theory*. New York: Chapman and Hall; 1983

Plastic Optical Fibre Sensor System Design Using the Field Programmable Gate Array

Yong Sheng Ong, Ian Grout, Elfed Lewis and
Waleed Mohammed

Additional information is available at the end of the chapter

<http://dx.doi.org/10.5772/intechopen.71451>

Abstract

Extrinsic optical fibre sensor (OFS) systems use a fibre optic cable as the medium for signal propagation between the sensor and the sensor electronics using light rather than electrical signals. A range of different optical fibre sensors have been developed and electronic hardware system designs interfacing the sensor with external electronic systems devised. In this chapter, the use of the field programmable gate array (FPGA) is considered to implement the circuit functions that are required within a portable optical fibre sensor system that uses a light emitting diode (LED) as the light source, a photodiode as the light receiver and the FPGA to implement the system control, digital signal processing (DSP) and communications operations. The capabilities of the FPGA will be investigated and a case study sensor design introduced and elaborated. The OFS system will be based on the FPGA and will provide wireless communications to an external supervisory system. The chapter will commence with an overview of OFS systems and the typical architecture of the system. Then the FPGA will be introduced and discussed as a hardware alternative to a software programmed processor that is currently widely used. A case study will then be presented with a discussion into design considerations.

Keywords: optical fibre sensor, field programmable gate array, electronic system design, SPR sensor, Python

1. Introduction

Recent advances in optical fibre sensing technology have been rapid and widespread stimulated through achievements in developing sensors for applications such as environmental monitoring, mechanical structure stress and strain monitoring, and biomedical [1–4]. Advances in sensor fabrication, sensitivity enhancement and the availability of new materials have demonstrated the potential of using optical sensors in new applications. The aim is to harness the

advantages that optical components can provide over electrical component alternatives in a wide range of sensor applications. However, identifying and using suitable enabling technologies, supported through experience in achieving repeatable results from suitable experiments for new OFS industrial applications, should be recognised as key in moving forward from a research idea into application [5].

It is widely accepted that initial OFS designs were fragile, reliable only under laboratory conditions and with material costs higher than those used in other sensor technologies [6, 7]. They were also difficult to produce and this limited their ability for practical use. However, with an increase in the availability of new materials, the proliferation of inexpensive 3D printing and other additive manufacturing technologies that enable rapid prototyping and analysis, sensor design and packaging performance have been improved dramatically. These OFS packaging improvements have enabled optical fibre sensor (OFS) deployment [8] in a wide range of different applications as referenced above. An OFS system is however not complete without supporting instrumentation [9]. It requires a suitable electronic system to implement system functions that include system control, sensor stimulus generation, data acquisition (DAQ) and storage, data analysis (high-speed digital signal processing (DSP) operations) and serial communications interfacing. To date, OFS system deployment is still largely dependent on laboratory-based sub-systems, particularly the light source and optical receiver that interface to a computer through a data acquisition (DAQ) module or proprietary software via universal serial bus (USB). A typical OFS system needs to use high-cost and complex instruments to provide the necessary control and measurement capabilities, and usually depends on a human operator to set-up the light source and access the sensor results. To make optical sensors more accessible, the use of high quality but lower cost equipment is required. Some improvements have been noted in recent system designs where operations were performed using a software programmed microcontroller based arrangement [10–12]. The potential also exists to create supporting instrumentation that can harness inexpensive and physically smaller components to make an OFS system portable (i.e. a battery operated system capable of operating independently for extended periods of time, small physical size, programmable with wireless communications and ability to be carried by an individual, e.g. a first responder). The low cost aspect however must not compromise the quality of the system operation and it must also have reliable operation in the intended application. The inert nature of optical fibre also allows it to perform in-situ measurements in harsh environments whilst the sensitive electronic circuits can be shielded at an appropriate location and remotely from the environment being sensed. In addition, for complex photonic system design, photonic integrated circuit (IC) technology is a promising solution to achieve lower cost and miniaturisation, but is still not yet as mature as electronic technology [13].

This chapter will consider the electronic system design requirements for a portable OFS system based on the use of a microcontroller alternative. Specifically, the field programmable gate array (FPGA) is used to implement the necessary digital logic functions in hardware including light emitting diode (LED) (light source) switching and current control and photodiode (light receiver) signal sampling and signal conditioning. A plastic optical fibre (POF) arrangement is considered, although the focus of the chapter will be on the FPGA based electronic system design approaches and potential solutions. The chapter will consider the system design, both

analogue and digital parts, and will develop a discussion into the use of the FPGA as a hardware based alternative to a software based processor design. The available hardware resources within the FPGA will be considered and approaches to using these resources will be discussed. The FPGA, as an alternative, provides potential benefits to system design and operation by using configured hardware that provides the potential for high speed operation, parallel processing (concurrent operation), high-speed embedded DSP operations and low-voltage/low-power capability. The available hardware resources within the FPGA, along with the capability for low-voltage and low-power operation, mean that a powerful whilst portable sensor system can be developed and deployed. This chapter will consider the potential benefits of using the FPGA in such sensor systems and the design choices required. The chapter will commence with an introduction to OFS systems and electronic system design using the FPGA. It will then discuss the use of the FPGA within an existing OFS system and the benefits the FPGA can provide before providing a conclusion.

In this chapter, the discussion will be based on a single sensor arrangement to demonstrate the use of the FPGA. However, the FPGA would be easily capable of interfacing to multiple sensors due to the availability of configurable hardware within the FPGA and the availability of a large number of programmable digital pins which can be configured to act as inputs, outputs or bi-directional pins. It would therefore be practical for the FPGA to be used in multiple (multipoint) and quasi-distributed OFS systems of the form shown in **Figure 1**. Additionally this concept may ultimately be extended to use in fully distributed systems, e.g. Rayleigh and Brillouin scattering based systems, utilising the considerable on-board capabilities of the FPGA in fulfilling the complex signal process required from these systems. However, this article is constrained to assessing the feasibility of a potential distributed OFS application where multiple 'single point' sensors are distributed in location but connected to

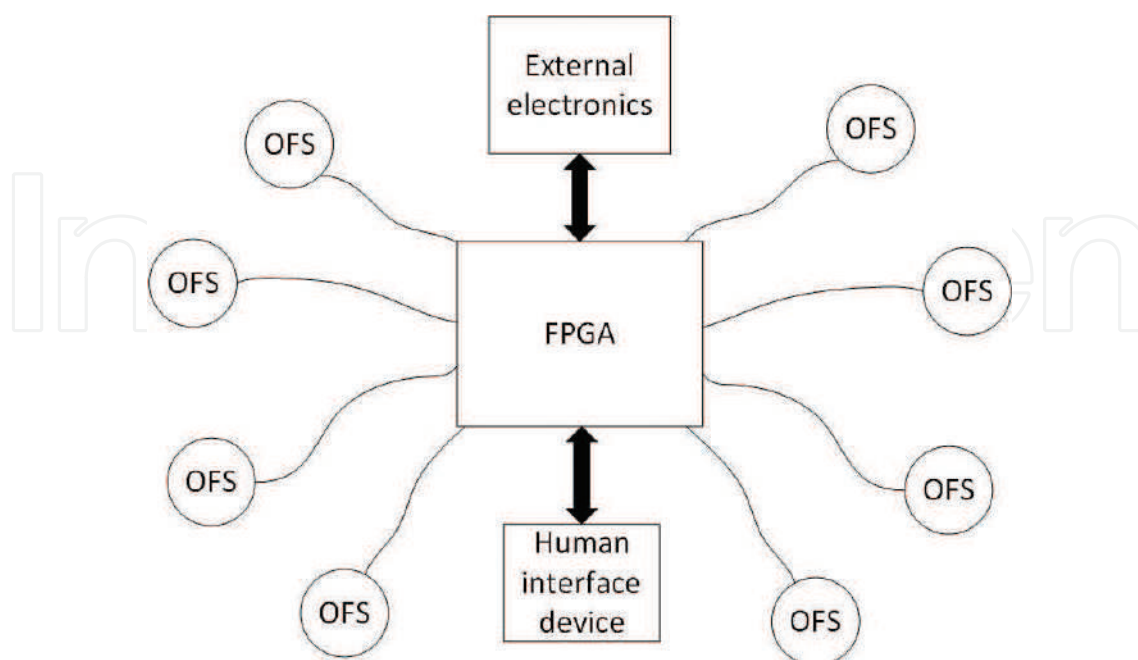


Figure 1. Distributed sensing with multiple 'single-point' sensors.

a single FPGA. The high number of available FPGA I/O pins are especially useful in allowing independent driving of multiple light sources and taking multiple light intensity measurements. Those measurements can be taken in a parallel manner and could be useful in phenomena detection [14]. Whilst the focus of this chapter is on a single ‘single point’ sensor, the basic design could be duplicated with other similar sensors and using the same FPGA to realise distributed sensing.

The chapter is structured as follows. Section 2 describes the OFS system operation and the design choices in the use of suitable components. Section 3 introduces the FPGA and how digital and mixed-signal electronic circuits and systems can be designed using the FPGA. This section also highlights a number of the advantages that the FPGA has over software programmed processor alternatives. Section 4 discusses the feasibility of use of the FPGA in an OFS system and Section 5 provides a real system based case study design using POF to provide an optical interface to the surface plasmon resonance (SPR) sensor. Section 6 concludes the paper.

2. Optical fibre sensor systems

2.1. Introduction

In this section, the structure and operation of a typical optical fibre sensor system is discussed. A typical OFS system essentially comprises of a light source, sensing element, optical detector and sensor data readout parts (external communications). A simplified architecture of such a system is shown in **Figure 2**. Light is guided from the light source to the optical receiver using an optical fibre. The sensing element is the part that transforms a change in the monitored parameter into a corresponding change in one or more of the physical properties of the guided light. Those properties include purely intensity, wavelength, polarisation orientation and phase. A change in the properties of the transmitted light through the sensor can be created by different physical mechanisms. For example, the chemical properties of a material being sensed. To capture the change in the propagated light properties, an appropriate light source

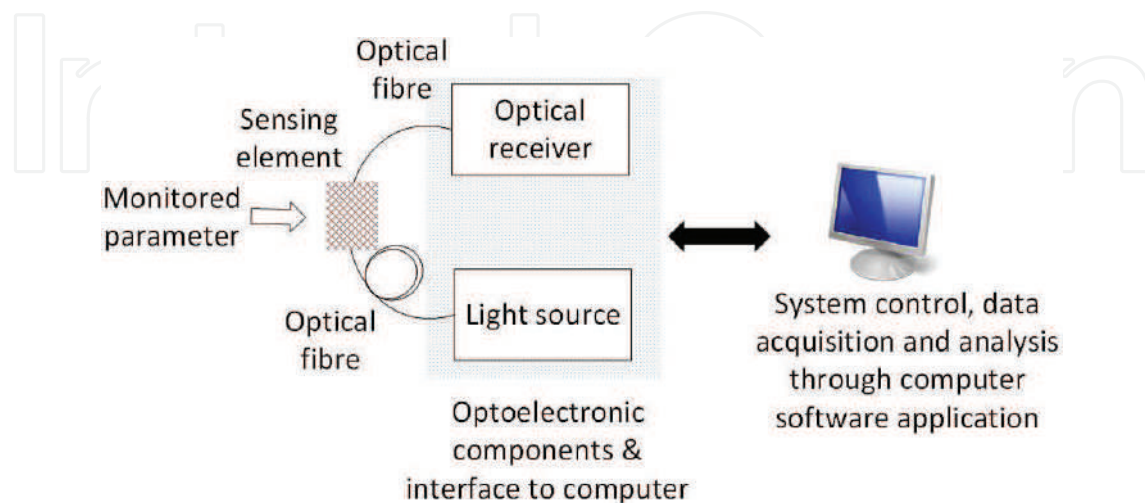


Figure 2. Simplified architecture of an OFS system (either intrinsic or extrinsic).

and matching optical receiver are required. The light source provides the sensor light stimulus of a particular wavelength or band of wavelengths to propagate to the sensing element. This light is modulated by the sensor and the resulting signal is captured by optical receiver. The optical parts of the system are linked together using an optical fibre cable. POF is becoming an increasingly popular choice in many sensors when compared to glass optical fibre (GOF) due to its low-cost, ease of connection and flexibility (allowing it to be mechanically bent and shaped to the requirements of the sensor housing and location). The source and receiver are electrically connected to the computing device that provides an optical-electrical interface, system control, communications and data analysis. The complexity of an OFS system is usually dependent on light modulation method used, the type of sensor and whether a single or multiple sensors are required. For example, distributed sensing requires complex light sources, coupling optics and receivers to obtain a sufficiently high-resolution result [14]. Distributed sensing ideally enables the measurement of any point along the optical fibre and is used in applications such as temperature, strain and acoustic sensing. Other OFS types include multi-point sensing or single point sensing [15, 16]. A multipoint sensor is similar to distributed sensing and therefore often also requires complex instrumentation although the cost of the interrogator unit is often much less than the fully distributed sensor. On the other hand, a single point sensor usually is the simplest form that requires less complex instrumentation. In all cases, the sensors may be classified as being either intrinsic or extrinsic. An intrinsic sensor uses the fibre itself as the sensor whilst in an extrinsic sensor, the fibre is used only used for light propagation to and from the sensor element which is therefore an external device. Clearly in the case of distributed sensors, e.g. Rayleigh or Brillouin, these are examples of intrinsic sensors.

The individual components of the OFS system are considered in the following sections.

2.2. Optical fibre

An optical fibre is a flexible optically transmitting waveguide that is drawn from glass or plastic [7]. In its simplest form, it is composed of three parts. Referring to **Figure 3**, these are the core, cladding, and coating. Both the core and cladding are made of a suitable dielectric

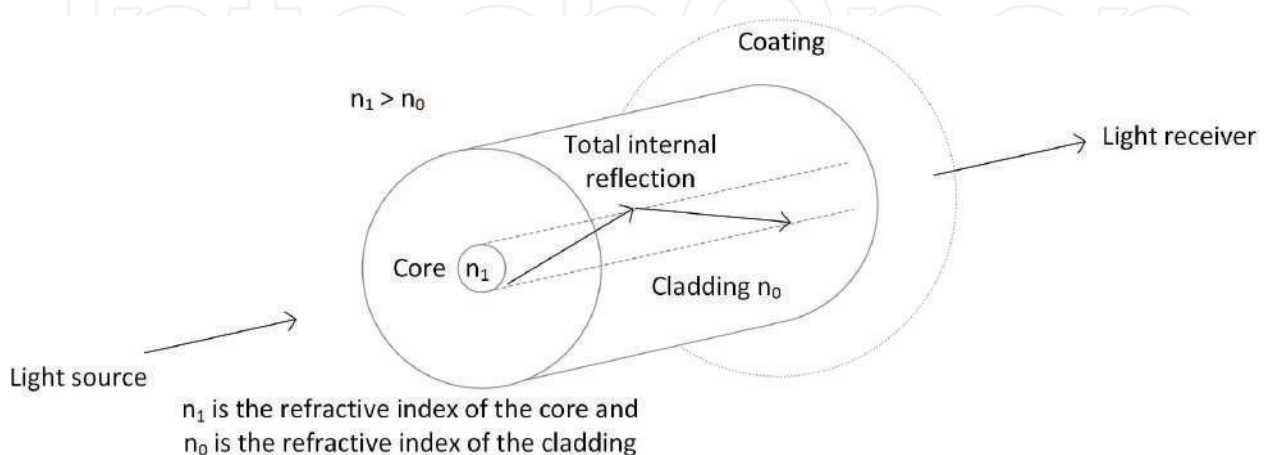


Figure 3. Optical fibre structure.

material, usually doped silica glass or a polymer. The core usually has a cylindrical cross-section and has higher refractive index (n) than the cladding that surrounds it. The coating is an additional layer of material, often a toughened polymer that provides protection from physical damage whilst maintaining flexibility. The interface of the core and cladding can be considered as a perfect abrupt but completely smooth boundary and the refractive index difference between the materials allows for total internal reflection to occur whilst minimising scattering losses [17]. In the case of total internal reflection, all of the light energy is ideally preserved within the core and allows the light to transmit through the fibre not only when the fibre is straight, but also when bent (up to a limit known as the minimum bend radius) as would be typically seen with a flexible fibre [7].

A number of fibre types are commercially available for different purposes and can be broadly categorised into two basic types: silica (glass) fibre or polymer (plastic) fibre. Glass fibre has widespread use in communications applications [18] due to its low-cost and material properties. It allows for extremely low loss long distance transmission of data with the need for fewer repeaters to boost signal strength due to losses in the transmission medium than would be required with electrical signal transmission. POF has found use in relatively short distance light transmission, e.g. in local area networks and, due to its flexibility, in situations that involve bending of the fibre, e.g. as in the case of automotive based networks. POF is generally large core fibre (i.e. a large fibre diameter, being typically 0.25 to 2 mm in diameter) that can bend into a smaller radius than can a silica fibre. There are some exceptions with much recent research being focused on single mode POF, e.g. for strain sensing [19]. Despite the material differences, both types of fibre operate under same principle of allowing the transmission of light. A major advantage of all optical fibres is that due to their material properties, an optical fibre is immune to external electrical interference. For example, unlike copper wiring, there is no cross-talk between signals in different close-proximity cables and no pickup of environmental noise, e.g. from proximal electrical machines or faulty electrical equipment. Recently, the application of the optical fibre has been extended from primarily a communications medium to the use as a sensor. An OFS introduces the idea of the modulation of a transmitted light signal as it propagates through a fibre and through different physical phenomena that are aimed to be measured [20]. Other specialist fibre types are available which result from novel structures or alternative materials. Photonic Crystal or Photonic Bandgap Fibres (PCF or PBF) rely on hollow or honeycomb (or many other sophisticated designs) patterned cores but currently their use is confined to some specialist applications, e.g. Supercontinuum Light sources [21]. Other specialist fibre materials are also available, e.g. Chalcogenide and ZBLAN for mid-infrared (MIR) operation, but again their use has been confined to some specialist sensing activities e.g. gas sensing [22].

2.3. Light source and optical detector

The light source and optical detector are fundamental parts of an OFS system. Both are required to have the necessary operating characteristics to be useful, are required to operate reliably over a long periods of time and to provide trustworthy data to the user. Light sources used to support low-cost optical fibre sensors are LED based and in some cases low-cost semiconductor laser diodes. Other systems use a broadband white light source and spectrometer

arrangement. The choice of which light source to use depends on the required application. For example, the laser provides a very narrow wavelength range, whereas the white light source provides a wide band of wavelengths. LEDs also provide a relatively small band of wavelengths (broader than laser diodes) that is governed by the semiconductor material band gap energy. The light source can also be categorised as either a directional or diffused light source. A directional light source emits the majority of the light in one direction and with a narrow angle of spread. A diffused light source emits light in a wide range of directions equally and requires optical components to efficiently couple it into waveguide. Some OFS applications may be able to utilise an unpolarised light source, others may need a polarised light source. In addition, there may be a requirement to the use a coherent rather than an incoherent light source. The most commonly used optical detectors for low-cost optical fibre sensors are the photodiode, the avalanche photodiode and the phototransistor. These optical detectors translate optical intensity into an electrical signal (a current proportional to the intensity of the light that the device is sensitive to). In addition, the light dependent resistor (LDR) can sometimes be used which converts input light intensity to generate a change in electrical resistance. However the LDRs tend to be inefficient and slow compared to the photodiode/phototransistor type detectors. A single current output is produced which corresponds to an integral result of the intensities at all the detected light wavelengths. If a system is to be able to discriminate signals at discrete spectral values, an optical detector needs to be used in conjunction with an optical grating or filter [23]. The spectral bandwidth of the detector must also be aligned with the light source spectrum and the spectral transmission of the sensor. Other parameters to consider in choice of detector include response time and the noise figure.

In considering the use of the LED and photodiode based arrangement, the digital sub-system must provide the necessary digital-analogue-digital signal interface. A typical system arrangement is shown in **Figure 4**. On the transmission side, the LED requires a drive current to output a specific light intensity. This is produced by a voltage-to-current (VI) converter that receives a voltage and outputs a current proportional to the input voltage. As the signal originates from a digital sub-system, the digital output is required to be converted to its analogue equivalent

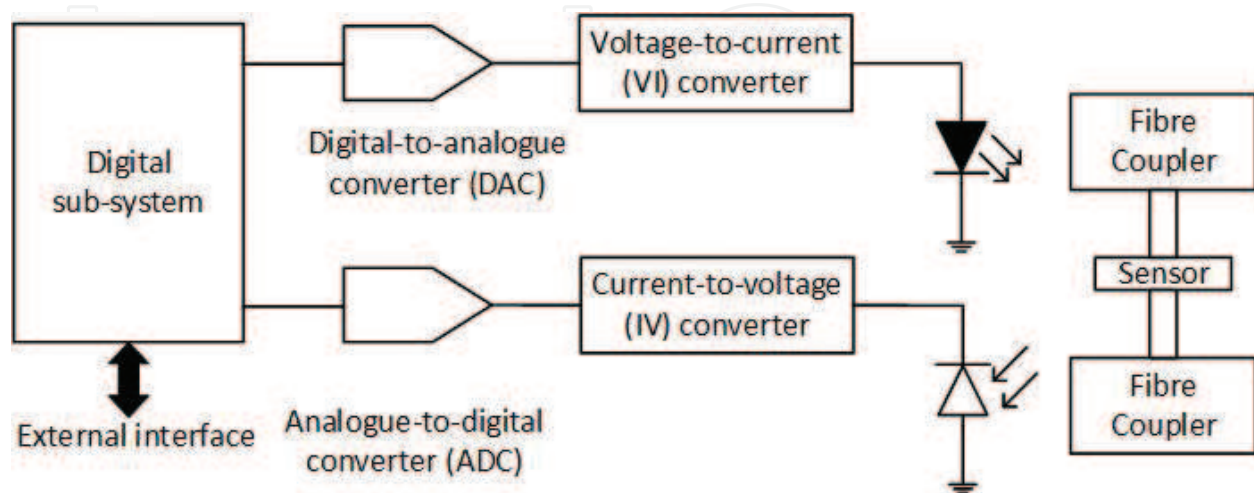


Figure 4. LED based light source current control and photodiode receiver circuit.

through a digital-to-analogue converter (DAC) with suitable speed and resolution. **Figure 4** assumes that the DAC output is a voltage rather than a current. The light is coupled to the POF and propagates to the sensor. Following transmission through and modulation by the sensor, the POF propagates the returning light signal to be received by the distal photodiode. The output of the photodiode is a current proportional to the intensity of the input light received. This is converted to a voltage through a current-to-voltage (IV) converter and applied to the input of an analogue-to-digital converter (ADC) with suitable speed and resolution. This set-up assumes that the ADC is a voltage input rather than a current input device. The digital subsystem captures and processes the digitised value. Results can then be processed and transmitted to a user or an external electronic system. The photodiode characteristics (light intensity range and range of wavelengths that can be detected) must be matched to the LED light source, otherwise the measurements do not accurately reflect the behaviour of the measured quantity.

2.4. Referencing

The accuracy of an OFS measurement depends on how reliably the value of the modulated signal reflects the behaviour of physical quantity being measured. However, other effects may cause the signal to change and therefore, their influence must ideally be isolated and removed in order to focus solely on the physical quantity being measured. In practice, this condition is not easy to achieve due to various factors. For example, the propagating light suffers from multiple attenuation factors in its propagation path which include losses from optical components and uncertainty introduced by optoelectronic component variability. To compensate for known effects that the system can be calibrated to account for, potential deviations from the ideal should be recognised and recorded. A common method is to apply an additional light signal that is used as a reference and is subjected to the same environmental influence as for measurement signal. Thus, the reference signal can be calibrated to the measurement signal. There are different techniques that can be used to introduce a reference signal into system including spatial, spectral, temporal, frequency separation or through a combination of these methods [24]. Such an approach also requires some form of signal processing, analogue or digital, and hence this must be factored into the design. Increasingly, digital signal processing (DSP) techniques are used and in the case of software based processors or hardware configured programmable logic devices (PLDs), can readily be included in order to provide for programmable and local sensor signal conditioning.

2.5. Wavelength and intensity interrogation

Some sensing elements react only to a narrow band of wavelengths. These sensor systems use a simple intensity interrogation technique where light is collected as a single value regardless of wavelength in order to provide a single light intensity reading. This technique is normally used with narrow bandwidth or monochromatic light sources. A low-cost choice for the light source in intensity interrogation based systems includes the LED and semiconductor laser diode. However, the LED is less complex to use from the viewpoint of driver circuitry and does not have the safety concerns that exist with some laser diodes. The optical receiver can be a photodiode or phototransistor. Referring to **Figure 5**, this represents the main choices to be made. The light source (**Figure 5**) is either an LED, low-cost laser diode (a) or a white light

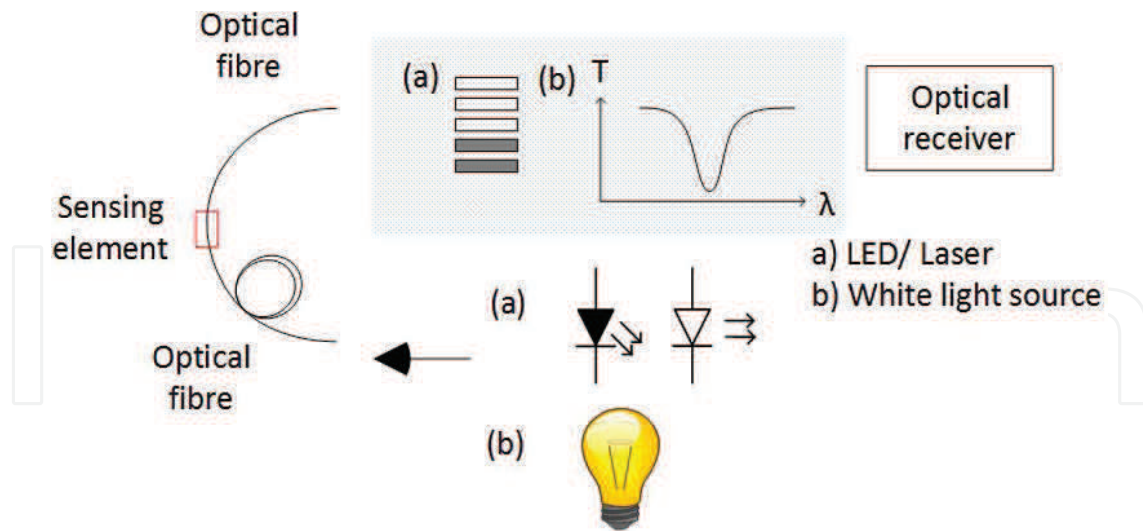


Figure 5. OFS system using a white light source and spectrometer or laser/LED and photodiode/phototransistor.

source (b). The choice of receiver is based on the light source. For the LED or laser diode, the receiver (**Figure 5**) provides only intensity interrogation (a) and for the white light source, either intensity or wavelength resolved interrogation (b).

It should also be noted and considered that some information can only be captured by observing at the signal spectrum instead of the cumulative intensity integrated across the whole spectrum. To extract such information, the signal needs to be spectrally resolved with adequate (spectral) resolution that will enable the desired measurand to be accurately determined and recorded. This technique, also known as wavelength interrogation, usually requires the use of a white light source and spectrometer as a detector.

Figure 6 shows the principle of operation of the spectrometer.

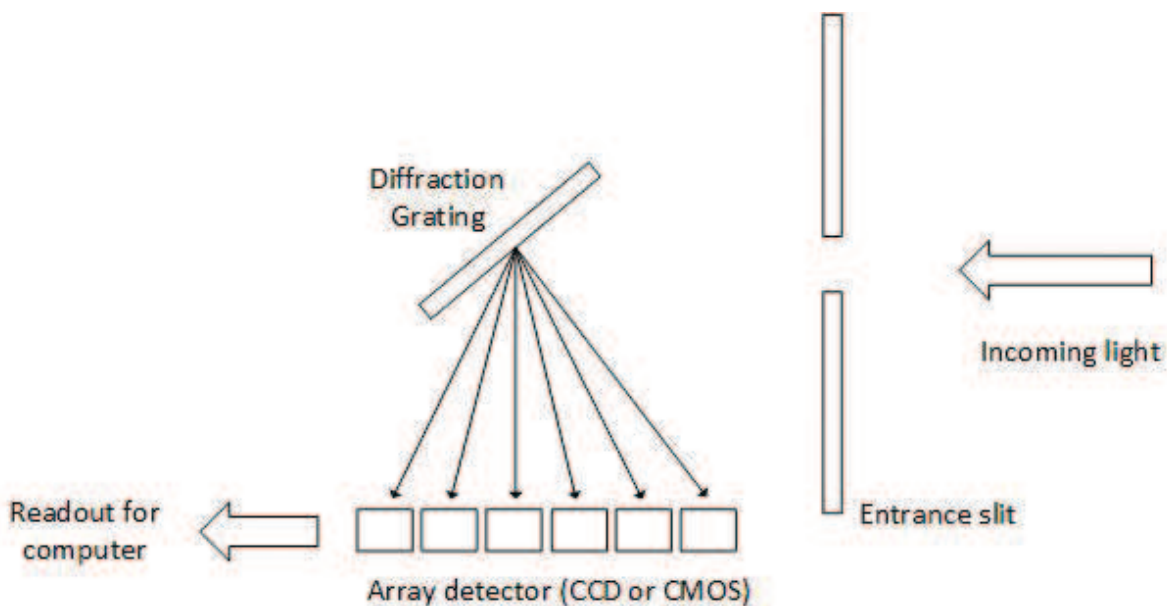


Figure 6. Principle of operation of the spectrometer.

The spectrometer is becoming increasingly widely used as an optical receiver. It receives a collimated input and disperses it into spectral components by an optical component such as a diffraction grating. The different spectral components are then registered by an array detector such as a charge-coupled-device (CCD) or complementary metal oxide semiconductor (CMOS) camera. To read out the spectral data as a digital representation of the captured optical signal, the spectrometer normally incorporates a suitable computer interface. The whole series of tasks require high precision optical elements and the spectrometer often needs to be recalibrated at regular intervals by a qualified technician. The cost of a spectrometer system is a factor that normally prohibits its use in situations with limited (financial) resources [25], although their cost and robustness is rapidly improving. Different parameters are best measured using the optimum combinations of suitable light sources and optical receivers. For example, surface plasmon resonance (SPR) sensing typically usually uses a white light source and spectrometer to measure a shift of wavelength. For purely light intensity interrogation sensing, it is possible to use a variety of light sources including the LED and laser diode, and optical receivers including the photodiode, phototransistor or the LDR. To access the information gathered by an OFS, the sensor information needs to be read out and displayed. A common acquisition module for light intensity interrogation is the DAQ module with microcontroller control. For other more complex instruments, the DAQ module is usually built into the instrument. A computer is universally used for data read-out using a common serial interface such as a wired USB or general purpose interface bus (GPIB), or a wireless interface such as Wi-Fi, Bluetooth or ZigBee. Software such as *LabVIEW*TM from National Instruments or *MATLAB*TM from The Mathworks company are commonly used to implement system control and data analysis. To identify examples of developed systems, **Table 1** provides a summary of the attributes of five reported systems. These arrangements use a variety of approaches, but are currently only suitable for use in a laboratory environment.

System configuration is generally similar for all sensor system implementations and this structure is shown in **Figure 7**. Each part can be implemented using different technologies and the choice of implementation is dependent on the requirements of the application. The required

Authors	Jiang et al. [26]	Zhao et al. [27]	Di et al. [28]	Mahanta et al. [29]	Stupar et al. [30]
Sensing mechanism	Surface plasmon resonance	Surface plasmon resonance	Intensity interrogation	Intensity interrogation	Intensity interrogation
Light source	White light source	White light source	LED	He-Ne laser source	LED
Optical receiver	Spectrometer	Spectrometer	Phototransistor	Light dependent resistor	Photo Darlington transistor
Data acquisition	Data acquisition card	Spectrometer	Data acquisition card	Data acquisition card	Microcontroller
Computer interface	USB	USB	DB37 cable	USB	ZigBee
Data readout	Computer	Computer	Computer	Computer	Computer
Data analysis	LabVIEW	–	WaveScan 2.0	LabVIEW	LabVIEW

Table 1. Examples of reported OFS system operation.

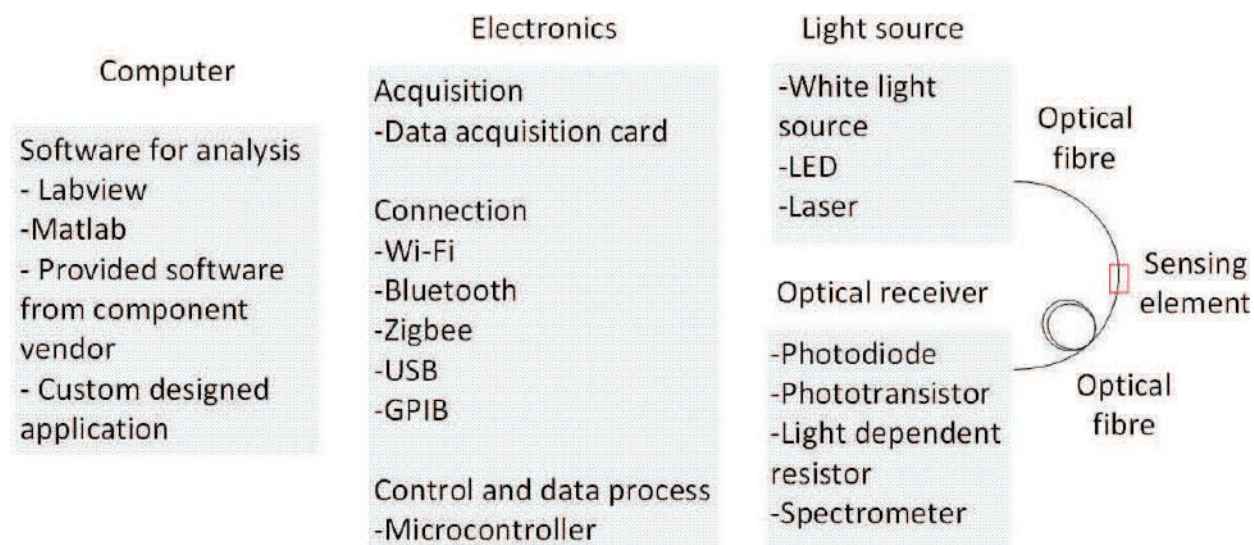


Figure 7. Typical sensor system – choice of sub-system components.

resources are identified in terms of the computing (PC), the electronics (electronic-optical-electronic signal interfacing), the light source and the optical receiver.

3. The field programmable gate array

3.1. Introduction

A programmable logic device (PLD) is a device with configurable logic and flip-flops linked together with programmable interconnect. Unlike a processor [microprocessor (μP), microcontroller (μC) or digital signal processor (DSP)] which is programmed to implement a software program, the PLD is configurable (programmable) in hardware. It is configured to implement different digital logic hardware circuits. The architecture provides flexibility in use and re-programmability to quickly re-target the same device to a different application. Early PLDs were based on the architecture of the simple PLD (SPLD) which could implement basic combinational logic and synchronous sequential logic (counter and state machine) circuits. Development of the SPLD led to the complex PLD (CPLD) which essentially is an array of SPLDs with programmable interconnect within a single device and hence, can implement more sophisticated functions. The CPLD has found uses in applications such as instrumentation and control. An alternative to the CPLD is the FPGA. This has a different architecture which allows for high-speed digital signal processing (DSP) operations which would not be possible in a CPLD. An advantage of the PLD is that it the same device can be configured and reconfigured in a short time, thus saving resources in terms of time and money to the need to develop new digital hardware. Any new update or correction can be simply done by downloading a new configuration bit stream into it.

3.2. The FPGA architecture

The FPGA is an integrated circuit (IC) that can be electrically configured to implement a digital hardware design. It consists of a matrix of configurable logic blocks (CLBs) connected via

programmable interconnects and through input/output blocks to interface with other devices. The logic blocks consist of look-up tables (LUTs) constructed using simple memories that store Boolean functions to perform logic operations. The LUT can handle any kind of logic function, but the complexity of the LUT depends on the manufacturer. In addition to the LUT, and with the growing demands to create more complex digital circuits and systems using the FPGA, special purpose blocks such as the DSP slice, embedded memory (Block RAM in FPGAs from Xilinx Inc.) and other functions have been introduced into FPGA. Today, a range of FPGAs from different vendors are available. **Table 2** provides a summary of the devices available from the key programmable logic vendors. The key differences between CPLD and the FPGA are in the device architectures and the complexity of functions that its basic unit is able to perform. The basic unit of CPLD is known as macro cell, using simple sum-of-products combinatorial logic functions and an optional flip-flop.

For a particular design, the configuration pattern is stored in memory within the device or external to the device. The configuration would initially be downloaded into the FPGA memory from an external circuit in the form of a bit stream file. Depending on the particular FPGA, the internal memory may non-volatile memory [electrically erasable programmable read only memory (EEPROM) or Flash] or volatile memory [static read only memory (SRAM)]. When using volatile memory, the configuration will need to be loaded from external memory into FPGA every time it powered on in order to set-up the FPGA. Currently, SRAM based FPGA dominate the market, however the availability of Flash memory based FPGAs is increasing and these provide lower power consumption and no boot time (i.e. the time to start operating once the device power supply is provided).

3.3. FPGA design flow

In many sensor designs, a software programmed processor, typically a μC , is programmed to provide the necessary digital sub-system operations (referring to **Figure 4**). The design flow for

Vendor	FPGA families	SPLD/CPLD	Other relevant devices	Notes
Xilinx Inc.	Virtex, Kintex, Artix and Spartan	CoolRunner-II, XA CoolRunner-II and XC9500XL	3D ICs, Zync PSoC	PSoC – Programmable system on a chip
Intel Corporation	Stratix, Arria, MAX, Cyclone and Enpirion	–	Stratix SoC FPGA	FPGAs were formerly from Altera. Altera MAX family also included CPLDs.
Atmel Corporation	AT40Kxx family FPGA	ATF15xx and ATF75xx CPLD families, ATF16xx and ATF22xx SPLD families	–	–
Lattice Semiconductor	ECP, MachX and iCE FPGA families	ispMACH CPLD family	–	–
Microsemi	PolarFire, IGLOO2 and RTG4 FPGA families	–	SmartFusion2 SoC FPGA	FPGAs were formerly from Actel

Table 2. Summary of key FPGAs and vendors (including SPLD and CPLD devices).

processor based design is well-known to many people and would be chosen based on existing knowledge and experience. However, hardware configured devices such as the FPGA can provide advantages to the system capabilities and operation if the capabilities of the FPGA were known and the ability to design with the FPGA existed. There are a number of advantages of using an FPGA within the digital sub-system and these include:

- High speed DSP operation capabilities such as digital filtering and FFT (fast Fourier transform) operations.
- Concurrent operation which means that operations in hardware can be run in parallel.
- A high number of digital input and output pins for connecting to peripheral devices.
- Programmable I/O standards such as LVTTTL, LVCMOS, HSTL and SSTL.
- In-built memories for temporary data storage.
- In-built hardware multipliers for DSP operations.
- In some FPGAs, in-built ADCs are available for analogue input sampling.
- Availability of macros such as FFT blocks for high-speed DSP operations.
- Ability to develop custom architectures suited to the particular application which does not restrict the designer to using the capabilities and limitations of existing processor architectures.

'But how is a design created using programmable logic, specifically with reference to the FPGA?' is an important question to ask. Details of the design flow would be specific to a particular device vendor and each vendor would provide an integrated development environment (IDE) for their devices. The terminology used also differs between vendors. However, **Figure 8** shows a

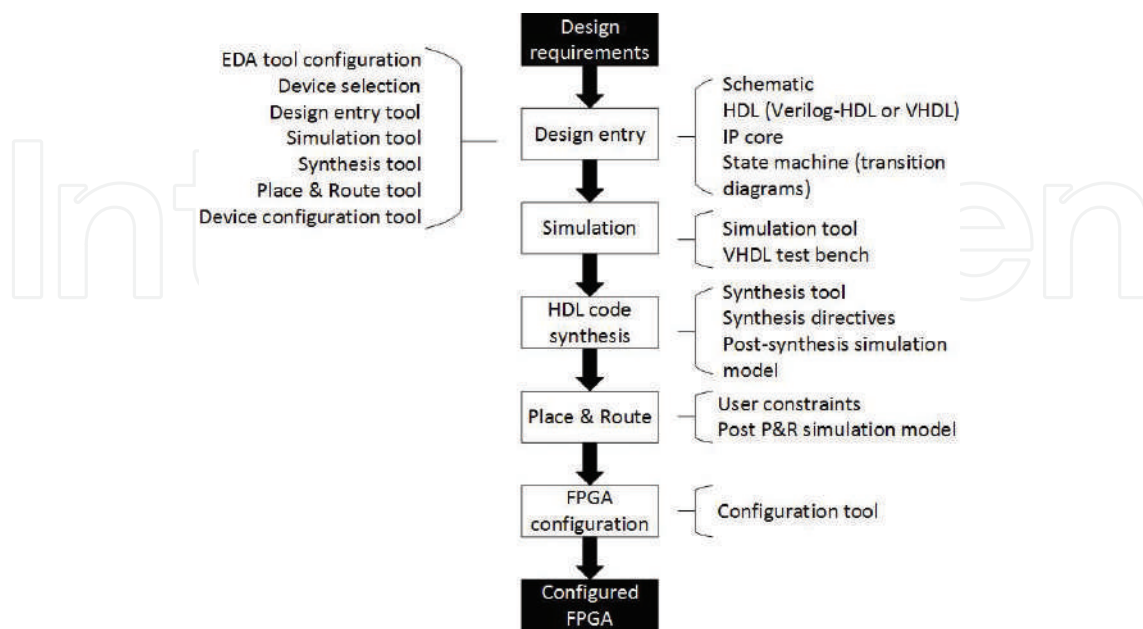


Figure 8. Simplified FPGA design flow.

simplified view of a typical FPGA design flow. Starting with the design requirements and understanding of the capabilities of the target FPGA, the FPGA design tool is used and the design description created. This can be in the form of a circuit schematic, hardware description language (HDL) description, a predesigned IP core or a FSM state transition diagram. An advantage of using an HDL is that the design description is in the form of an ASCII text file and if suitably written, is independent of any particular target device. This means that the HDL code can be synthesised to a different device and this allows for flexibility in design choice and the ability to update designs in the future if so required. The design is initially simulated using a suitably defined test bench (also referred to as a test fixture) before synthesis into logic and implementation within the FPGA (design place and route (P&R) into the FPGA hardware). After synthesis and P&R, timing details in terms of additional signal delays due to logic and interconnect propagation delays can be identified and included in the simulation studies. This is particularly important for high-speed operation as the timing of the signals propagating through the hardware need to be taken into consideration otherwise incorrect circuit operation may occur. Finally, the design can be configured into the FPGA and physical testing of the hardware can then be undertaken. At each step, depending on the simulation and test results, it may be necessary to modify aspects of the design in order to achieve correct circuit operation.

4. FPGA based OFS system

4.1. Introduction

Within an OFS system, the operation of the system in the majority of solutions is controlled by the deployment of one or more software programmed processors. There would be many reasons for adopting such an approach, particularly designer understanding and experience. Using programmable logic as an alternative requires a different design approach and a different set of designer skills. The design philosophy must be switched from *'how can I achieve the required functionality using the available sequential software functions?'* to *'how can I achieve the required functionality in concurrent hardware?'*. When considering the use of the FPGA, there must be benefits for adopting such an approach. The FPGA can:

- Provide the ability to handle real-time system operation with a high sampling rate of sensor data and other DSP operations that other, traditional microcontroller only based approaches would have problems in undertaking. For example, [31] discusses the use of the FPGA within wireless sensor networks (WSNs). In Ref. [32], a phase-sensitive optical time-domain reflectometer using the FPGA is discussed.
- Undertake high-speed DSP operations in hardware using embedded macros.
- Be readily reconfigured in the field for system upgrades.
- Allow the user to rapidly prototype the design in the same way as software programmed microcontroller while provide concurrent processing capability that overcome processor performance and precision limitations.

- Adapt its hardware configuration to a target application needs. As the FPGA does not have a fixed architecture, it is not limited to a predefined set of possible operations and this allows for a custom design which matches the operating requirements of the target application (speed, power consumption, circuit size) to be developed.

In this section, the use of the FPGA is considered as a digital core (sub-Section 4.2) to integrate functions (sub-Section 4.3) for optically based sensor systems.

4.2. The FPGA as a digital core

With reference to the digital sub-system in **Figure 4**, this can be considered in terms of the functions it needs to implement. Specifically the required functions can be considered as:

- Sensor interfacing.
- Control.
- Storage (memory).
- DSP.
- Communications to an external electronic system.
- User interfacing.

Figure 9 shows a simplified block diagram for an FPGA based design that implements the above functions. The FPGA operation control signal timing is determined by the external clock it uses (e.g. a 100 MHz clock) and control signals from external peripheral devices (e.g. an external power-on reset circuit) as well as user control which has been configured into the

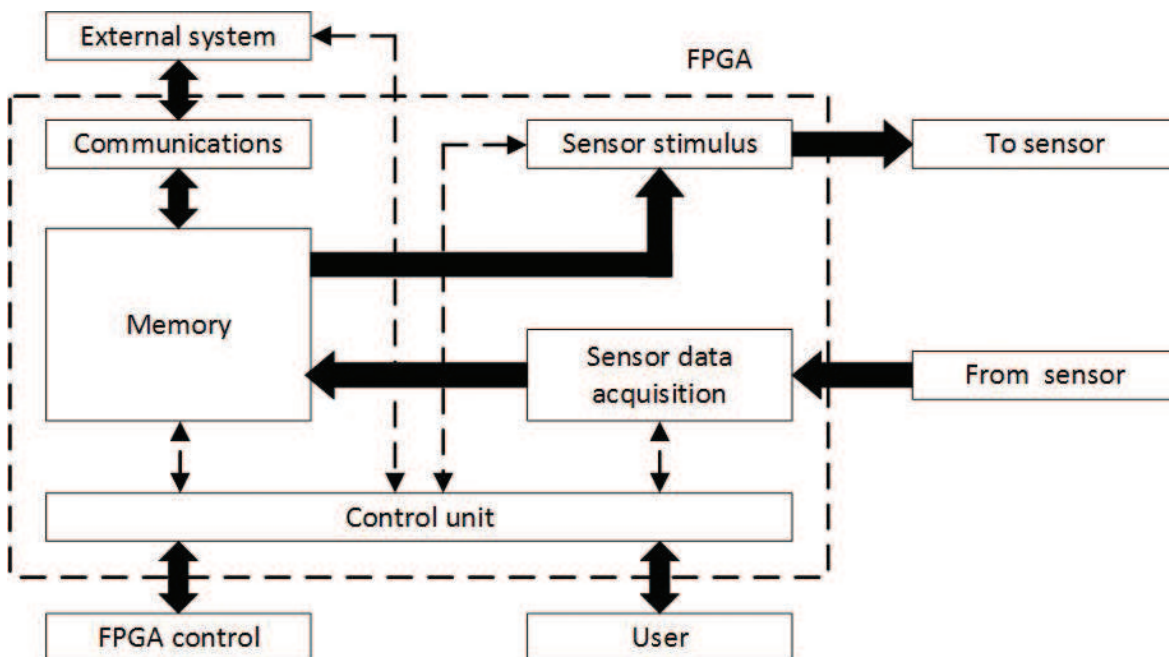


Figure 9. FPGA core functions example.

device. User control can come from an external electronic system using wired or wireless communications and from human interaction devices such as a keypad or touch-screen device. This requires a suitable *Control unit* to be designed for controlling the other circuits configured into the FPGA. Signals to/from an external system would be via a suitable *Communications* circuit that allows both control signal and data transfer. Local memory, bistables (latches and flip-flops) and SRAM are used for temporary storage. *Memory* may be internal to the FPGA only, or external. Output to the sensor in the form of *Sensor stimulus* would be in the form of a voltage that may need translating to a current. For example, an LED may be driven by a DC current level or by a modulated signal using a signal encoding scheme such as pulse-width modulation (PWM). Sensor response would be sampled using a *Sensor data acquisition* circuit. Building on this architecture, additional operations, such as DSP, can be included.

4.3. Integrating functions into the FPGA

An OFS system based on a digital core within an FPGA will need to ensure that the circuit configured into the FPGA meets the system requirements. A simple implementation would consist of a basic communications protocol, along with a basic signal generator (LED current control) and a signal capture (photodiode current sampling) along with memory for temporary storage of values (where the memory requirements are small then latches and flip-flops would be sufficient, whereas where the memory requirements are larger, static random access memory (SRAM) and Flash memory would be required). Such a basic system would not utilise many of the available hardware resources within the FPGA and in such a case, a smaller and simpler CPLD would probably be sufficient. The power of the FPGA however becomes apparent where higher operating frequencies and embedded DSP functions are introduced. For example, analogue signal measurements are influenced by external parameters such as ambient temperature and noise introduced into the signal from surrounding electronic circuitry and the ambient environment. This would be particularly noticeable where low-level signal measurements are required. To improve system performance, signal processing techniques such as oversampling, averaging and correlation can be used as well as digital filtering and the FFT. For these functions to operate in an application such as a real-time system, the calculations to be performed need to operate at high frequency and utilise high-speed memories for temporary storage. All these requirements map effectively to modern FPGAs and so can make the FPGA the natural choice for a high performance embedded sensor arrangement. With the increased interest and use of the FPGA in DSP operations, recent FPGA architectures have evolved with high-speed operation and complex DSP in mind. Generally, FPGAs today incorporate the following circuitry. With reference to the Xilinx FPGA families, these can include:

- CLB: The configurable logic block is a basic building block of the FPGA and incorporates circuitry such as the look-up table (LUT), a flip-flop and a multiplexer.
- Distributed RAM: Small RAM within the LUT.
- Slices: Slices are groups of LUTs and flip-flops.
- Block RAM (dedicated two-port memory), first-in first-out (FIFO) and error correction checking (ECC) cores.

- Singled-ended and differential input/output cells (I/O): For higher speed signals, differential signals are preferred and the programmable I/O cells can be configured for single-ended or differential signal operation and with different I/O standards.
- DSP slices: Essentially high-speed cells that can be used to create DSP operations.
- Analog(ue) mixed-signal (AMS) core: XADC, in-built ADC.
- Configuration bit stream encryption blocks incorporating methods such as AES, HMAC and DNA.

Although the discussion into the use of the FPGA has so far concentrated on the development of custom hardware designs, with hardware architectures suited to a target application needs, it is possible and in some cases preferable to utilise a software programmed processor. A processor itself is simply hardware with logic gates and memory connected in such a way to implement a processor architecture. The FPGA therefore can be used to implement a processor core and so be configured to act as a software programmed processor. Either a pre-defined processor architecture can be implemented within the FPGA as an intellectual property (IP) core with a description provided in Verilog-HDL or VHDL, or the designer can develop their own architecture processor. Therefore, the FPGA can implement a design which is based on hardware logic only, be based on a processor only or, and where the benefits of using the FPGA can be truly seen, can implement a hardware-software co-design within a single device. In addition, with the hardware resources available in many FPGAs, multiple processors can be implemented within a single FPGA and so architectures consisting of arrays of interconnected processors operating concurrently with hardware only based designs for high-speed computations can be developed.

5. Case study design

5.1. Introduction

Modern OFS systems are becoming ever more sophisticated as such systems today are targeting more complex problems than previously considered [33]. This includes the need for more sophisticated and computationally intensive data analysis methods. Today, an OFS system that uses a personal computer (PC) and software data analysis software such as *LabVIEW*[™] or *MATLAB*[™] has little difficulty to undertake such analysis tasks. However, the PC may not necessarily be an ideal data processing unit for in-field measurements or real time monitoring in remote areas due to its size and power consumption requirements. To make this system portable for personnel to carry, and for remote deployment over extended periods of time, it has to be physically small, lightweight, low-power and battery powered. The system should be as easy as possible for operator personnel to use as they should not be expected to understand the detailed electronic circuit operation or the arrangement that forms the system. It would also be better if it is capable of real-time data processing that provides timely and useful information via modern telemetry. Real-time data processing also reduces storage and transmission requirements that both consume precious resources in a portable system [34].

This section provides a case study into an OFS system using the surface plasmon resonance (SPR) principle. The objective of this case study was to demonstrate integration of the FPGA into an OFS system based on SPR. SPR is a popular sensing mechanism for biomedical optical sensors as it is sensitive to a change in the refractive index of a surrounding medium. It is a phenomenon that occurs when photon momentum is matched with plasmon momentum and thus photon energy efficiently transfers to the surface plasmon. This results in absorption of specific wavelengths of light that are then visible in the resulting light spectrum and the absorption wavelengths are then used to determine the properties of the measurand. The surface plasmon effect exists only in p-polarised (transverse magnetic) waves, so it is a requirement that a p-polarised wave is generated that oscillates in the same orientation in order to be excited. A propagating photon in vacuum or air does not have enough momentum to excite SPR [35]. The common technique to excite SPR optically is by using total internal reflection to create an evanescent wave that has a higher momentum. The matching condition depends heavily on the surrounding environment which makes it suitable for use as a sensor. **Figure 10** shows the principle of operation for the sensor used.

The electronic system design was also created to be modular in order to accommodate different sensing mechanisms. This is readily managed using POF as the interface medium since the sensor housing can be changed by simply removing and inserting the transmitting and receiving fibres. The system architecture developed is discussed and the strategy to implement refractive index measurement using a combination of the FPGA with a tri-colour (RGB: red, green, blue) LED and photodiode is proposed. The FPGA functionality is identified in a later section. System control and data acquisition with a host PC was created using the Python open

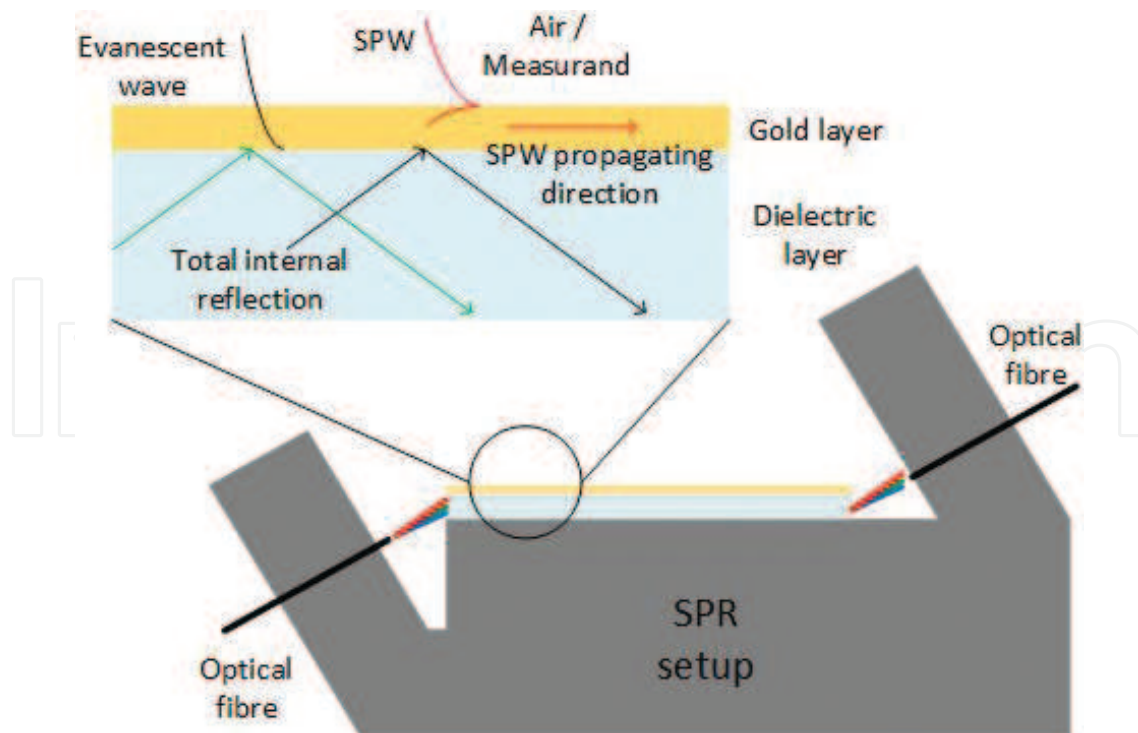


Figure 10. Surface plasmon sensor. Schematic diagram of total internal reflection and surface plasmon wave (SPW) generated during SPR.

source programming language. However, the FPGA operation does not rely on a PC connection to work. The FPGA used was the Xilinx Artix-7 [36] FPGA and this was embedded within the Arty development board from Digilent [37]. The FPGA operates on a 100 MHz clock frequency on this particular development board, so all digital signals were timed to this master clock. Connections to an external printed circuit board (PCB) with additional hardware was made using the available PCB header connections. This supports the capability to readily configure the FPGA as well as enabling the FPGA to be powered from the USB port +5 V power supply for development. In the final set-up, a battery pack provides the power supply for the FPGA. The digital logic operating within the FPGA was developed using VHDL design entry and synthesised to the Artix-7 architecture. Design entry and simulation using VHDL test benches were undertaken using the Xilinx Vivado toolset.

5.2. System architecture

The circuit hardware design, as shown in **Figure 11**, was separated into five sub-systems: OFS, power supply, digital core, light signal generation and sensing module. The power supply module comprises a low-dropout linear voltage regulator circuit for providing the necessary power supply to the light signal generation and sensing modules. A separate linear voltage regulator is used to isolate the photodiode circuit from digital noise which could be present on the power supply from the FPGA board. These regulators also provide the system flexibility to accommodate different battery voltage levels.

The light signal generation and sensing modules are additional circuits that support the optoelectronic components and their corresponding circuits. For light signal generation, a current source was designed to control the light through a digital signal (two level voltage) from the FPGA. As a tri-colour LED was used, the FPGA was required to provide a sequential series of

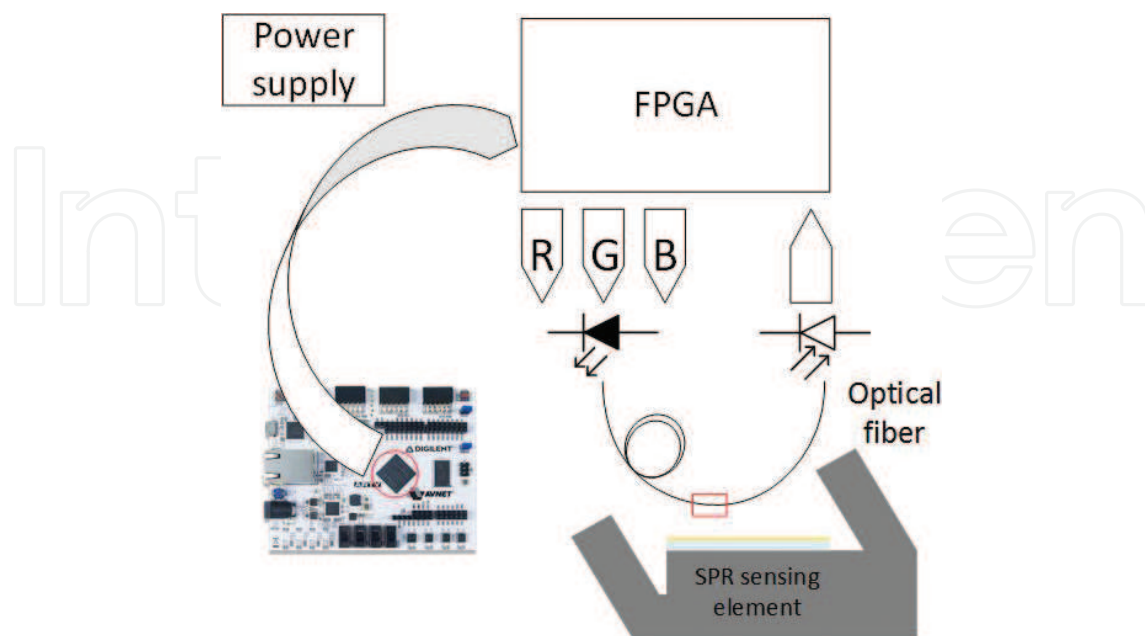


Figure 11. Case study system architecture.

red, green, and blue light pulses in a current range from 0 mA to 20 mA for each LED. With the receiver, the analogue response from photodiode circuit as a voltage was sampled using the in-built 12-bit 1 MSPS (mega sample per second) ADC (XADC) and the sampling of the responses were synchronised with the XADC conversion timing within the FPGA. Therefore, the intensity of the individual colour pulses could be recorded separately. The on-chip ADC is then used to translate the voltage reading into a 12-bit digital signal. The photodiode current is initially converted to a voltage using a high-gain transimpedance amplifier and then amplified. For a high attenuation sensing mechanism, the received light intensity is low and a high-gain transimpedance amplifier using an operational amplifier (op-amp) hence required. However, this leads to noise related issues and so the choice of a suitable op-amp along with the use of noise reduction techniques are required in the realised electronic circuit. To reduce noise in this design, PCB ground planes and an aluminium shield fixed on top of the receiver circuit was required. Although these additions reduced the resulting noise levels, additional noise reduction should also be considered. A 3D printed cap for the LED allowed a bare-end of the POF to collect light immediately from LED without any focus aid and coupled the light into the sensor housing without the need for a connector. A photodiode that requires no connector was also chosen to be the optical receiver for the modulated light. The OFS is an extrinsic sensor; gold film coating on top of a glass slide and mounted on top of a 3D printed housing to position the fibre at an angle facing the edge of the glass slide. It was designed to excite SPR for different measurands with minimum change in the blue light region.

The digital output from the FPGA is fed into an op-amp based current driver circuit. The digital logic 1 and 0 values from the FPGA are represented by two voltage levels of 3.3 V and 0 V. It is assumed in this discussion that the voltage levels produced are exactly 3.3 V and 0 V. The voltage-to-current conversion is achieved using an op-amp as a unity gain amplifier with a transistor in the feedback loop as shown in **Figure 12**. The transistor is included in this configuration as a current amplifier as it can achieve higher current output than the op-amp alone. A 20 mA current was allowed to flow when a logic 1 output is given and no current otherwise (logic 0). A current sensing resistor, R_E , is used to provide a voltage input for the op-amp. The average current then can be controlled using the pulse width modulation (PWM) control technique which is generated using a PWM generator circuit within the FPGA. The FPGA then receives an analogue output from a transimpedance circuit that translates the generated current into a voltage.

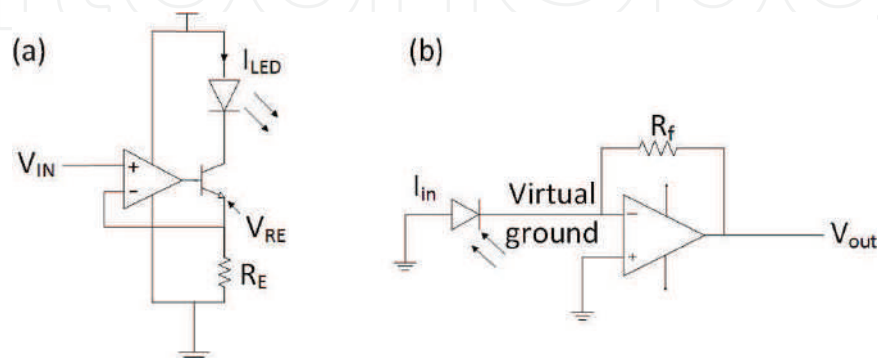


Figure 12. (a) Current source and (b) transimpedance amplifier circuit.

The Artix-7 FPGA board used also has some additional and useful features which include external SRAM, external Flash memory and the ability to be powered from the USB connector or any 7–15 V power supply voltage source. The Artix-7 FPGA operates with a core voltage of 1 V, with 3.3 V I/O and a 100 MHz master clock. The XADC has access to nine external analogue input channels and is capable of performing self-calibration in order to correct for offset and gain errors, provided that the ADC reference voltage is reliable (i.e. an accurate and stable value). On-board peripherals include a USB-UART (UART: universal asynchronous receiver transmitter) integrated circuit that allows a computer to communicate with FPGA for configuration and data transfer during normal operation. This wired communication is especially useful during development and testing. However, in the realised system and once the FPGA has been configured, a ZigBee wireless interface is used for normal data transmission and this allows the sensor hardware to be operated at a distance from the computer. This FPGA board undertakes multiple functions including system control, data processing, communication, LED control and analogue-to-digital conversion (ADC) for sensing module. Its functionality is discussed detail in the next section.

5.3. FPGA functions

To support the system operation as previously discussed, the FPGA function as a digital core (sub-system) that itself is composed of different sub-systems. The circuit configured within the FPGA is shown diagrammatically in **Figure 13**. This is a block diagram representation of the VHDL code. These sub-systems include data acquisition, control system, communication, LED pulse generation. All these sub-systems were initially described in VHDL and operate concurrently. The control system includes an XADC acquisition control unit that keeps the timing of the XADC and LED pulse generation units in synchronisation. It allows the user to set the

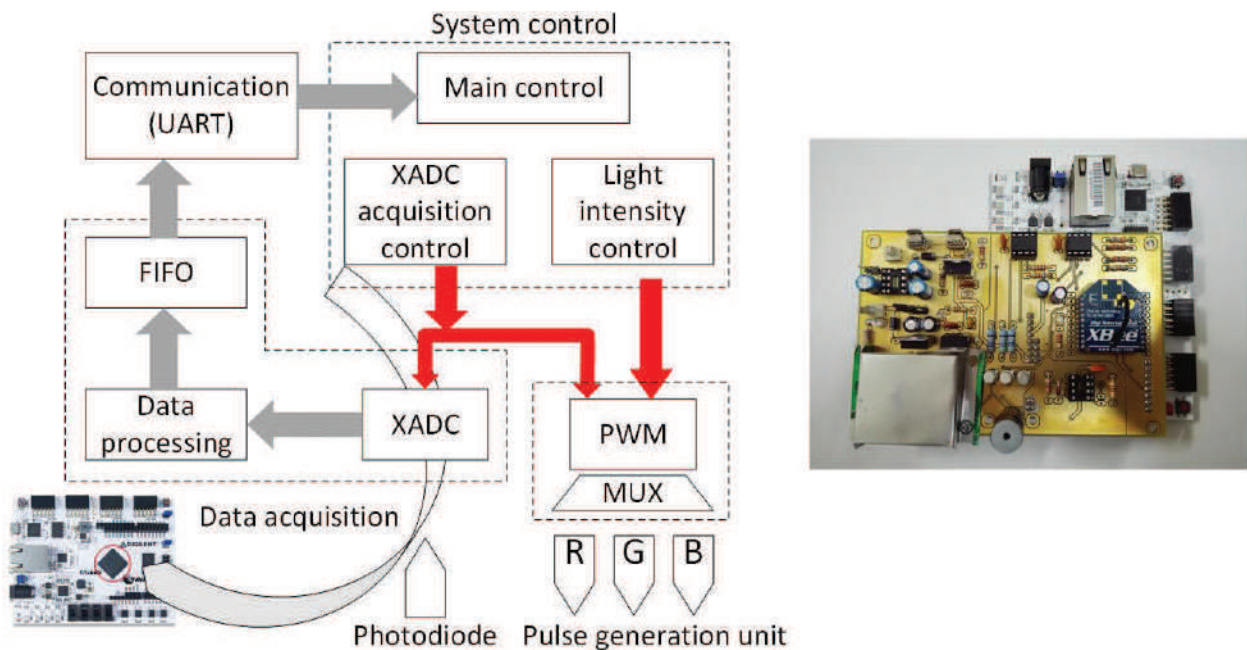


Figure 13. Schematic of the digital design implemented within the FPGA.

number of measurement to be taken. The light intensity control unit is tasked to regulate the duty cycle of the PWM output for each LED. The generated signal is then passed to the digital pin output set by multiplexer. The data acquisition system involves the use of the XADC that is capable to sample voltage reading from 0 to 3.3 V into 12-bit digital signal and can be controlled in order to accommodate different settling times for the signal conditioning circuit or different sampling rates. The acquired data bit size is bigger than the UART protocol (with eight bit data, one start bit and one stop bit), and so is required to be separated into two parts. A protocol was developed for data transmission which included a header to indicate each different light colour. Within the FPGA, sampled data is processed and the processed data stored in memory storage before transmitted to PC when requested to do so. Serial communication is implemented using UART protocol with a Baud rate of 115,200 baud. At this stage, the data is then processed with computer.

5.4. Control and data acquisition using Python

In order to interface the PC to the FPGA and then to the user, a USB or ZigBee serial interface is used. The FPGA and the computer then communicate using UART protocol so that the computer can send commands to the FPGA and the FPGA can respond with sensor data results. Therefore, a suitable programming language was required to achieve the computer-to-FPGA and computer-to-user communications. In this work, the Python open source language is used to implement system control, data acquisition and data presentation. A graphical user interface (GUI) was built using *Tkinter* and *Matplotlib* modules for Python which enabled live data presentation. The GUI is shown in **Figure 14** with left graph showing all red, green, and blue intensities plotted together and three smaller graph at the right side shown three

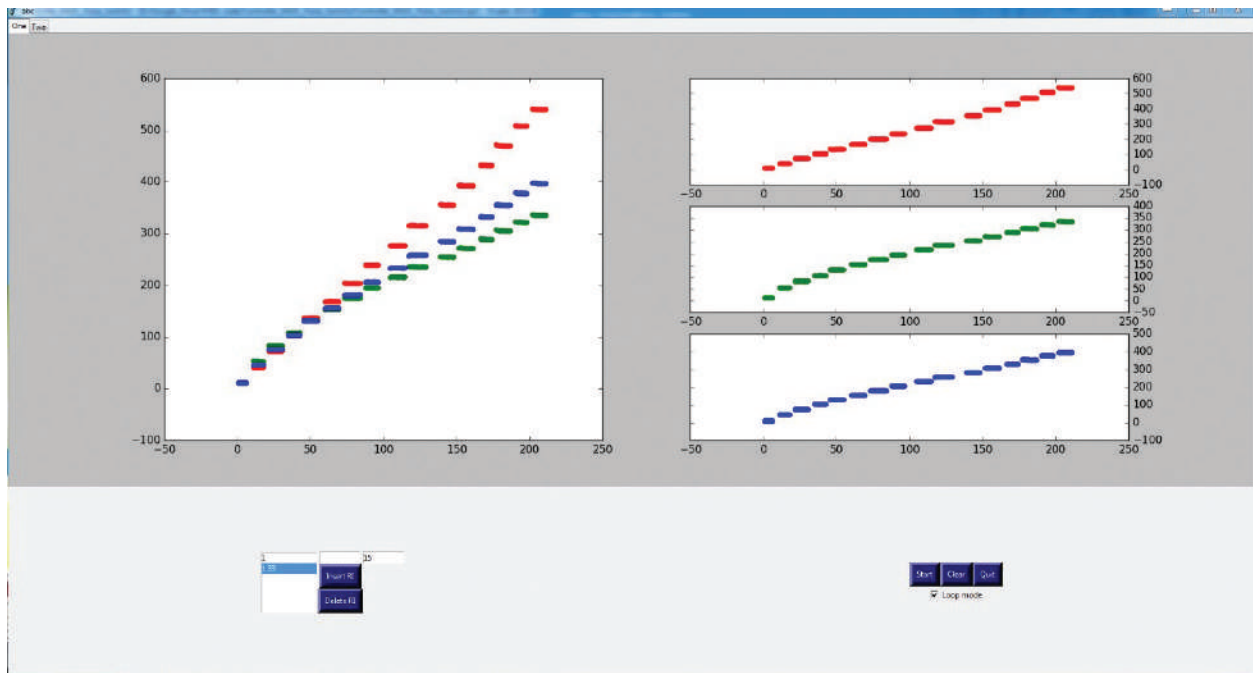


Figure 14. GUI created from Python.

individual colour intensity plots. Data labels for data frame are selected at lower left region of GUI. The lower right region are for system control: measurement initiation and process termination. The *Pyserial* module was used for communication with the FPGA by using the computer COM port in order to carry out FPGA control and sensor data acquisition. The acquired data stream is then formatted using the *NumPy* and *Pandas* modules. The data structure used was a data frame using the *Pandas* module. This data frame was considered as it allowed the sensor data to be serialised into a minimal and useful *JSON* format that could then be stored in a database or readily transferred elsewhere. In addition, a *MySQL* database was set up for data storage and management.

Test results are shown in **Figure 15**. The top plot shows the sensor results with air as the measurand and the bottom plot with water. A comparison is made between the spectrometer measurement using an Ocean Optic QE65000 and the Industrial Fiberoptics IF-D91 photodiode output. The spectrometer integration time was set to 500 ms. The line plot showing the spectrometer reading is shown on the left y-axis and the overlap bar plot showing the photodiode measurement for intensity reading is shown on the right y-axis. The wavelength x-values are only for the spectrometer reading while the photodiode just overlap with it for comparison. In this view, both the spectrometer and photodiode's y-values are represented in plot using arbitrary units. The photodiode measurement and spectrometer readings for different measurands has shown good agreement in terms of the trend of the signal during the measurand change. However, the magnitude of the changes are not exactly the same for the spectrometer and photodiode and this can be attributed to different spectral responsivity. The plot shows that the blue colour measurement is relatively stable for both the photodiode and spectrometer. The blue colour measurement shows a weak response to both measurands and it is therefore suitable for use as the reference signal. It provides the system with a self-calibration capability which can be built in hardware within the FPGA.

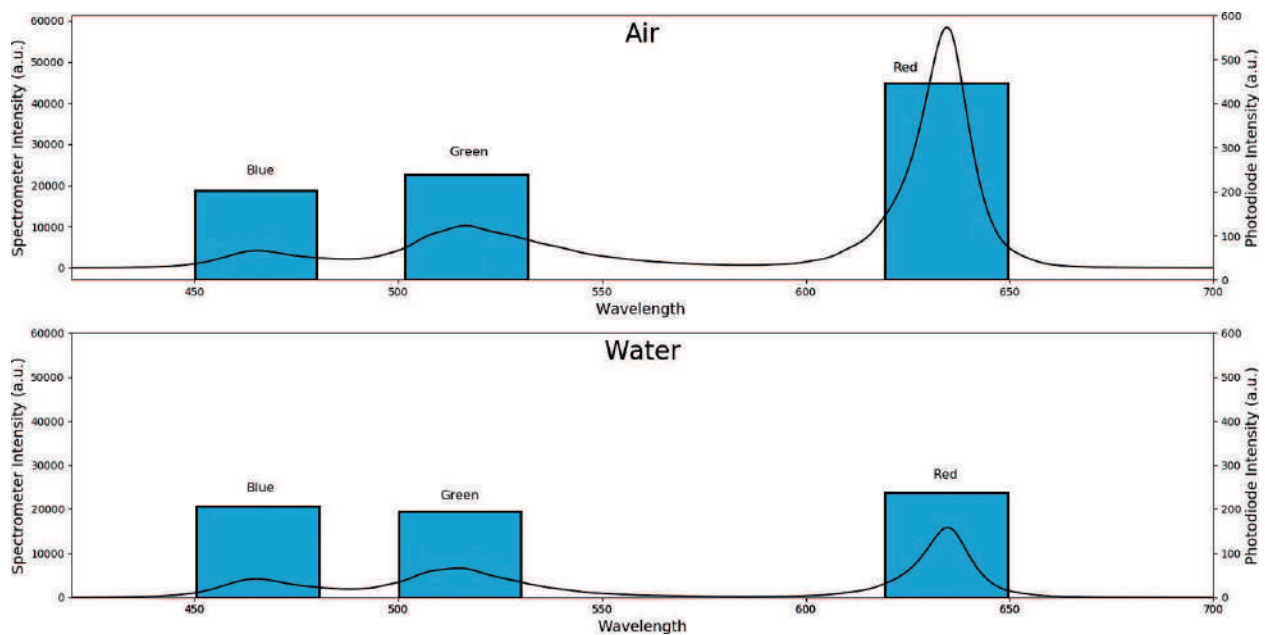


Figure 15. OFS test results visualisation.

6. Conclusions

In this chapter, the use of programmable logic has been discussed in relation to the design and implementation of OFS systems using POF technology. Specifically, the focus of the discussion was based on the use of the FPGA to provide hardware functionality as a complement to a software based processor approach. In this case, the necessary digital operations were performed in hardware using a synthesised VHDL description of the digital logic functions. The FPGA provided the necessary signals to control the output light intensity of a LED source using current control. An RGB LED was used, and hence three wavelengths of light could be created and combined. The light was propagated to a SPR sensor using standard 1 mm diameter POF and was received by a photodiode detector, also using POF. The chapter has included a case study of a SPR sensor based on POF, and the system has been designed, built and characterised when tested in air and submersed in water. With the functions created in this particular application, the building blocks of the FPGA based sensor systems capable of measurement of a wide range of parameters could be developed. FPGA control, data capture and visualisation was achieved on PC using the Python open source language.

Acknowledgements

The authors would like to thank the European Union Erasmus Mundus LEADERS (Leading mobility between Europe and Asia in Developing Engineering Education and Research) scholarship programme in its support of this work.

Author details

Yong Sheng Ong¹, Ian Grout^{1*}, Elfed Lewis¹ and Waleed Mohammed²

*Address all correspondence to: ian.grout@ul.ie

1 Department of Electronic and Computer Engineering, University of Limerick, Limerick, Ireland

2 BU-CROCCS, School of Engineering, Bangkok University – Rangsit Campus, Bangkok, Thailand

References

- [1] Grattan L, Meggitt B, editors. Optical Fiber Sensor Technology: Advanced Applications- Bragg Gratings and Distributed Sensors. New York, USA: Springer US; 2000. Vol. X. p. 385. DOI: 10.1007/978-1-4757-6079-8

- [2] Alwis L, Sun T, Grattan KTV. Optical fibre-based sensor technology for humidity and moisture measurement: Review of recent progress. *Measurement*. 2013;**46**:4052-4074. DOI: 10.1016/j.measurement.2013.07.030
- [3] O'Keefe S, McCarthy D, Woulfe P, Grattan MW, Hounsell AR, Sporea D, Mihai L, Vata I, Leen G, Lewis E. A review of recent advances in optical fibre sensors for in vivo dosimetry during radiotherapy. *The British Journal of Radiology*. 2015;**88**. DOI: 10.1259/bjr.20140702
- [4] Ashley J, Welch, Martin JC van Gemert, editors. *Optical-Thermal Response of Laser-Irradiated Tissue*. 2nd ed. The Netherlands: Springer Netherlands; 2011. XIV, 958 p. DOI: 10.1007/978-90-481-8831-4
- [5] Yang M, Li S, Jiang D. Review on optical fiber sensing technologies for industrial applications at the NEL-FOST. In: EWSHM – 7th European Workshop on Structural Health Monitoring; July; Nantes, France. 2014
- [6] Lecler S, Meyrueis P. Intrinsic optical fiber sensor. In: YasinM, Harun SW, Arof H, editors. *Fiber Optic Sensors*. InTech; 2012. DOI: 10.5772/27079. <https://www.intechopen.com/books/fiber-optic-sensors/intrinsic-optical-fibersensor>
- [7] Grattan KTV, Sun T. Fiber optic sensor technology: An overview. *Sensors and Actuators A: Physical*. 2000;**82**(1–3):40-61. DOI: 10.1016/S0924-4247(99)00368-4
- [8] Alwis LSM, Bustamante H, Roth B, Bremer K, Sun T, Grattan KTV. Evaluation of the durability and performance of FBG-based sensors for monitoring moisture in an aggressive gaseous waste sewer environment. *Journal of Lightwave Technology*. 2016;**35**(16): 3380-3386. DOI: 10.1109/JLT.2016.2593260
- [9] Mescia L, Prudenzano F. Advances on optical Fiber sensors. *Fibers*. 2014;**2**:1-23. DOI: 10.3390/fib2010001
- [10] Laskar S, Bordoloi S. Microcontroller-based instrumentation system for measurement of refractive index of liquid using bare, tapered and bent fibre as sensor. *IET Optoelectronics*. 2013;**7**(6):117-124. DOI: 10.1049/iet-opt.2013.0052
- [11] Bram Van Hoe, Graham Lee, Erwin Bosman, Jeroen Missinne, Sandeep Kalathimekkad, Oliver Maskery, David J. Webb, Kate Sugden, Peter Van Daele, Geert Van Steenberge. Ultra small integrated optical Fiber sensing system. *Sensors*. 2012;**12**(9):12052-12069. DOI: 10.3390/s120912052
- [12] Suryadi, Puranto P, Adinanta H, Waluyo TB, Priambodo PS. Development of microcontroller-based acquisition and processing unit for fiber optic vibration sensor. *Journal of Physics: Conference Series*. 2016;**817**(012042):1-6. DOI: 10.1088/1742-6596/817/1/012042
- [13] Ibrahim SK, Farnan M, Karabacak DM, Singer JM. Enabling technologies for fiber optic sensing. In: *Optical Sensing and Detection IV*; April 29. Brussels, Belgium: SPIE; 2016. DOI: 10.1117/12.2234975

- [14] Safia AA, Al Aghbari Z, Kamel I. Phenomena detection in mobile wireless sensor networks. *Journal of Network and Systems Management*. 2016;**24**(1):92-115. DOI: 10.1007/s10922-015-9342-z
- [15] Guemes A, Fernandez-Lopez A, Soller B. Optical fiber distributed sensing – Physical principles and applications. *Structural Health Monitoring*. 2010;**9**(3):233-213. DOI: 10.1177/1475921710365263
- [16] Pfrimer FWD, Koyama M, Dante A, Ferreira EC, Antonio Siqueira Dias J. A closed-loop interrogation technique for multi-point temperature measurement using fiber Bragg gratings. *Journal of Lightwave Technology*. 2014;**32**(5):971-977. DOI: 10.1109/JLT.2013.2295536
- [17] Werneck MM, Allil RCSB. Optical fiber sensors. In: Krejcar O, editor. *Modern Telemetry*. 2011. DOI: 10.5772/25006. <https://www.intechopen.com/books/modern-telemetry/optical-fiber-sensors>
- [18] Sun S-S, Dalton LR, editors. *Introduction to Organic Electronic and Optoelectronic Materials and Devices*. Boca Raton, Florida, USA: CRC Press; 2008. 936 p
- [19] Lee GCB, Van Hoe B, Yan Z, Maskery O, Sugden K, Webb D, Van Steenberge G. A compact, portable and low cost generic interrogation strain sensor system using an embedded VCSEL, detector and fibre Bragg grating. In: *SPIE 8276, Vertical-Cavity Surface-Emitting Lasers XVI, 82760E*; January 21; San Francisco, California, USA. 2012. DOI: 10.1117/12.907810
- [20] Fidanboyulu K, Efendioglu HS. Fiber optic sensors and their applications. In: *5th International Advanced Technologies Symposium (IATS'09)*; May 13–15; Karabuk, Turkey. 2009. p. 1-6
- [21] Woyessa G, Pedersen JKM, Fasano A, Nielsen K, Markos C, Rasmussen HK, Bang O. Simultaneous measurement of temperature and humidity with microstructured polymer optical fiber Bragg gratings. In: *25th Optical Fiber Sensors Conference (OFS)*; 24–28 April; Jeju, South Korea. 2017. DOI: 10.1117/12.2265884
- [22] Muda R, Clifford J, Chambers P, Mulrooney J, Merlone-Borla E, Gili F, Dooly G, Fitzpatrick C, Lewis E. Simulation and measurement of carbon dioxide exhaust emissions using an optical fibre based mid infrared point sensor. *Journal of Optics A: Pure and Applied Optics*. 2009;**11**:1-7. DOI: 10.1088/1464-4258/11/5/054013
- [23] Lee B. Review of the present status of optical fiber sensors. *Optical Fiber Technology*. 2002;**9**:57-79. DOI: 10.1016/S1068-5200(02)00527-8
- [24] Udd E, Spillman WB Jr, editors. *Fiber Optic Sensors: An Introduction for Engineers and Scientists*. 2nd ed. John Wiley & Sons, Inc.; 2011. 512 p. DOI: 10.1002/9781118014103
- [25] Santos JL, Farahi F, editors. *Handbook of Optical Sensors*. Boca Raton, Florida, USA: CRC Press; 2017. 718 p
- [26] Jiang X, Meng Q. Design of optical fiber SPR sensing system for water quality monitoring. In: *International Conference on Computational Science and Engineering (ICCSE 2015)*; July 20–21; Qingdao, Shandong, China. 2015. pp. 123-127

- [27] Zhao Y, Deng Z-Q, Hu H-F. Fiber-optic SPR sensor for temperature measurement. *IEEE Transactions on Instrumentation and Measurement*. 2015;**64**(11):3099-3104. DOI: 10.1109/TIM.2015.2434094
- [28] Di H, Xin Y, Sun S. Electric current measurement using fiber-optic curvature sensor. *Optics and Lasers in Engineering*. 2016;**77**:26-30. DOI: 10.1016/j.optlaseng.2015.07.009
- [29] Mahanta DK, Laskar S. Power transformer oil-level measurement using multiple fiber optic sensors. In: 2015 International Conference on Smart Sensors and Application (ICSSA); IEEE; 2015. p. 102-105. DOI: 10.1109/ICSSA.2015.7322519
- [30] Stupar DZ, Bajic JS, Manojlovic LM, Slankamenac MP, Joza AV, Zivanov MB. Wearable low-cost system for human joint movements monitoring based on Fiber-optic curvature sensor. *IEEE Sensors Journal*. 2012;**12**(12):3424-3431. DOI: 10.1109/JSEN.2012.2212883
- [31] Antonio de la Piedra, An Braeken and Abdellah Touhafi. Sensor systems based on FPGAs and their applications: A survey. *Sensors* 2012;**12**(9):12235-12264. DOI: 10.3390/s120912235
- [32] CK Madsen, T Snider, R Atkins, J Simcik. Real-time processing of a phase-sensitive distributed fiber optic perimeter sensor. In: SPIE Proceedings Vol. 6943: Sensors, and Command, Control, Communications, and Intelligence (C3I) Technologies for Homeland Security and Homeland Defense VII, 694310; April 16; SPIE; 2008. DOI: 10.1117/12.777987
- [33] Wang Y, Negri LH, Kalinowski HJ, Mattos DS, Negri GH, Paterno AS. Hardware embedded fiber sensor interrogation system using intensive digital signal processing. *Journal of Microwaves, Optoelectronics and Electromagnetic Applications*. 2014;**13**(2). DOI: 10.1590/S2179-10742014000200003
- [34] Plaza AJ, Chang C-I, editors. *High Performance Computing in Remote Sensing*. Boca Raton, Florida, USA: CRC Press; 2007. 496 p
- [35] Pitarke JM, Silkin VM, Chulkov EV, Echenique PM. Theory of surface plasmons and surface-plasmon polaritons. *Reports on Progress in Physics*. 2007;**70**(1):1-87. DOI: 10.1088/0034-4885/70/1/R01
- [36] Xilinx Inc. Artix-7 FPGA, 7 Series FPGAs Data Sheet: Overview, DS180 (v2.4) [Internet]. March 28, 2017. Available from: https://www.xilinx.com/support/documentation/data_sheets/ds180_7Series_Overview.pdf [Accessed: July 7, 2017]
- [37] Xilinx Inc. Artix-7 35T Arty FPGA Evaluation Kit [Internet]. 2017. Available from: <https://www.xilinx.com/products/boards-and-kits/art7.html> [Accessed: July 7, 2017]